

# Semi-contained Interactions of Atmospheric Neutrinos in the MACRO Detector

Thesis by  
Robert G. Nolty

In Partial Fulfillment of the Requirements  
for the Degree of  
Doctor of Philosophy

California Institute of Technology  
Pasadena, California

2002  
(Defended 18 October 2001)

©2002

Robert G. Nilty

All rights reserved

## Acknowledgments

Personally, I would like to thank my family and my spiritual communities, especially Urban Village, for tremendous support through some very lean times.

Professionally, I extend thanks first of all to my advisor, Barry Barish, for his incredible patience and generosity when the road did not seem to be going anywhere. I am grateful to Caltech, the U.S. Department of Energy and the Italian Istituto Nazionale di Fisica Nucleare for financial support. I thank my collaborators for making MACRO what it was, with special affection for the Italians who showed me hospitality and for the Americans (and Greeks!) with whom I shared a cross-cultural experience.

During my mid-grad-school crisis in 1992, when I was looking for an opportunity to convert to experimental physics, I chose to join MACRO largely because of the nature of the weekly meeting of the Caltech MACRO group. It was lively, intense, sometimes loud, usually filled with laughter. Ideas were proposed, shot down, and rebuilt. It was there that I learned to be a scientist, and it is to this group that this thesis is dedicated:

Barry Barish	Charlie Peck
Gary Liu	Doug Michael
John Hong	Stephane Coutu
Erotokritos Katsavounidis	Sophia Kyriazopoulou
Chris Walter	Kate Scholberg
Rongzhi Liu	Neal Pignatano

## Abstract

Atmospheric neutrinos arise from the decay of particles (primarily pions, muons and kaons) produced in the collision of high energy cosmic ray particles with the atmosphere. The great distances traveled by atmospheric neutrinos between their production and detection make them useful for studying neutrino oscillations, the predicted phenomenon of massive neutrinos changing flavor in flight. This thesis reports a study of atmospheric neutrinos interacting in the MACRO detector. The results, though somewhat clouded by large theoretical uncertainties, clearly rule out the no-oscillations hypothesis, and are consistent with oscillations with the parameters preferred by other MACRO neutrino analyses, as well as those of other experiments (most notably Super-Kamiokande). Combining this analysis with another MACRO neutrino analysis, some of the theoretical errors cancel, further constraining the region of allowed oscillation parameters.

# Contents

<b>1</b>	<b>Introduction</b>	<b>1</b>
1.1	The Wily Neutrino . . . . .	1
1.2	Massive Neutrinos . . . . .	2
1.2.1	Physics Beyond the Standard Model . . . . .	2
1.2.2	Direct Searches . . . . .	3
1.2.3	Neutrino Oscillations . . . . .	4
1.2.4	Current Oscillation Experiments and Limits . . . . .	8
1.3	MACRO as a Detector of Atmospheric Neutrinos . . . . .	12
<b>2</b>	<b>The MACRO Detector</b>	<b>14</b>
2.1	The Scintillator System . . . . .	17
2.1.1	Scintillation Counters . . . . .	17
2.1.2	Scintillator Electronics . . . . .	19
2.2	Streamer Tubes . . . . .	21
2.3	Calibrations . . . . .	22
2.3.1	Timing Reconstructions . . . . .	22
2.3.2	Calibration Procedure . . . . .	26
<b>3</b>	<b>Monitoring and Modeling the Detector</b>	<b>33</b>
3.1	Muon Analysis . . . . .	33
3.2	Microcuts: Eliminating Bad Channels from the Analysis . . . . .	35
3.3	Detecting Dead and Inefficient Channels . . . . .	39
3.4	Detector Simulation . . . . .	43
3.4.1	Why the Detector Must Be Simulated . . . . .	43
3.4.2	Geant and GMACRO . . . . .	44
3.4.3	Tuning the Monte Carlo . . . . .	49

3.4.4	Simulating Problems with the Real Hardware . . . . .	61
<b>4</b>	<b>Predicting the Atmospheric Neutrino Interaction Rate</b>	<b>70</b>
4.1	Atmospheric Neutrino Flux . . . . .	70
4.1.1	Transport Equations . . . . .	71
4.1.2	More Precise Calculations . . . . .	76
4.1.3	The Bartol Flux . . . . .	83
4.2	Neutrino Cross Section . . . . .	83
4.2.1	The Lipari Cross Section Model . . . . .	88
4.2.2	The NEUGEN Cross Section Model . . . . .	90
<b>5</b>	<b>Measurement of Neutrino Interactions in the Detector</b>	<b>92</b>
5.1	Topologies of Neutrino-Induced Muons in MACRO . . . . .	92
5.1.1	Topology Criteria for This Analysis . . . . .	94
5.2	The Dataset . . . . .	95
5.2.1	Data Flow and Analysis Software . . . . .	95
5.2.2	Real Data . . . . .	98
5.2.3	Simulated Data . . . . .	99
5.3	Analysis Chain . . . . .	105
5.3.1	Preparing the Data for Analysis . . . . .	105
5.3.2	Identifying the Best Candidate Track . . . . .	106
5.3.3	Containment . . . . .	109
5.3.4	First Background-Reducing Cuts . . . . .	112
5.3.5	Further Background Suppression Methods . . . . .	113
5.4	Results . . . . .	119
5.4.1	The Selected Events . . . . .	119
5.4.2	The Monte Carlo Prediction . . . . .	121
5.4.3	Comparison of the Measurement and the Prediction . . . . .	123
<b>6</b>	<b>Interpretation</b>	<b>127</b>
6.1	Corrections and Estimates of Uncertainty in the Measurement . . . . .	127

6.1.1	Externally-produced Neutrino-induced Muon Background . . .	127
6.1.2	Mistimed Background . . . . .	127
6.1.3	Remaining $\beta = -1$ Background . . . . .	128
6.1.4	The Nominal Detector Simulation . . . . .	129
6.1.5	The Simulation of Non-ideal Detector Performance . . . . .	132
6.2	Estimates of Uncertainty in the Theoretical Prediction . . . . .	133
6.2.1	Neutrino Flux . . . . .	133
6.2.2	Neutrino Cross Section . . . . .	133
6.2.3	The Solar Cycle . . . . .	134
6.2.4	Summary . . . . .	134
6.3	Oscillation Analysis . . . . .	135
6.3.1	The Number of Events . . . . .	135
6.3.2	The Angular Distribution . . . . .	137
6.4	This Analysis in the Context of Other MACRO Analyses . . . . .	143
<b>7</b>	<b>Conclusion</b>	<b>148</b>
	<b>Bibliography</b>	<b>149</b>

# Chapter 1 Introduction

## 1.1 The Wily Neutrino

Although much of what we know about the neutrino is based on experimental evidence, it may still be considered the theorists' particle; indeed, we could say the neutrino was not so much discovered as invented. The neutrino is so elusive that there have been no serendipitous experimental discoveries. It is only with extensive guidance from theory that the experimentalists have been able to build apparatus to catch traces of the wily neutrino, and even then it has been hard going.

The idea that was to evolve into the neutrino was first postulated in 1930 in Pauli's famous "Dear Radioactive Ladies and Gentlemen" letter [1]. The purely theoretical motivation was to reconcile the spin and statistics of nuclear beta decay and to explain the continuous electron spectrum. Within a few years the neutrino was on solid theoretical ground as an essential component of Fermi's quantitative theory of beta decay [2]. However, more than two decades were to pass before the neutrino was directly observed.

By 1953 nuclear theory including neutrinos had matured despite the non-observation of neutrinos; indeed it was only the theoretical understanding of neutrinos that allowed Reines and Cowan to devise their delayed coincidence experiments to make the first experimental detection of neutrinos when they observed inverse beta decay induced by reactor-produced electron neutrinos [3].

Soon after the first experimental observation of neutrinos, experimentalists were in a position to answer some theoretical questions about neutrinos. The V-A Lorentz structure of the neutrino vertex was quickly deduced by a large number of experiments within two years of the 1956 suggestion of parity violation by Lee and Yang [4].

Another question awaiting an experimental answer concerned the existence of two types of neutrinos. Some neutrinos arose during the production of electrons and

some during the production or decay of muons, but it was not known if these two types of neutrinos were identical. Schwarz, Lederman and Steinberger invented the neutrino beam at Brookhaven and their results showed that neutrinos associated with muons behaved differently than those associated with electrons [5]. The existence of multiple types of neutrinos became a central assumption of the electroweak theories of the 1960s.

Soon the theorists were again out in front with the prediction of neutral currents. A number of experiments in the early-1970s confirmed the existence of neutral currents [6, 7, 8] and bolstered confidence in the emerging theories.

By this time neutrinos were understood well enough that they could be used as an experimental tool to study other physics. In particular, deep inelastic scattering of neutrinos off nucleons confirmed the picture of nucleons consisting of fractionally-charged partons which had been emerging from electron scattering experiments [9, 10]. Also in the 1960s Ray Davis began his chlorine experiment [11] which attempted to study the solar interior by observing the rate of solar neutrino interactions on earth. In 1987, observations of neutrinos from Supernova 1987A [12, 13, 14] were analyzed in attempts to understand the interior of a collapsing star.

Extensive high energy neutrino scattering experiments throughout the 1970s and 1980s confirmed that neutrinos behave very much as predicted by the Standard Model they helped to create. However, by the end of the 1980s intriguing hints were emerging that neutrinos that travel large distances may depart from the behavior predicted by the Standard Model. Many interpreted these hints as evidence that the neutrinos are not massless as the Standard Model assumes.

## 1.2 Massive Neutrinos

### 1.2.1 Physics Beyond the Standard Model

The Standard Model of particle physics has been very successful in quantitative calculations of particle phenomenology but is rather unsatisfying as a fundamental theory.

It is widely believed that the Standard Model is a low-energy effective theory deriving from a more elegant high-energy theory. In the 1990s, after the spectacular validation of the Standard Model in precision measurements at LEP, attention of both theorists and experimentalists turned to phenomena beyond the Standard Model in the hopes of constraining explorations of fundamental theories. Many sectors of particle physics may give a glimpse beyond the Standard Model, but three in particular have received attention as the possible next step in experimental particle physics: studying the origin of mass by direct observation of the Higgs particle (awaiting completion of the LHC experiment at CERN); studying the origin of CP violation by precision measurements of quark mixing (currently underway at SLAC and KEK); and finally, mixing and mass in the neutrino sector. Of these three, neutrino experiments have been the first to yield exciting results pointing beyond the Standard Model.

In the Standard Model, neutrinos are assumed to be massless. However, *a priori* there is no compelling theoretical reason to expect neutrinos to be massless, and the Standard Model may be easily extended to include small neutrino masses without contradicting any known observations. In fact, if one assumes the Standard Model is a low-energy effective theory of a non-renormalizable quantum gravity field theory, neutrino masses arise generically [15]. However, simple extensions to the Standard Model are only satisfying if they explain why the neutrino masses are so small (compared to the typical mass scales in the theories).

### 1.2.2 Direct Searches

Upper limits on neutrino mass come from observations that rely directly on the mass properties of neutrinos. In the next section, the more subtle effect of neutrino oscillations will be considered.

The most straightforward experiments attempt to detect neutrino mass by examining the energy spectrum of observable particles in decays involving neutrinos; if neutrinos have mass the maximum possible invariant mass for the sum of other particles is reduced. Such examinations have yielded no evidence for neutrino masses,

and have set the upper limits shown in Table 1.1.

$m_{\nu_e}$	$< 3 \text{ eV}$
$m_{\nu_\mu}$	$< 0.19 \text{ MeV}$
$m_{\nu_\tau}$	$< 18.2 \text{ MeV}$

Table 1.1: Direct limits on neutrino masses from PDG [16].

Analyses of neutrino mass from the arrival time of SN1987A neutrinos [12, 13, 14] are somewhat difficult to interpret, and under the skeptical judgment of the Particle Data Group [16], they do not improve the limits shown above.

If we adopt standard Big Bang Cosmology, in the current universe there is a high density of relic neutrinos created during the radiation-dominated epoch. From the current observation that the density of the universe is not far from the critical density, we may rule out neutrino masses greater than a few tens of MeV [17].

### 1.2.3 Neutrino Oscillations

If neutrinos have mass, there may be no reason to expect the mass eigenstates to be the same as the weak force eigenstates. Thus, the particles created and destroyed in weak interactions (the electron neutrino, muon neutrino and tau neutrino) may be superpositions of mass eigenstates; conversely the mass eigenstates would be superpositions of the flavor eigenstates. As a particle propagates according to the mass eigenstates, its flavor content could evolve, a process known as neutrino oscillation. We can gain insight into this process by considering a two-neutrino model, with flavor eigenstates  $|\nu_a\rangle$  and  $|\nu_b\rangle$ , and mass eigenstates  $|\nu_1\rangle$  and  $|\nu_2\rangle$ .

In general,

$$|\nu_a\rangle = |\nu_1\rangle \cos \theta + |\nu_2\rangle \sin \theta$$

$$|\nu_b\rangle = -|\nu_1\rangle \sin \theta + |\nu_2\rangle \cos \theta$$

where  $\theta$  is called the mixing angle.

## Vacuum Oscillations

If a flavor eigenstate  $|\nu_a\rangle$  is created at  $x = 0$  with momentum  $p$ , the two mass components of the particle will have slightly different velocities, and the flavor content of the propagating particle will vary in time. Invoking the quantum mechanical equivalence of energy to frequency, the state at time  $t$  of a particle that is pure  $|\nu_a\rangle$  at  $t = 0$  is

$$|\nu_a\rangle_t = \exp(-iE_1 t)|\nu_1\rangle \cos\theta + \exp(-iE_2 t)|\nu_2\rangle \sin\theta$$

Invoking the orthogonality of the mass eigenstates ( $\langle\nu_1|\nu_2\rangle = 0$ ), we find the probability the particle will be observed as  $|\nu_b\rangle$  at time  $t$  is<sup>1</sup>

$$|\langle\nu_b|\nu_a\rangle_t|^2 = \sin^2 2\theta \sin^2\left(\frac{1}{2}(E_2 - E_1)t\right)$$

For ultrarelativistic neutrinos of given momentum,

$$\begin{aligned} E_2 - E_1 &= \sqrt{p^2 + m_2^2} - \sqrt{p^2 + m_1^2} \\ &\approx \frac{m_2^2 - m_1^2}{2p} \end{aligned}$$

so that (equating  $p$  with  $E$  and  $t$  with  $x$  for ultrarelativistic neutrinos)

$$|\langle\nu_b|\nu_a\rangle_t|^2 = \sin^2 2\theta \sin^2\left(\frac{\Delta m^2 x}{4E}\right)$$

This is the fundamental equation of neutrino oscillations. (This simple treatment sweeps a lot of details under the rug, but more rigorous treatments involving wave packets do not change the basic phenomenology of oscillations [18].) The unknown parameters of the theory are the mixing angle  $\theta$  and the mass difference  $\Delta m^2$ . If we restore the factors of  $c$  and  $\hbar$  that have been suppressed, we find the half-wavelength

---

<sup>1</sup>NOTE: No cats were harmed in the collapse of this wavefunction.

for oscillation is

$$L_{vac} = \frac{4\pi E\hbar}{\Delta m^2 c^3} = 2.48 \left( \frac{E}{\text{GeV}} \right) \left( \frac{\text{eV}^2}{\Delta m^2} \right) \text{ km} \quad (1.1)$$

We have little theoretical guidance for the expected value of the parameters  $\theta$  or  $\Delta m^2$ . We do know that the analogous mixing angles in the quark sector are relatively small (for example, for the Cabbibo Angle  $\theta_c$ ,  $\sin^2 \theta_c \approx 0.05$ ). Without unexpected fine tuning, the mass difference is expected to be on the order of the neutrino masses.

Atmospheric neutrinos (described below), with typical energies of a few GeV and with typical path lengths of thousands of kilometers, are in principle sensitive to mass differences less than 0.1 eV.

### Oscillations in Matter

The above arguments apply for neutrinos propagating in vacuum. However, when neutrinos propagate through matter, their evolution is altered by weak interactions with the medium, which may be considered a perturbation to the mass hamiltonian. All three known types of neutrinos (electron, muon and tau neutrinos) will feel the effects of the neutral current weak force, typified by the Feynman diagram in Figure 1.1a. If these are the only types of neutrinos that participate in mixing, this force will shift the phase of all components of a mass eigenstate equally, so the nature of oscillations is unchanged by it. However, only the electron weak eigenstate participates in the charged current weak force shown in Figure 1.1b. This changes the phase evolution of the electron component of a mass eigenstate and alters the oscillation behavior. It has also been postulated that a sterile neutrino exists and mixes with the known neutrino flavors, but does not participate in neutral current or charged current weak interactions. If so, the absence of reaction (a) will cause its phase to shift relative to the other types of neutrinos.

Wolfenstein [19] was the first to make quantitative calculations of matter effects, in 1978<sup>2</sup>. The energy perturbation is  $\langle \nu_e | H_{eff} | \nu_e \rangle$  where  $H_{eff}$  arises from the  $W$ -

---

<sup>2</sup>There were errors in Wolfenstein's original formula, but they were corrected in the subsequent literature and here.

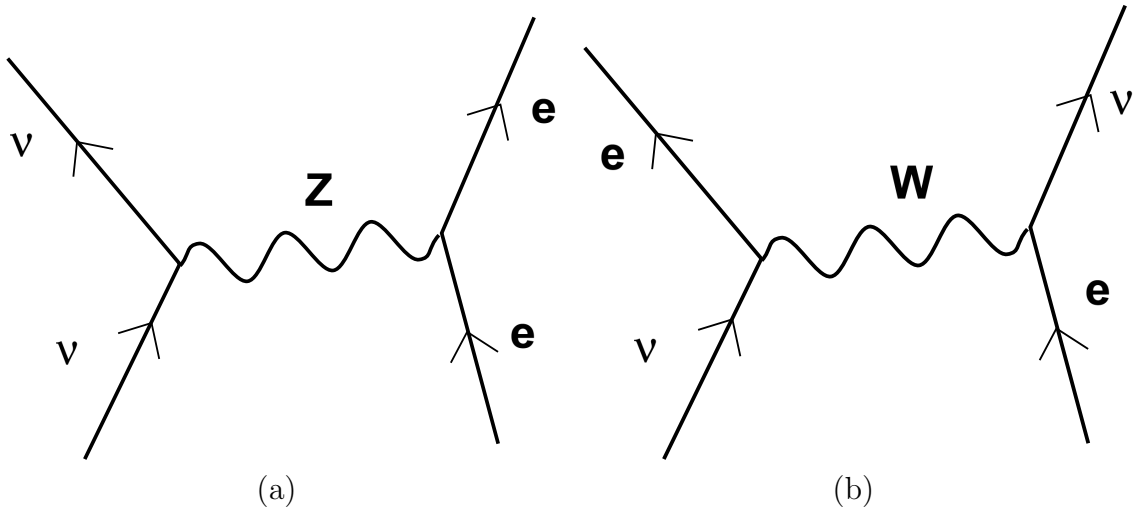


Figure 1.1: Feynman diagrams for weak interactions in matter. (a) Neutral current interactions, affecting all known neutrino flavors. (b) Charged current, affecting only electron neutrinos.

exchange of Figure 1.1b. For low energy neutrinos we may use the old Fermi theory for the diagram; thus the magnitude of the effect will be proportional to the Fermi constant  $G_F$ . The effect will also be proportional to the number of electrons with which the neutrino can interact. The result of Wolfenstein's exact calculation is

$$\Delta E = \sqrt{2}G_F N_e$$

where  $N_e$  is the density of electrons. Thus, electron neutrinos acquire an additional phase  $e^{-i\Delta E t}$  relative to the muon and tau components of a mass eigenstate, and the phase depends on the density of electrons but is independent of neutrino energy (at least in the range where the Fermi approximation is valid). For ultrarelativistic neutrinos one may obtain the “matter oscillation length”  $L_m$ , which is the length over which the phase of the electron neutrinos changes by  $2\pi$  relative to the vacuum oscillation formula. For propagation through the earth, with

$$N_e \approx 3 \frac{\text{g}}{\text{cm}^3} * N_A \frac{\text{nucleon}}{\text{g}} * \frac{1 \text{ electron}}{2 \text{ nucleon}} = 9.9 \times 10^{23} \frac{\text{electron}}{\text{cm}^3}$$

we find  $L_m \approx 10^4$  km, so matter effects are an important correction to vacuum oscillation calculations. (For solar neutrinos, in the center of the sun,  $L_m \approx 200$  km, and matter effects lead to some surprising phenomenology.)

### 1.2.4 Current Oscillation Experiments and Limits

Regions of parameter space excluded or preferred by various experiments to be discussed below are shown in Figure 1.2.

#### Accelerator Neutrinos

An accelerator neutrino beam consists almost entirely of  $\nu_\mu$  or almost entirely of  $\bar{\nu}_\mu$ . Some detectors that are not efficient to detect  $\nu_e$  or  $\nu_\tau$  measure only  $\nu_\mu$  disappearance. Others, also sensitive to  $\nu_e$  or  $\nu_\tau$  appearance, are able to probe much smaller mixing angles. Accelerator experiments from the 1970s through the end of the century did not see evidence of muon neutrino disappearance. Given the energies (typically tens to hundreds of GeV) and baselines from neutrino creation to detection (hundreds of meters), typical experiments could only see oscillations if  $\Delta m^2$  were a few  $\text{eV}^2$  or greater.

An innovation on the traditional beam experiments is K2K, an ongoing experiment with a baseline from accelerator to detector of 250 km, and a detector very sensitive to both  $\nu_\mu$  and  $\nu_e$  interactions. With low statistics (44 interactions in the detector in two years, with 64 expected in the absence of oscillations) they see evidence for  $\nu_\mu$  disappearance and no evidence for  $\nu_e$  appearance [20].

A completely different type of accelerator-based experiment brings accelerator-created pions to rest in a dense medium where they decay. (Some pions that decay in flight also contribute to the experiment.) Detailed reconstructions of neutrino interactions in a target a few tens of meters away can show evidence of  $\bar{\nu}_\mu \rightarrow \bar{\nu}_e$  or  $\nu_\mu \rightarrow \nu_e$ . Two experiments of this type have been performed. LSND [21] sees evidence of electron neutrino appearance while Karmen [22] does not. Because of differences in geometry, much of the LSND-preferred region is not excluded by Karmen,

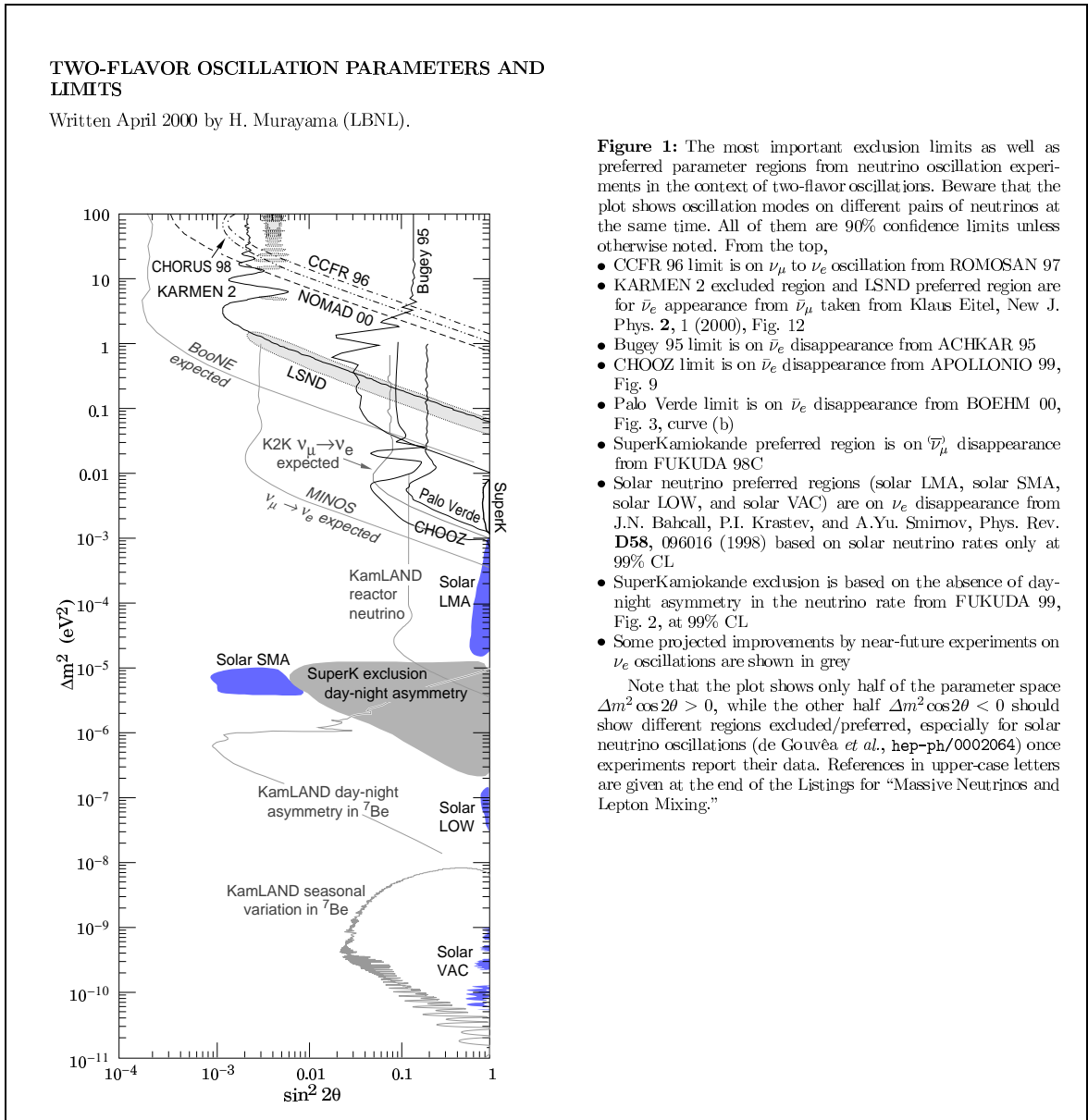


Figure 1.2: Figure and caption on neutrino oscillation limits from the latest Review of Particle Physics [16].

at least at the 90% confidence level. The parameter space preferred by LSND (and not ruled out by beam experiments) is  $0.04 \text{ eV}^2 < \Delta m^2 < 2 \text{ eV}^2$  with  $\sin^2 2\theta > 0.002$ . (See Figure 1.2.)

### **Reactor Neutrino Experiments**

Nuclear reactors produce copious numbers of electron antineutrinos with energies of a few MeV. Because the neutrino flux can be calculated precisely when the power level is known, detectors tens to hundreds of meters from a reactor can serve as electron antineutrino disappearance experiments. None has seen any evidence for oscillations.

### **Solar Neutrino Experiments**

One solar neutrino detector, the chlorine detector at Homestake, has been running almost continuously since 1967, and has consistently seen a flux of electron neutrinos around one-third that predicted by the Standard Solar Model. However, due to large theoretical uncertainties and some experimental questions, the result did not garner much attention at first. By the 1990s the errors were under control and then a series of new experiments confirmed the deficit in additional energy ranges. Today, there is no doubt that electron neutrinos are disappearing due to unknown neutrino physics, but it is difficult to prove the deficit is due to oscillations.<sup>3</sup> Assuming the deficit is due to oscillations, four disjoint regions of parameter space are allowed, all with  $\Delta m^2 < 0.001 \text{ eV}^2$ . (See Figure 1.2.)

### **Atmospheric Neutrinos**

When high energy cosmic ray particles (protons or heavier nuclei with typical energies in the GeV - TeV range) collide with the atmosphere, a hadronic shower develops. Charged pions and kaons in the shower can decay in flight yielding high energy muons and muon neutrinos. If the muon also decays in flight, it can yield another muon neutrino and an electron neutrino. Flux of these so-called atmospheric neutrinos is

---

<sup>3</sup>During the preparation of this thesis, the SNO collaboration [23] reported evidence that the missing electron neutrinos are present at earth in other, non-sterile flavors (presumably  $\nu_\mu$  or  $\nu_\tau$ ).

on the order of several hundred per square centimeter per second. (Flux models will be discussed in detail in Chapter 4.) The energy and flight pathlength of these neutrinos are not as well-determined as accelerator neutrinos. However, the detected neutrinos come from a large variety of energies and pathlengths so one can potentially explore more oscillation parameter space with atmospheric neutrinos than with accelerator neutrinos.

Prior to 1996, a number of experiments built primarily for other purposes (including MACRO) were able to make measurements of atmospheric neutrino fluxes. The early results were confusing, with some measurements favoring, some disfavoring, oscillations. Even the positive experiments did not have enough precision to show that the deviations were best explained by oscillations. In 1996 the first experiment built primarily to study oscillations in atmospheric neutrinos, Super-Kamiokande (Super-K), turned on and quickly amassed the dominant data set in the field. By 1998, Super-K was able to claim the discovery of neutrino oscillations [24]. The result is convincing because Super-K derives oscillation parameters from many different analyses involving different event sets with different energy ranges, some utilizing ratios in which much of the systematic uncertainty cancels, and all the analyses give results consistent with a single oscillation hypothesis.

Super-K results [25] indicate muon neutrino disappearance, without a corresponding appearance of electron neutrinos, with large mixing angle ( $\sin^2 2\theta > 0.88$ ) and  $0.0015 \text{ eV}^2 < \Delta m^2 < 0.005 \text{ eV}^2$ . Other recent experiments with positive results (MACRO [26] and Soudan [27]) have results consistent with Super-K but with a less-precise preferred region in parameter space.

This thesis presents an analysis of atmospheric neutrinos interacting inside the MACRO detector.

## Future Experiments

Energized by the discovery that neutrinos are oscillating at least in the atmospheric neutrino sector, a number of new experiments are in the works to resolve the outstanding qualitative questions (How many types of neutrinos participate in oscillations?

Which neutrinos mix with which? Is the solar neutrino problem due to oscillations?) and to make more precise measurements of the oscillation behavior.

One cannot simultaneously accommodate the LSND, atmospheric and solar results with only the three known types of neutrinos. Perhaps there is a “sterile neutrino” – a fourth type of light neutrino that does not participate in weak interactions but does mix with the well-known neutrinos through oscillations. Or, perhaps the LSND result is wrong, or either the LSND or solar neutrino problems are not due to oscillations.

Also, the results so far presented have been within the framework of 2-flavor oscillations. However, the reality probably involves a  $3 \times 3$  or  $4 \times 4$  matrix of mixing parameters. Perhaps, for example, muon neutrinos mix primarily with tau neutrinos but have a small mixing angle with electron neutrinos.

A few of the most significant planned experiments include:

- Sudbury Neutrino Observatory - sensitive to neutral current interactions of solar neutrinos, SNO should be able to determine if the disappearing electron neutrinos are turning into active or sterile neutrinos.
- NuMI and CNGS - long baseline (730 km) experiments in the U.S. and Europe respectively which are designed to explore the parameter space around the atmospheric neutrino preferred parameters.
- Boone - a short baseline accelerator experiment that should definitively confirm or refute the LSND result.
- Kamland - the first long baseline reactor neutrino experiment which will extend down to mass differences relevant to the solar neutrino problem.

### 1.3 MACRO as a Detector of Atmospheric Neutrinos

In the years leading up to such next-generation experiments, we may use existing detectors (most built for other purposes) to further elicit the nature of the flux dis-

crepancies and guide the developers of the new experiments. The use of the MACRO detector in atmospheric neutrino physics is an example of such a fortuitous and timely analysis.

Located deep underground at the Italian Gran Sasso National Lab (LNGS), the Monopole, Astrophysics and Cosmic Ray Observatory (MACRO) was a large area detector of ionizing particles. In the neutrino realm, it was most efficient for detecting muons from the charged current interaction of muon neutrinos and antineutrinos. The experimental technique is to look for upward-going muons, thus eliminating the large background due to downgoing primary muons produced by cosmic rays in the atmosphere above MACRO. MACRO could detect upgoing muons that were produced within its volume or those that were produced in the rock below. MACRO also had some sensitivity to electrons from charged current interactions of electron neutrinos within the detector, or neutral current interactions of any flavor neutrino within the detector. However, MACRO was not optimized for these experimental signatures.

This thesis reports a study of the interactions within the MACRO detector of upgoing atmospheric neutrinos.

## Chapter 2 The MACRO Detector

The MACRO experiment is a collaboration of about 100 physicists from Italian and U.S. institutions. Originally conceived to detect slow-moving supermassive particles in the cosmic radiation (e.g., GUT monopoles) [28, 29, 30, 31, 32], MACRO has also produced results in the study of penetrating muons from high energy cosmic rays [33, 34, 35, 36, 37, 38, 39, 40, 41, 42] (sometimes in coincidence with a surface detector [43, 44, 45]), searches for astronomical point sources of penetrating muons [46], searches for low-energy neutrino bursts from collapsing stars [47, 48], a search for fractionally-charged particles [49], as well as neutrino physics [50, 26, 51, 52, 53, 54]<sup>1</sup>. MACRO began taking data in 1989 while it was still under construction. The detector was completed in 1994, and stable running lasted until the detector was retired in December, 2000.

MACRO was located in Hall B of the Italian Gran Sasso National Laboratory (LNGS) in the Apennine mountain range east of Rome (see Figure 2.1). Located in the middle of a mountain, Hall B is covered by at least 3150 m.w.e. of rock. (1 meter of water equivalent (m.w.e.) = 100 g/cm<sup>2</sup>.) At this depth, electrons and hadrons from cosmic ray showers cannot penetrate and the muon flux from cosmic rays is about 10<sup>-6</sup> of the flux at the surface.

MACRO (Figure 2.2) was a very large detector (approximately 72 m × 12 m × 10 m). The long axis consisted of six identical *supermodules*, often abbreviated “SM.” The walls and central layer of the detector were instrumented with planes of streamer tubes (ST) and boxes of liquid scintillator (SC). The upper half of MACRO (the *attico*) was hollow while the lower half consisted of layers of uninstrumented rock absorber and additional streamer tube planes. Also in the lower half was one plane of passive plastic track etch detector in which exotic particles were expected to leave

---

<sup>1</sup>An up-to-date list of MACRO publications may be found at <http://www.df.unibo.it/macro/pub1.htm>.

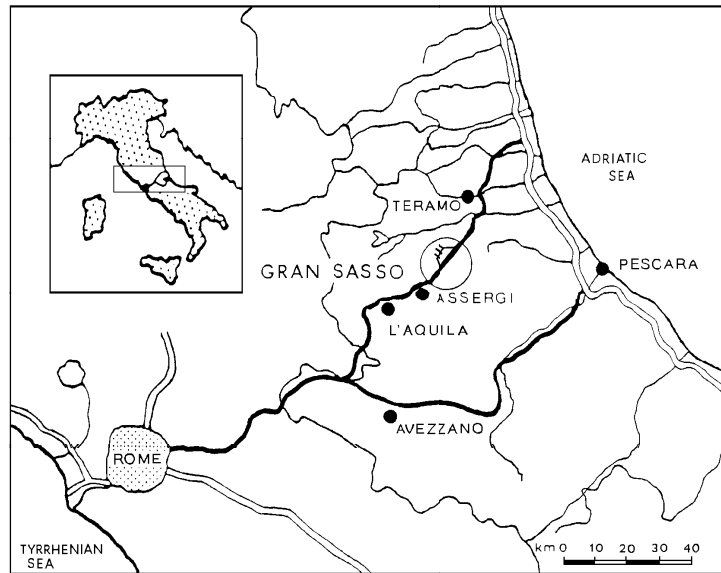


Figure 2.1: Location of Gran Sasso.

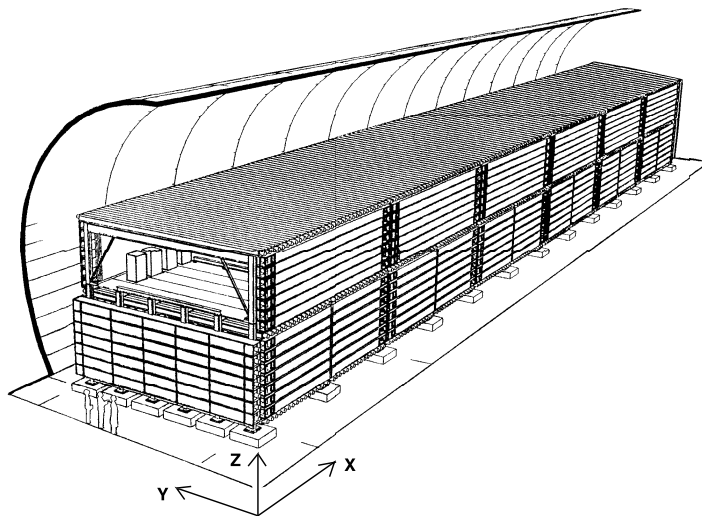


Figure 2.2: The MACRO detector.

distinctive tracks that could be analyzed months later. (See Figure 2.3.)

We define the Z-axis to be vertical upward, the X-axis along the long dimension of MACRO (north to south), and the Y-axis along the horizontal short dimension (west

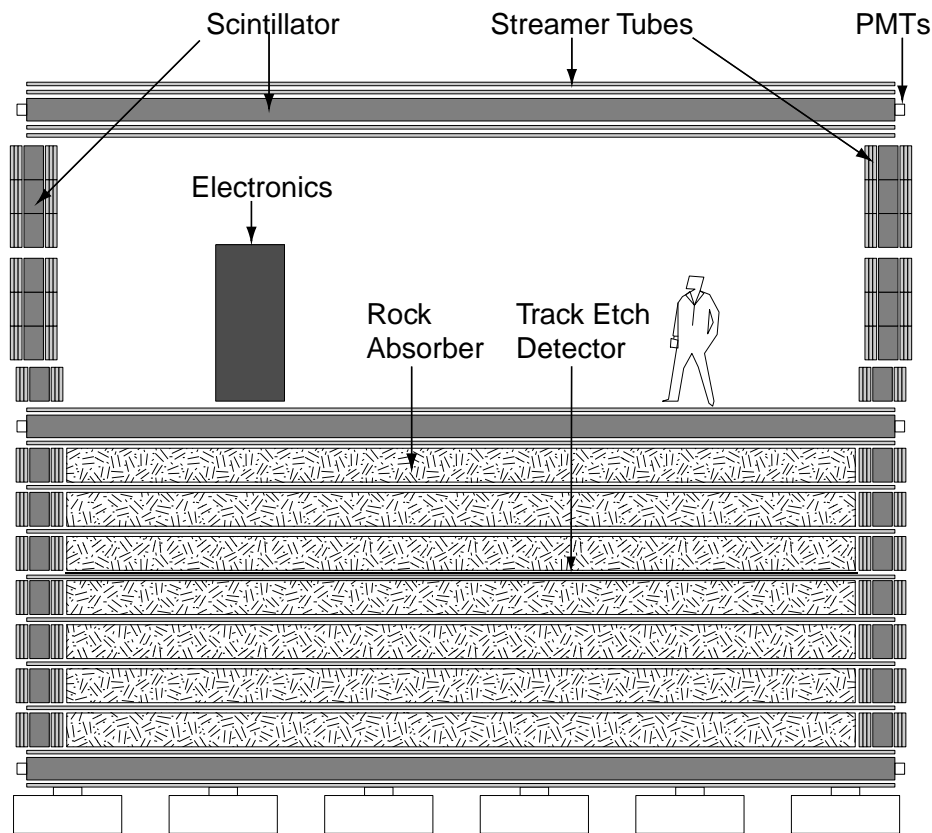


Figure 2.3: Cross section of MACRO.

to east). An additional coordinate in the X-Y plane is defined; D is the coordinate perpendicular to the streamer tube pickup strips (described below).

The two main electronic detector systems of MACRO, streamer tubes and scintillation counters, are very complementary. The amount of scintillation light produced was proportional to the energy loss in the scintillator and the light was produced promptly, so the scintillation counters had good energy and timing resolution. However, the high cost of the photomultiplier tubes used to detect the light limited the designers of MACRO to about 500 scintillator boxes.

The streamer tubes had poor timing resolution because of the drift time in the gas and poor energy resolution because of the digital nature of streamer formation. However, the low cost of plastic streamer tubes allowed MACRO to employ about 50,000 channels of streamer tube readout. In each streamer tube plane the wire

spacing was about 3 cm.

Therefore, to reconstruct a particle traversing the MACRO detector, the streamer tubes provide most of the position information, and scintillators provide the timing and energy information.

## 2.1 The Scintillator System

### 2.1.1 Scintillation Counters

The scintillation counters were boxes of opaque PVC, filled with a liquid scintillator consisting of a base of mineral oil with a 6.2% admixture of scintillator concentrate. The concentrate consisted primarily of pseudocumene (1,2,4-trimethylbenzene) with small amounts of PPO (2,5-diphenyl-oxazole) and bis-MSB (p-bis[o-methylstyryl]benzene). The mineral oil had high transparency and purity, allowing scintillation light to propagate several meters. At the end of each box was an endchamber separated from the scintillator by a clear PVC window. One or more photomultiplier tubes (PMTs) were placed in the endchamber to detect scintillation light. Each endchamber was filled with pure mineral oil to optically couple it to the scintillator and to reduce sparking of the phototube high voltage system. A mirror of shaped, aluminized PVC around each phototube increased its light-collection efficiency. (See Figure 2.4.)

The boxes of scintillator lived in layers. *Horizontal* boxes were found in the Bottom (B), Center (C) and Top (T) layers. Horizontal boxes were about 12 m long, 75 cm wide and filled to a depth of 19 cm with liquid scintillator. Horizontal boxes had two PMTs in each end, but the outputs were immediately summed and treated as a single channel in the electronics. *Vertical* boxes lived in the vertical faces. The West (W) and East (E) faces were along the long axis of MACRO. The North (N) and South (S) faces were instrumented only on the lower part of the detector to allow convenient access to the hollow part of the upper detector (refer back to Figure 2.2). Vertical boxes were about 12 m long, 21 cm wide and filled to a depth of 43 cm with

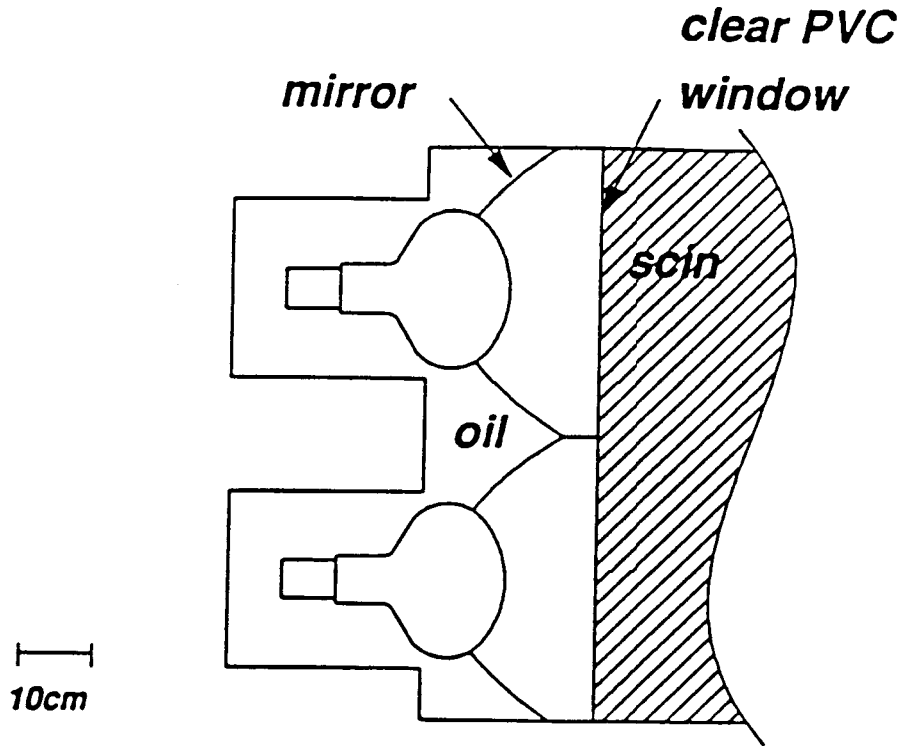


Figure 2.4: A scintillator box endchamber.

scintillator. They had only one phototube in each end. The speed of light in the scintillator was about  $0.7c$  so light could travel from one end of the box to the other in about 60 ns.

Scintillator boxes also had a light-emitting diode (LED) near each phototube and a laser fiber that could deposit laser light near the center of the tank. LED or laser light was introduced only during special calibration runs (to be discussed in Section 2.3.2).

Each scintillator box is referred to by a unique four-character name based on its location in MACRO. For example, the seventh tank in the Bottom (B) layer of the third supermodule is referred to as 3B07. The two ends of the box are referred to as the 0- and the 1-end, so a box end is referred to by a name such as 3B07-1. Each box is also identified by a unique integer as detailed in Table 2.1.

boxes	SM1	SM2	SM3	SM4	SM5	SM6
B01-B16	001-016	101-116	201-216	301-316	401-416	501-516
C01-C16	017-032	117-132	217-232	317-332	417-432	517-532
W01-W07	033-039	133-139	233-239	333-339	433-439	533-539
E01-E07	040-046	140-146	240-246	340-346	440-446	540-546
N01-N07	047-053	-	-	-	-	-
S01-S07	-	-	-	-	-	547-553
T01-T17	054-070	154-170	254-270	354-370	454-470	554-570
W08-W14	071-077	171-177	271-277	371-377	471-477	571-577
E08-E14	078-084	178-184	278-284	378-384	478-484	578-584

Table 2.1: Numbering of scintillator boxes.

### 2.1.2 Scintillator Electronics

The phototube signals from each end of each scintillator box were fanned out to several electronic subsystems. The Energy Reconstruction Processor (ERP) was a self-triggering system of ADCs and TDCs for each box. Other electronic subsystems, not relevant to this analysis, included a gravitational collapse trigger, a slow-moving monopole trigger, a two-face coincidence detector and a waveform digitizing system.

There was a different ERP system for each supermodule of MACRO. (For ERP purposes, the North face and South face each constituted a supermodule, so there were a total of eight ERP systems.) For each box in the supermodule, the ERP had two ADCs and two TDCs for each end (a total of four ADCs and four TDCs per box). One of the ADCs saw an input that was attenuated by a factor of ten compared to the other; the unattenuated ADC often saturated to its maximum count of 4095 on muon-level phototube pulses. All TDCs in a supermodule shared a common stop. One of the TDCs had a lower threshold to generate a TDC start. On most events the two TDCs started at almost the same time but occasionally a small signal could start the low-threshold TDC without starting the high-threshold TDC. The eight measurements for each box are summarized in Table 2.2.

ERP activity for a box began when a signal crossed a front-end threshold (typically around 100 mV) and started the TDC for that box. If both box ends crossed threshold within 200 ns, this coincidence was called a minimum bias trigger (MBT). When

name	description
ADC0U	0-end unattenuated ADC
ADC1U	1-end unattenuated ADC
ADC0A	0-end attenuated ADC
ADC1A	1-end attenuated ADC
TDC0H	0-end high-threshold TDC
TDC1H	1-end high-threshold TDC
TDC0L	0-end low-threshold TDC
TDC1L	1-end low-threshold TDC

Table 2.2: ERP signals for each box.

the MBT occurred, delayed versions of the input signals were gated onto an ADC capacitor for 200 ns. The common stop for all TDCs occurred about 400 ns after the first MBT in the supermodule. If no MBT occurred within 200 ns of a TDC start, the event was ignored and the circuitry was cleared.

Even if an MBT occurred, the event could be rejected. The circuitry waited until charge integration was complete, and then estimated the energy of the event based on the unattenuated ADC values at both ends. (The estimate was done using a pre-stored lookup table, indexed by 6-bit non-linear flash ADCs that digitized the integrated charge from each tankend.) If the estimated energy exceeded a trigger threshold the acquisition was triggered and the event was held to be read out. If the energy was too low the event was rejected and the circuitry was cleared. Note that activity in a single box was sufficient to trigger the acquisition. The acquisition read out all boxes that had sufficient energy to trigger.

There were actually two different energy trigger thresholds, sometimes called Ehigh and Elow, and sometimes called muon and GC (gravitational collapse) respectively. For the events considered in this analysis, at least one box had the more stringent (muon-level) trigger, but all boxes in that supermodule that passed at least the GC level were read out.

Channels in different supermodules had a different common stop. If a particle crossed a supermodule boundary, one cannot reconstruct the timing using ERP information alone. However, the stop signal for each supermodule was sent to a CA-

MAC TDC called the interERP TDC. By using the interERP TDC one can relate the timing in different supermodules and reconstruct the timing for the whole event.

## 2.2 Streamer Tubes

A MACRO streamer tube consisted of a 12 m long wire at high voltage (typically 2.5 kV) in a gas chamber of cross section  $3\text{ cm} \times 3\text{ cm}$  formed by graphite-coated plastic at ground. Primary ionization from the passage of a high energy charged particle led to the formation of a streamer which migrated to the wire, producing a pulse of current on the wire. All the streamer tube planes except those in the lower vertical walls were also equipped outside the gas cell with pickup strips at some angle to the wires ( $26.5^\circ$  in horizontal planes and  $90^\circ$  in vertical planes). The strips picked up an oppositely-charged pulse by induction when a streamer formed under them. Wires and strips had a pitch of about 3 cm.

The wires and strips that resided in horizontal planes are called central wires and strips, those on the East and West vertical walls are called lateral wires and strips, and those on the North and South vertical walls are called frontal wires (recall there are no strips on the lower lateral or the frontal planes).

The streamer tube electronics used in this analysis provided simply the digital information of which wires and strips had a pulse above 40 mV threshold within  $10\ \mu\text{s}$  of the trigger. Offline software uses this digital information to construct tracks in various views (such as the central wire view, the central strip view, the lateral wire view, etc.). If one can unambiguously associate tracks in two or more different views one can reconstruct the tracks in three dimensions.

Specifically, to reconstruct a track in the central wire or strip views, the standard MACRO tracking software (used throughout this analysis) requires four or more collinear hits. The lateral tracking is more complicated. In addition to the wire hits in the lateral planes, which provide a hit in the (Y,Z) view, the tracking also pairs central wire hits with central strip hits in the same plane to form more (Y,Z) candidate coordinates. To reconstruct a lateral track, the software requires a total of

at least 5 collinear hits, of which at least 3 must be on lateral wires. If there are 5 or more lateral hits, no central hits are required. In this analysis, frontal wires and lateral strips are not considered for tracking.

Other electronics, not relevant to this analysis, recorded the digital information of hits in a much-longer time window, and also recorded (with limited precision) timing and charge information for each streamer.

Further technical details on the scintillator and streamer tube systems may be found in References [55] and [56].

## 2.3 Calibrations

As will be detailed in Chapter 5, the heart of the experimental analysis is the recognition of upgoing muons using the time of flight (TOF) in the scintillator system. The scintillators were intrinsically capable of subnanosecond timing resolution. However, box-to-box variations and week-to-week variations made a weekly calibration procedure critical to the success of the analysis.

### 2.3.1 Timing Reconstructions

All timing reconstruction is done using the ERP TDCs for the hit channels. Within a single supermodule, all TDCs received a common stop. The time of phototube activity at a tankend is reconstructed as

$$\text{TIME}_i = (TDC_i + \text{TWC}) * \text{TICK} + \text{TOFF}$$

where

$$\text{TWC} = \frac{\text{TWC1}}{\sqrt{\text{ADC}_i}} + \frac{\text{TWC2}}{\text{ADC}_i}$$

is a timewalk correction which corrects for the fact that if two pulses begin at the same time, the pulse of lower amplitude will cross threshold later and thus start the

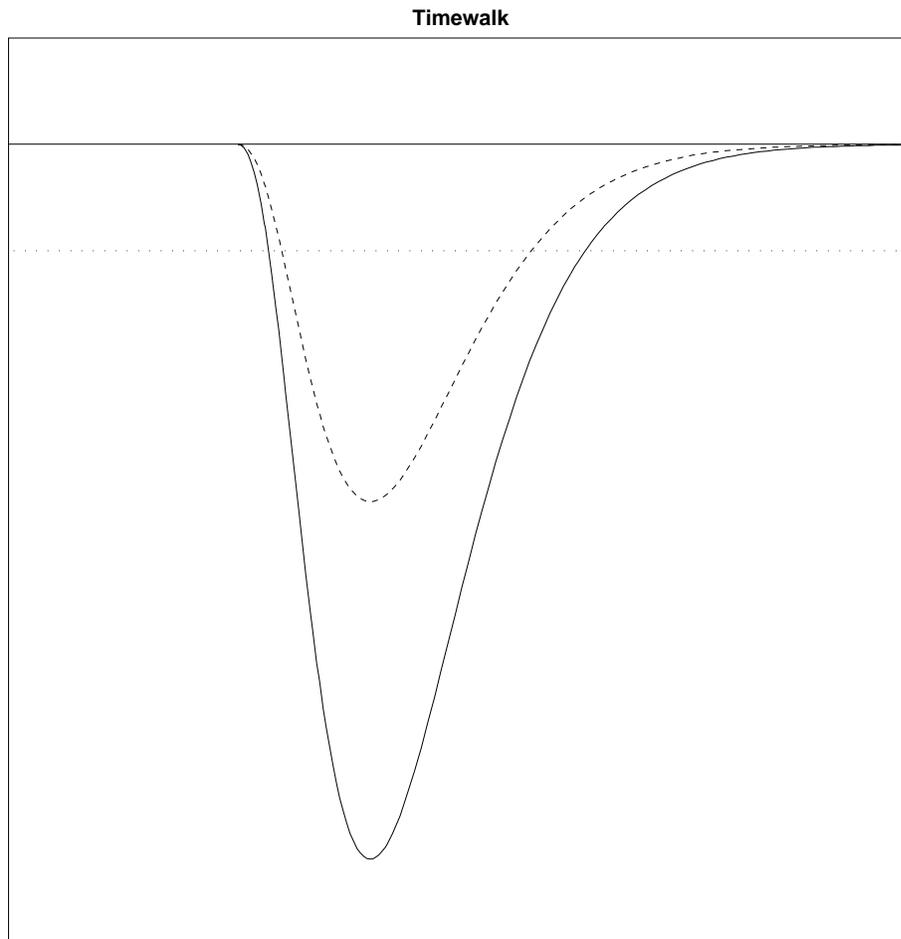


Figure 2.5: An illustration of timewalk. A large pulse and a small pulse are superposed, beginning at the same time. The small pulse crosses the TDC start threshold (indicated by the dotted line) later than the large pulse.

TDC later (see Figure 2.5). In the above,  $i$  indicates the 0- or 1- tankend,  $TDC_i$  and  $ADC_i$  are the measurements from ERP and TICK, TOFF, TWC1 and TWC2 are calibration constants, determined separately for each channel of each box on a weekly basis.

In calculating TOF, the time of light propagation within a scintillator box cannot

be neglected. For a z-axis along the long dimension of a box, with the origin at the center of the box, if a particle passes through the box at location  $z$ ,

$$\begin{aligned}
 TIME_0 &= T + \left(\frac{L}{2} + z\right)\frac{n}{c} \\
 TIME_1 &= T + \left(\frac{L}{2} - z\right)\frac{n}{c} \\
 T &= \frac{TIME_0 + TIME_1}{2} + const \\
 z &= \frac{TIME_0 - TIME_1}{2} \frac{c}{n}
 \end{aligned} \tag{2.1}$$

where  $T$  is the time the light is produced,  $L$  is the box length, and  $\frac{c}{n}$  is the speed of light in the oil. So the difference in meantimes of two boxes gives the time of flight between the two boxes, independent of  $z$ .

Most events involve ERP hits in only one supermodule, and the above ‘‘intraERP’’ reconstructions are all that is needed to determine the relative timing of all scintillator hits. However, when scintillators fired in more than one supermodule (and recall that for ERP purposes, the North face and the South face are each a supermodule unto themselves), an interERP adjustment must be made. Two types of information are available: each ERP system provides data about when each box in that supermodule fired relative to the common stop signal on that supermodule, and the interERP TDC system provides data about when the common stop on one supermodule’s ERP system occurred relative to that on the other ERP system. The latter information can be reconstructed from the interERP TDCs using an interERP slope and an interERP offset for each supermodule. Putting the interERP and intraERP information together, the reconstruction equation is

$$\begin{aligned}
 \Delta T &= TMEAN_a - TMEAN_b + (IETDC_a * IESLOPE_a + IEOFF_a) - \\
 &\quad (IETDC_b * IESLOPE_b + IEOFF_b)
 \end{aligned}$$

where the IE (interERP) terms give the difference between the common stops on the

two different supermodules. Here  $TMEAN$  is the mean time calculated using the intraERP constants (see Equation 2.1),  $IETDC$  is the measured time in the channel of the interERP TDC corresponding to the hit supermodule, and  $IESLOPE$  and  $IEOFF$  are calibration constants.

In the case of more than two supermodules, or non-adjacent supermodules, it may or may not be possible to adjust the event with the interERP TDCs and calibrations that are available, as detailed in the following paragraphs.

Every pair of supermodules was read out by a different computer; often a pair of supermodules is referred to as a “microvax,” because three microvax computers (one for each pair of supermodules) were used to read out the equipment during runs. In this nomenclature, Microvax 1 is SM1 and SM2, Microvax 2 is SM3 and SM4, and Microvax 3 is SM5 and SM6. Generally, if all the triggers in an event were in SM1 and SM2, only Microvax1 would be read into the event record, etc.

Therefore, there was a different interERP TDC hardware module physically located on each microvax; in an event only read out by Microvax 1, the Microvax 1 interERP TDC would be read into the event record. With this TDC information, it is possible to reconstruct the interERP timing among the North face, SM1 and SM2 (recall that, while the North face is generally considered a part of SM1, it has a separate ERP system and so an interERP adjustment is required to reconcile ERP timing between the North face and other faces in SM1). There was a sufficient number of N/SM1 and SM1/SM2 events each week to calculate the necessary calibration constants, an interERP slope and an interERP offset for each supermodule (including the North face, 6 parameters in all). Similar considerations hold for Microvax 3 and the SM5, SM6 and South face ERPs.

With the exception of interERP, Microvax 2 was primarily responsible for reading out only SM3 and SM4; however, not only the common stop signals from SM3 ERP and SM4 ERP, but also a copy of the common stop signal from each of the other six ERP supermodules (N, SM1, SM2, SM5, SM6 and S), was fed into its own channel on the Microvax 2 interERP TDC. There was a sufficient number of SM2/SM3, SM3/SM4 and SM4/SM5 events each week to calculate an interERP slope and an

interERP offset for the four supermodules 2-5, eight parameters in all. Note that SM2 has one interERP slope and interERP offset for the hardware on Microvax 1, and a different interERP slope and interERP offset for the hardware on Microvax 2. For a SM2/SM3 event, both Microvax 1 and Microvax 2 triggered and read out their respective interERP TDCs, but only the Microvax 2 interERP TDC is useful to adjust the timing between SM2 and SM3 (because the Microvax 1 interERP TDC has no information about when the SM3 common stop occurred). With the interERP slopes and offsets determined from SM2/SM3 events and SM3/SM4 events, it is also possible to adjust an event with hits only on, for example, SM2 and SM4.

However, there were few events each week between N, SM1, SM6 or S and either SM3 or SM4. Thus, no calibrations are available for the Microvax 2 interERP slopes and offsets for those supermodules. Therefore, if an event occurred with ERPs fired in SM1 and SM4 only, the event cannot be adjusted. There is no information about SM4 in the Microvax 1 interERP TDC, and the information present about SM1 in the Microvax 2 interERP TDC is uncalibrated.

However, suppose SM2 also fired so there are hits in SM1, SM2 and SM4. The relative timing of SM2 and SM4 is known from the Microvax 2 interERP TDC and calibrations, while the relative timing of SM1 and SM2 is known from the Microvax 1 interERP TDC and calibrations. Thus, it is possible to use SM2 as a bridge to synchronize calibrated data from both the Microvax 1 interERP TDC and the Microvax 2 TDC:

$$t_{SM1} - t_{SM4} = (t_{SM1})_{MVAX1} - (t_{SM2})_{MVAX1} + (t_{SM2})_{MVAX2} - (t_{SM4})_{MVAX2}$$

### 2.3.2 Calibration Procedure

The calibration constants have been determined anew for every week the detector was in operation. For a given week, the inputs to the calibration process are all the clean, well-tracked single muons detected that week from the cosmic radiation, plus data from special runs involving laser and LED that were performed at the beginning

of the week. Actually, the special runs were not performed on all supermodules every week, so some of the constants might remain static for up to a few weeks at a time.

The special calibration runs were performed on one day a week, designated as Calibration and Maintenance Day. Any scheduled hardware interventions (such as replacements and repairs of electronics or phototubes) would occur first, and then the special calibration runs would occur, including the newly-installed hardware. The first normal run after maintenance and calibration was used to label the set of calibrations. For example, 2 Aug 1994 was a Calibration and Maintenance Day. After maintenance and calibrations were finished, the first normal run was Run 8035, beginning at 8:05 pm. Normal runs, with an average length of about 8 hours, continued for a week, until Run 8057 was stopped at 8:47 am on 9 Aug to begin maintenance and calibrations. The special calibration runs on 2 Aug, along with the muons collected in normal running from Run 8035 through Run 8057, are used to produce the calibrations that are subsequently used to reconstruct data in Runs 8035 through 8057. This set of calibration constants is referred to as Set 8035, or sometimes as Week 8035.

### **LED Calibrations**

LED calibrations relied on a programmable pulse generator. A digital trigger output was fed into an ERP channel (the so-called “LED fake box”) while an analog output was fed to the LEDs in many boxes. The time delay between the trigger output and the analog output was programmable. (The pulser could also fake monopoles in special runs not considered here.) An LED run typically consisted of 16 events at each of about 25 different delay settings ranging from 0 to 650 ns. For each event the fake box was the first to trigger, while the timing of other boxes relative to the fake box depended on the delay setting. For each TDC, and for each delay setting, the average TDC value is determined and plotted versus the programmed delay (see Figure 2.6); a linear fit is used to determine the TICK parameter.

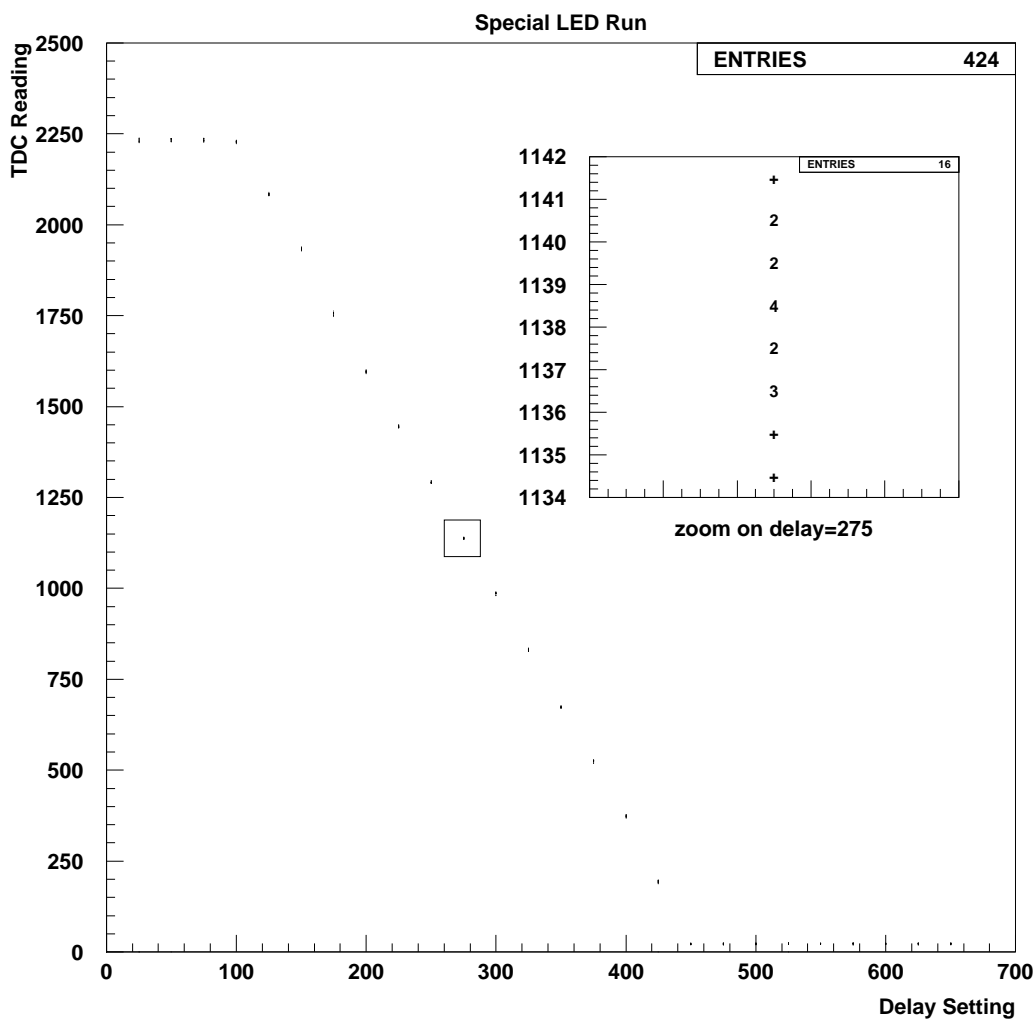


Figure 2.6: Determination of the TICK parameter. For a single box, for a single special LED run, TDC0H versus delay setting is shown. Each dot is one event. The boxed area is blown up in the inset, showing the typical spread in TDC values among the 16 events at a single delay setting. The parameter is determined by a fit to the linear portion of the graph.

## Laser Calibrations

One laser was fanned out through an optical splitter box and sent via optical fibers to many scintillator boxes. A computer-controlled attenuator wheel was programmed to reduce the light before it reached the splitter box. Two stand-alone photomultiplier

tubes measured the light before and after the attenuator wheel respectively. The unattenuated PMT was discriminated and the digital signal was fed into a channel of the ERP (the so-called “laser fake box” channel).

A laser run typically consisted of 50 pulses at each of about 20 attenuator settings. In addition to energy calibrations (not used in this analysis) the laser events are used to determine the timewalk constants. The fake box was the first ERP channel to trigger on each event, and its timing was independent of the attenuator setting. However, the timing of the other boxes relative to the fake box depended on the amplitude of the pulse (due to timewalk) and thus varied with the attenuator setting. For each TDC channel, at each attenuator setting the average ADC and average TDC are determined, and the timewalk constants TWC1 and TWC2 are determined to make the corrected TDC independent of attenuator setting.

This procedure is underconstrained; there may be many choices for TWC1 and TWC2 that give the right curvature. The different choices may give different values for the corrected TDC value, but that can be accommodated by the TOFF offset constant. In practice, if the timewalk constants are determined anew every time a laser calibration run is available, each of the TWC1, TWC2 and TOFF constants may show considerable variation from week to week even when the apparatus is fairly stable; the differences arise from random fluctuations in the underconstrained timewalk determination. Therefore, we chose to update the timewalk constants very rarely. Figure 2.7 shows the performance of the timewalk correction in a laser run that was taken a couple of years after the timewalk constants were determined.

## **Muon Calibrations**

During each week, clean, well-tracked single muons were collected. From the streamer tube tracks, the position within hit tanks and the flight path between tanks is determined. TOFF constants are determined in a two-step procedure, making use of the TICK and TWC constants already determined from the special runs.

First, the timing within a single tank is considered. A linear fit is made to a plot of reconstructed time difference between the two tank ends versus the position

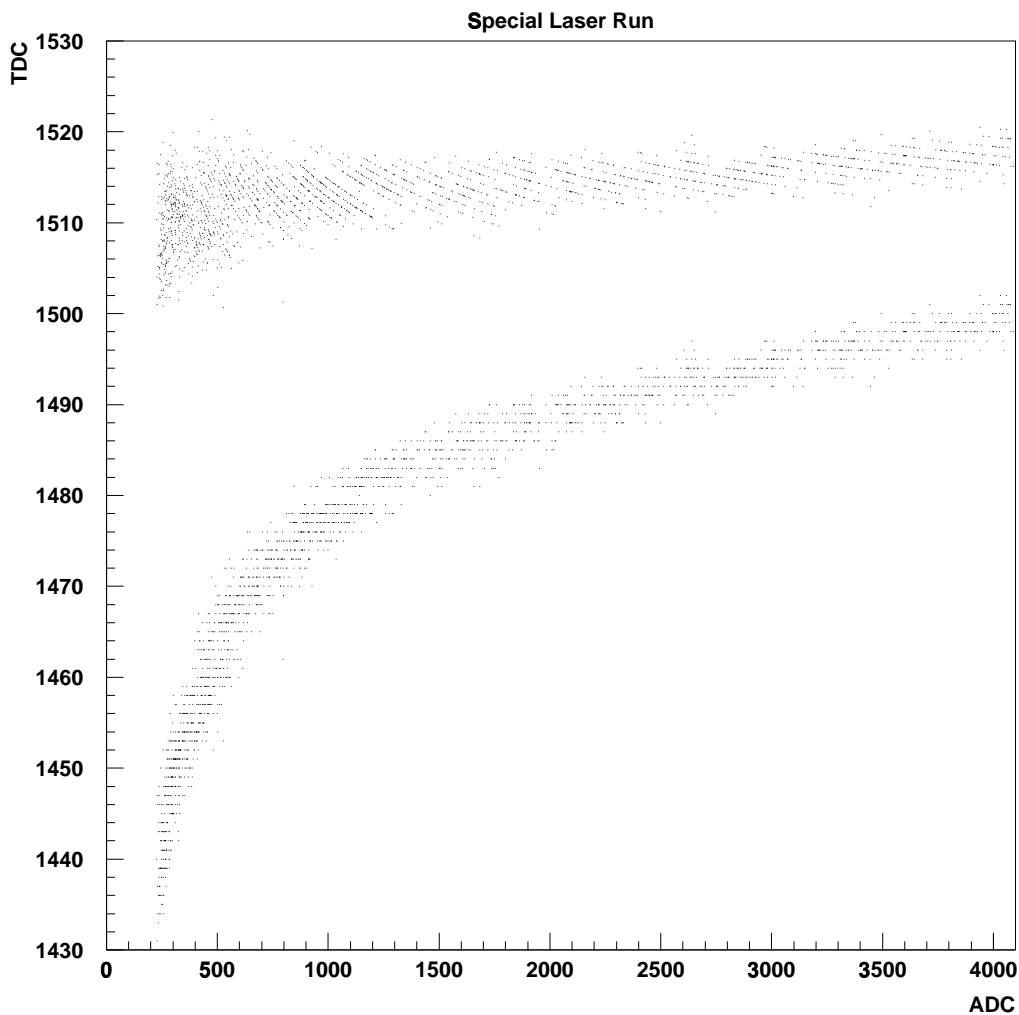


Figure 2.7: Determination of timewalk constants. The data shown are for a single channel, for a single special laser run. The lower set of dots gives the raw TDC values versus ADC values. The upper set of dots gives the corrected TDC values using the parameters  $TWC1 = 1163$ ,  $TWC2 = -1745$ . Each TDC count represents around  $1/6$  ns.

determined from tracking (see Figure 2.8). The fit parameters give the effective speed of light within the tank and the relative difference between the TOFFs for the two ends of the tank.

After this initial adjustment of TOFF, time of flight between boxes is considered

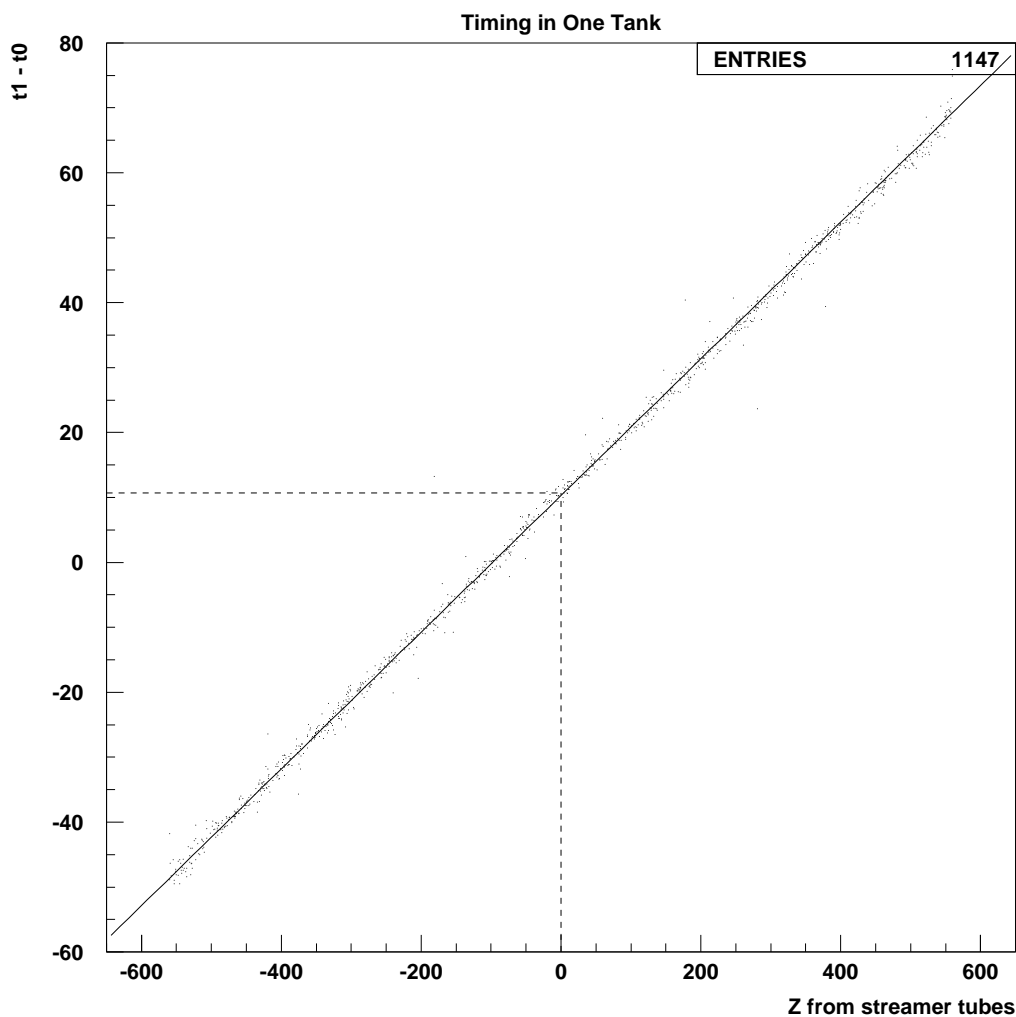


Figure 2.8: Timing within a single tank. The data shown are for a single channel, for a week of muons. Each dot is one event, with the x coordinate given by the point a streamer tube track intersects the 1200 cm tank; 0 is the center of the tank. The y coordinate is the difference between the reconstructed time on the -0 end of the tank and the -1 end, before the offset is corrected. The reciprocal of the slope gives twice the effective speed of light in the tank, while the intercept shows the amount that must be added or subtracted to the TOFF constant on one end.

to determine the offsets of the various boxes relative to one another. An iterative procedure is used. Using an initial guess for the offsets (the results of the previous week's fit, modified by the results of the single-tank offset adjustment), the velocity

of every particle is reconstructed. If the mean computed velocity of particles hitting a certain tank is not equal to  $c$  (the sample is dominated by downgoing relativistic muons), the offset constant for that box is adjusted to reposition the mean to  $c$ . This will affect the calculated velocities of all events that hit that box, and feed back to affect the mean velocity calculated for boxes in other planes. The iteration continues until the mean velocity for all boxes is within a tolerance (typically 0.001) of  $c$ .

### **InterERP Calibrations**

After the intraERP constants are all determined using events that do not cross supermodule boundaries, then interERP events from the weekly sample of clean, well-tracked muons are used to determine the interERP constants (a slope and an offset for each supermodule). An optimization is performed using the CERNLIB computer code MINUIT [57] in which IESLOPE and IEOFF are allowed to freely vary to minimize the Mean Squared Error (that is, to minimize the sum over all events of the square of the difference between reconstructed and expected time-of-flight).

The North and South faces each had an independent ERP system. As with other supermodules, their TICK and TWC constants can be determined using the laser and LED runs, and the relative TOFF difference between the two ends of each box can be determined using muon tracks that intersect each box. All of these quantities are known before interERP calibrations begin. However, because these ERPs hosted only one plane, there are no multi-plane intraERP events to use to determine the relative TOFF constants between different boxes in the North or South face. Therefore, TOFF constants for each box in the North and South faces are also variables to be determined by the interERP MINUIT fit.

## Chapter 3 Monitoring and Modeling the Detector

### 3.1 Muon Analysis

With the exception of small effects (due to electron neutrino interactions or nuclear recoil), this analysis is essentially an analysis of muons in the MACRO detector. Atmospheric muons (muons produced in the atmosphere by cosmic ray showers) reached the detector at the rate of about  $10^4$  per day. Neutrino-induced muons produced outside the detector reached the detector about once every few days, while the semi-contained neutrino-induced muons which are the subject of this analysis were created once every few weeks. Therefore, the starting point for this analysis is a procedure for identifying and characterizing muons in the detector. Furthermore, the health of the detector hardware can be monitored as a function of time via the muon analysis applied to the copious atmospheric muons.

In addition to the measurement of semi-contained upgoing muons which is the aim of this analysis, the analysis also uses studies of downward throughgoing muons and downward stopping muons to monitor the detector. All of these analyses are extremely similar and, utilizing a modular software environment, parts of the different analyses are executed by the same code. Here will be given a very brief overview of the downward throughgoing analysis, necessary to understand the rest of this chapter. The semi-contained upgoing muon analysis will be described in much more detail in Chapter 5.

When a single event is analyzed, utilizing reconstructed streamer tube tracks (see Section 2.2), information from at least two views (wire, strip, or lateral) is combined to define a track in three-dimensional space (a “space track”). Next, two or three scintillator boxes that lie on the track or very near it and that triggered in the event

are identified and associated with the track. If a space track cannot be created from the single-view tracks in the event, or if there are not two scintillators that fired along a space track, the event is rejected. Otherwise, after a few more cuts to ensure the quality of the data in the event, the time of flight between two scintillator hits is determined using the timing reconstructions (see Section 2.3.1), and the pathlength between the two hits is determined by using the reconstructed position along the box, along with a database of the positions of all scintillator boxes. (If there are more than two boxes associated with the track, the two with the largest separation are used to characterize the event.) From these a velocity can be determined which will be represented by the value  $\beta \equiv \frac{v}{c}$ , with the convention that downgoing particles have positive  $\beta$  and upgoing particles have negative  $\beta$ . The vast majority of muons in MACRO have  $\beta$  very near unity. A sample of downgoing muons can be created by selecting from those events passing all cuts only the events with  $\beta$  near +1.

Another quantity, **tError**, can be defined as the difference between the measured time of flight and the time of flight that would be expected for a relativistic particle traversing the same pathlength. When the apparatus is well-functioning and well-calibrated, **tError** values cluster near zero. Unlike  $\beta$ , the experimental error on the measurement of **tError** is almost independent of pathlength.

Most detected muons, whether upward or downward, originate outside the detector, and traverse the entire detector to stop somewhere on the other side. We may create a sample of muons that originate in the detector (if they are upgoing) or stop in the detector (if they are downgoing) by selecting events with incomplete tracks; that is, tracks whose continuation strikes several streamer tube channels that did not fire. The exact algorithm will be detailed in Chapter 5.

Applying these analyses to all events in the dataset yields 24,000,000 downward muons (a rate of about ten per minute) of which 210,000 stopped (a rate of about one every ten minutes). There are also about 690 externally-produced upward muons identified (about one every two days), and a refined version of the analysis (described in Chapter 5) finds 76 identifiable semi-contained neutrino-induced upward muons (about one every three weeks).

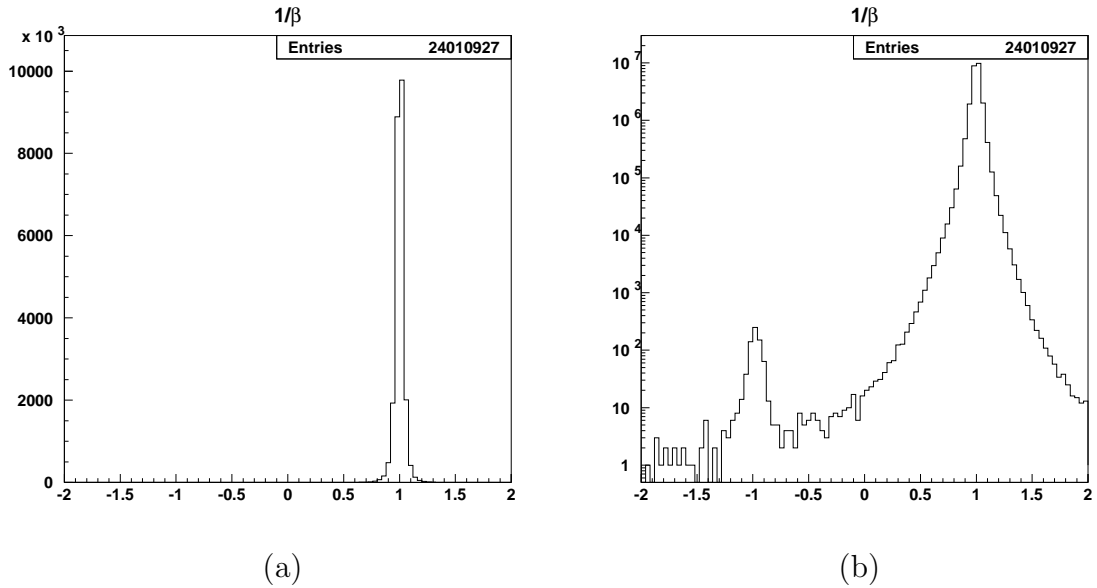


Figure 3.1: The distribution of  $1/\beta$ . Downgoing events are at  $\beta = +1$  and upgoing at  $-1$ . (a) is on a linear scale and (b) is logarithmic.

Figure 3.1 shows the distribution of the quantity  $1/\beta$  for all events passing a simple muon analysis. (For fixed pathlength, the error in  $1/\beta$  is proportional to the error in the measured time of flight; hence, the experimental data is often presented as a distribution of  $1/\beta$ .) Note that published MACRO analyses on upward throughgoing muons use a more sophisticated analysis which eliminates more mistimed events.

## 3.2 Microcuts: Eliminating Bad Channels from the Analysis

Using the calibrations generated as detailed in Section 2.3, the timing can be reconstructed reliably in most boxes most of the time. However, due to hardware problems or errors in the calibration software, results for a certain box may be unreliable for a specific period of running time. Because there were more than  $10^5$  potential background events (downgoing atmospheric muons) for each signal event, it is necessary

to eliminate any box from the analysis if its timing was not reliable. This causes a small loss of acceptance for the analysis, but pays off with a big increase in data quality. These cuts are referred to as *microcuts*.

It makes sense to compute the microcuts on a weekly basis. That is, when reconstructing the data for each different week of running in the dataset, a different list of boxes to be eliminated is in effect. At the lab, most hardware interventions took place on designated “Calibration and Maintenance Days.” The calibration constants are produced on a weekly basis, to be in effect from one Calibration and Maintenance Day to the next. So problems due to bad calibration constants or bad hardware often began and/or ended on Calibration and Maintenance Day.

The microcuts are all determined empirically by looking at the real data, in particular at the distribution of **tError** (defined as the difference between measured time-of-flight and expected time-of-flight assuming downgoing relativistic particles) for events passing all cuts of the standard muon analysis. When a box was operating well and is well-calibrated, **tError** is distributed symmetrically about zero with an RMS on the order of a nanosecond. For each box, a decision is made for each calibration period (usually one week) whether to apply a microcut. Figure 3.2 shows the value of **tError** for each event for a single week of running, as a function of box number (recall Table 2.1). Figure 3.3 shows the value of the mean and the RMS of the **tError** distribution for each box-week (i.e., each of 476 boxes has one entry for each of 262 calibration periods, except for a few boxes that were completely dead for some weeks). A box is cut (by a microcut) for any week in which the box’s **tError** distribution has a mean more than  $\pm 3$  ns from zero, or an RMS of more than 2.7 ns. Furthermore, there are weeks in which all the boxes have a good mean and RMS, but in a particular supermodule there is an unusually high number of “outliers,” events with **tError** of more than  $\pm 15$  ns. Any week when a supermodule shows more than ten events in the outlier region (after the microcuts for individual bad boxes in that supermodule have already been applied), the entire supermodule is cut for that week. Figure 3.4 shows the box-weeks that are cut by these criteria. They are not randomly distributed; out of 1004 box-weeks cut, 98% of the cuts fall into one of two categories:

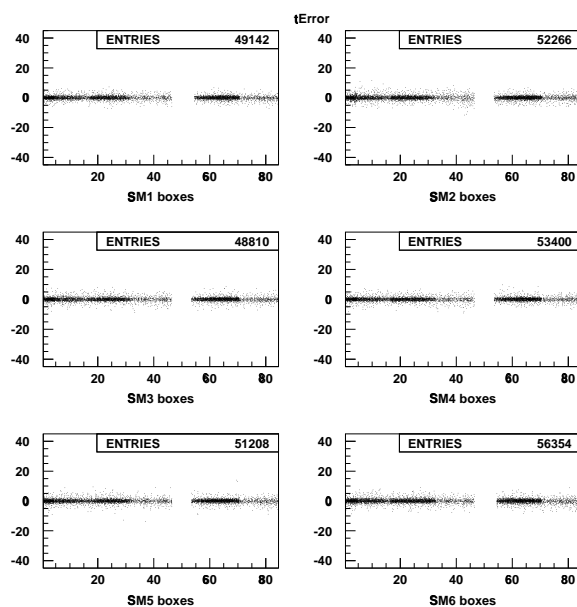


Figure 3.2: Scatter plot of  $t\mathbf{Error}$  for every box. For every event, two dots are plotted:  $+t\mathbf{Error}$  for the entry box, and  $-t\mathbf{Error}$  for the exit box. All of the events for a typical week are plotted. The gaps from 47-53 are because the North face and South face boxes are not shown here; they are handled in the interERP microcuts.

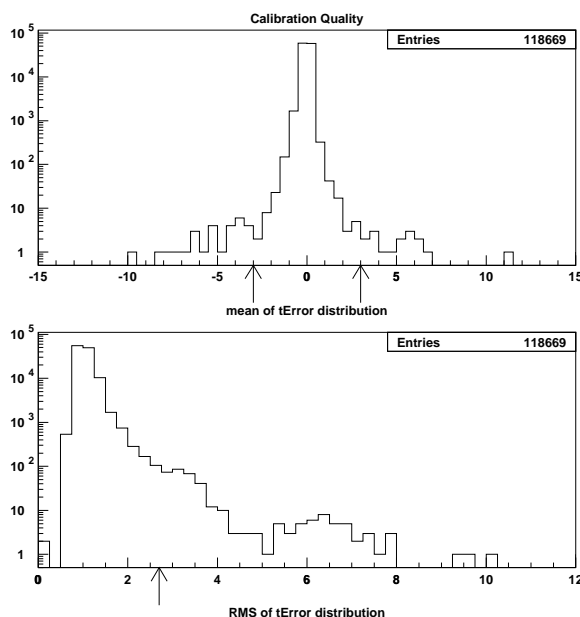


Figure 3.3: Distribution of means and RMS of the  $t\mathbf{Error}$  distribution, for all boxes and all weeks. The arrows show the locations of the microcut criteria. Note the logarithmic scale.

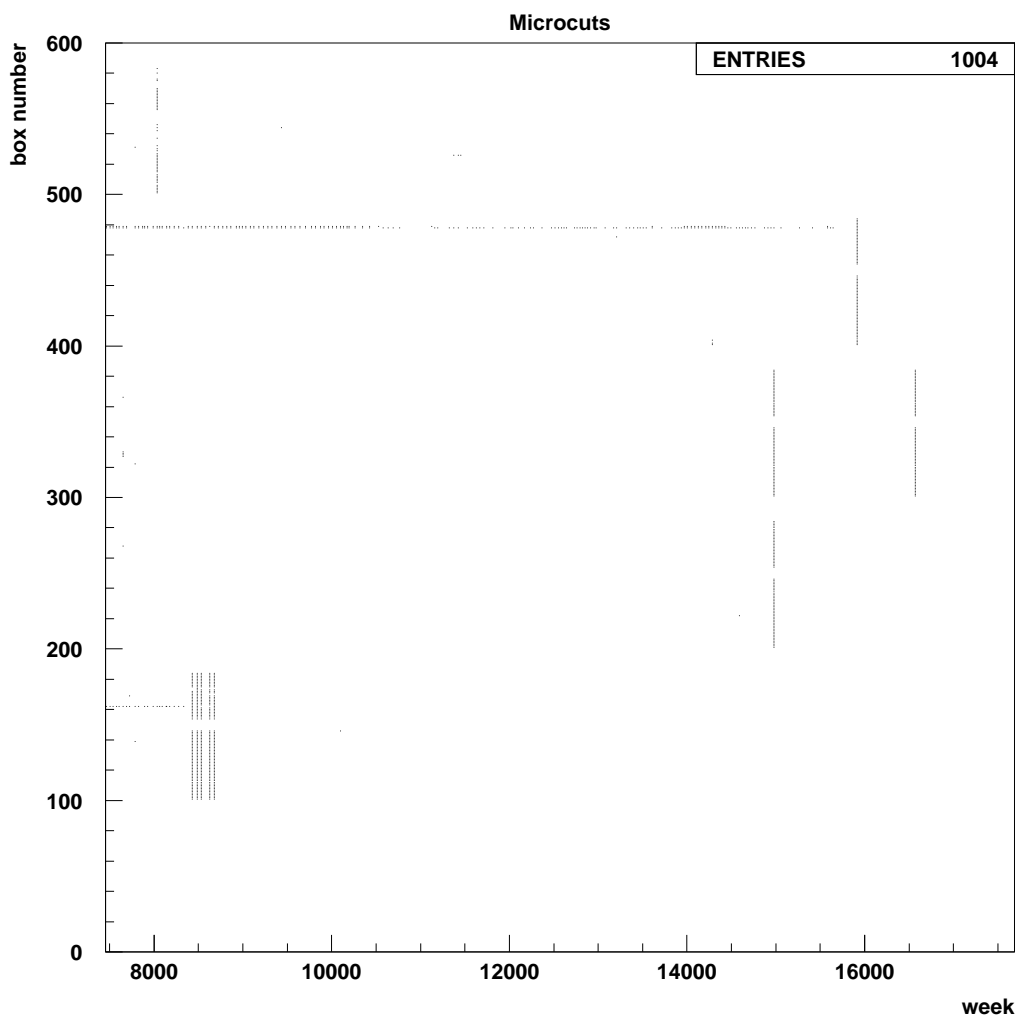


Figure 3.4: Box-weeks eliminated by microcuts. The vertical axis is the identification number of the box eliminated (see Table 2.1). The horizontal axis is the run number labeling the calibration week during which the box was eliminated.

- Ten cases of entire supermodules cut. In SM-weeks SM6-8035 and SM4-14978 almost every box had a bad mean and RMS. In SM-weeks SM2-8430, SM2-8487, SM2-8534, SM2-8628, SM2-8677, SM3-14978, SM5-15194 and SM4-16571 the majority of the data was good (boxes had good mean and RMS) but there were an excessive number of outliers.

- Three particular boxes had problems for extended periods of time. Boxes 478 (5E08) and 479 (5E09) were bad throughout the first four years of the running period (actually, RMS was near the cut so the boxes are marked as bad for most weeks, but survive the cut for some weeks). These boxes became normal after a hardware intervention in 1998. Box 162 (2T09) was bad during the first several months of the running period.

Only 20 other box-weeks are cut. All told, less than 0.1% of all box-weeks are cut.

Similarly, due to hardware or software failures, interERP events could not be reliably reconstructed all the time, so additional microcuts are applied to interERP events. Because the North and South faces had their own ERP systems, there are 7 interERP pairs of adjacent “supermodules” – N/1, 1/2, 2/3, 3/4, 4/5, 5/6, and 6/S. Distributions of **tError** for all the events crossing a given pair in a week are accumulated, and the pair is cut if the mean of the distribution exceeds  $\pm 0.5$  ns, if the RMS of the distribution exceeds 1.5 ns, or if there are ten or more outliers more than  $\pm 15$  ns from zero. See Figure 3.5.

Serious malfunctions of the interERP hardware were common. The interERP microcuts eliminate 390 pair-weeks, which is 21% of all possible pair-weeks. All microcuts of both kinds reduce the number of downgoing atmospheric muons reconstructed from the dataset for this analysis by 0.5%.

### 3.3 Detecting Dead and Inefficient Channels

We will want to be able to calculate the event rate expected in the detector under certain hypotheses about the neutrino physics. To do so with the highest accuracy, we must be able to account for the effect of imperfections in the detector – channels that were dead or inefficient for some period of time.

Around  $10^5$  atmospheric (downward) muons traversed MACRO each week and are fully reconstructed by the nominal muon analysis. A scintillation counter was hit about every 10-30 minutes on average (depending on the type and location of the counter), and a streamer tube channel (defined as a unit of eight wires, about 25 cm

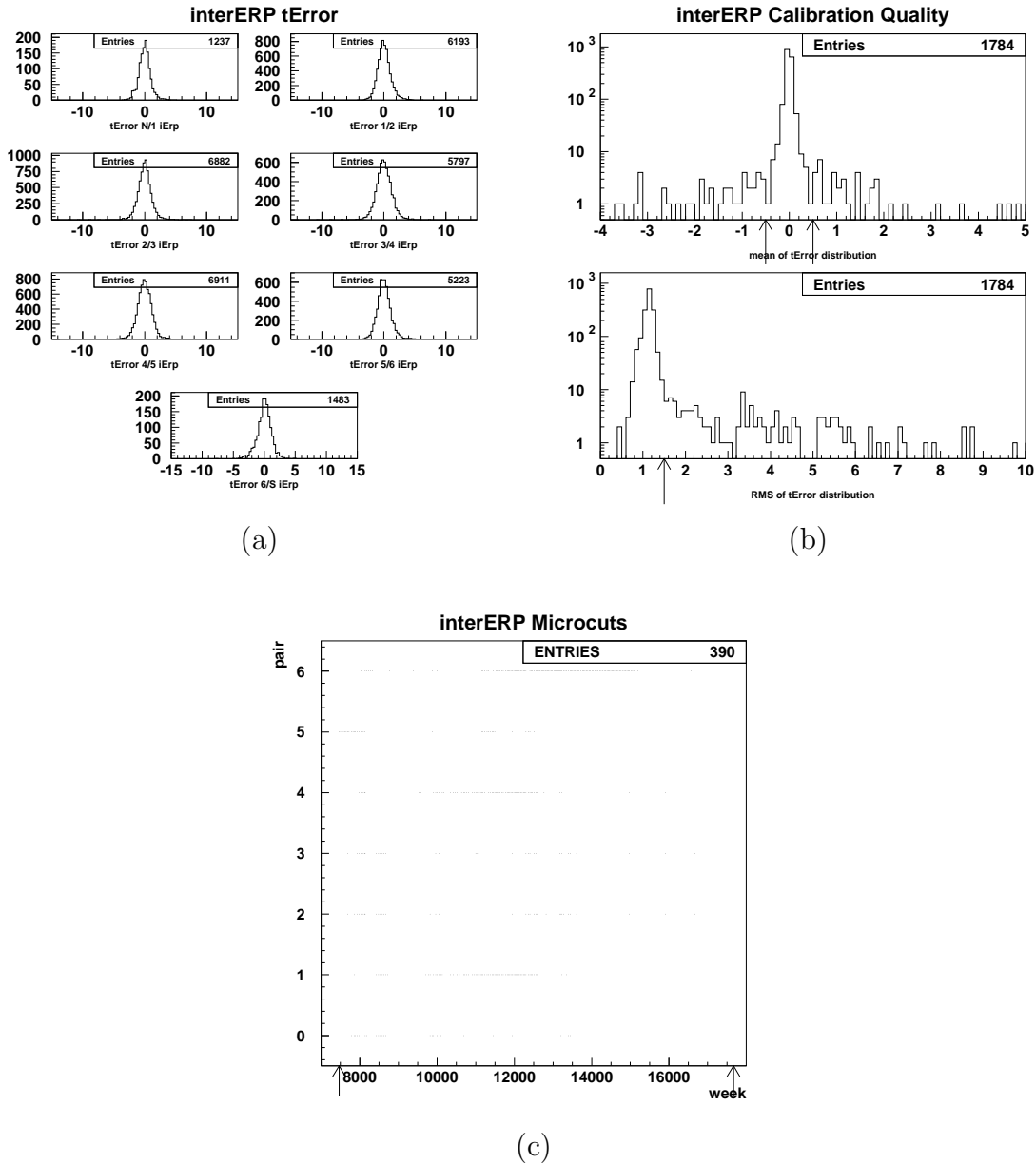


Figure 3.5: InterERP microcuts. (a) shows the distribution of  $tError$  for each of seven interERP pairs for a typical week's worth of data. (b) shows the distribution of mean and RMS for all pair-weeks. The arrows show the locations of the microcut criteria. (c) shows the pair-weeks that are cut by this microcut.

wide) was hit about every 30-100 minutes. These muons provide an excellent tool for monitoring the efficiency of every part of the apparatus as a function of time.

As with the microcuts, the efficiency is computed on a weekly basis. The number

of muons each week gives fairly good statistics for each channel, and, as discussed in Section 3.2, problems due to bad calibration constants or bad hardware often began and/or ended on Calibration and Maintenance Day.

Starting with events fully reconstructed by the standard muon analysis, we may define a *hit* as an event in which a given channel appears to be intersected by the muon track, and a *firing* as an event in which the channel was hit and it fired. However, to understand the efficiency of a channel, it is not enough to know just the ratio of firings to hits for a week. For example, if a channel were hit 100 times in a week and fired 50 times, there are a couple of extreme possibilities. The channel may have been 50% efficient all week; or it may have been completely dead for half the week and fully efficient for half the week. Also, it is worthwhile to keep track of exactly when a channel was dead because several channels may have been dead at the same time. A supermodule that was completely dead half the week and fully alive half the week would have a different efficiency than one that had part of the SM dead for the first half of the week, and the remaining part dead for the second half of the week.

There was a constant probability per unit time of a muon hitting a given type of channel, so the time between events is distributed exponentially (see Figure 3.6). For each type of channel a cut is defined that excludes less than 1% of the exponential part of the distribution. If a channel did not fire for a period of time exceeding the cut for that type of channel, the channel is considered dead during that period. Further statistical power is gained by considering not only individual channels, but also groupings of channels. For example, if a ten minute period elapsed during which no scintillator fired in an entire supermodule, we can be sure the supermodule was dead for those ten minutes – even though looking at each channel individually, a ten minute gap would not be long enough to be convincing evidence that the individual channel was dead.

After all the dead periods for each channel are identified, the efficiency (the ratio of firings to hits) is computed for each channel summing over all the non-dead periods of the week. For each channel a database stores the beginning and ending time of each dead period, as well as the efficiency for each week.

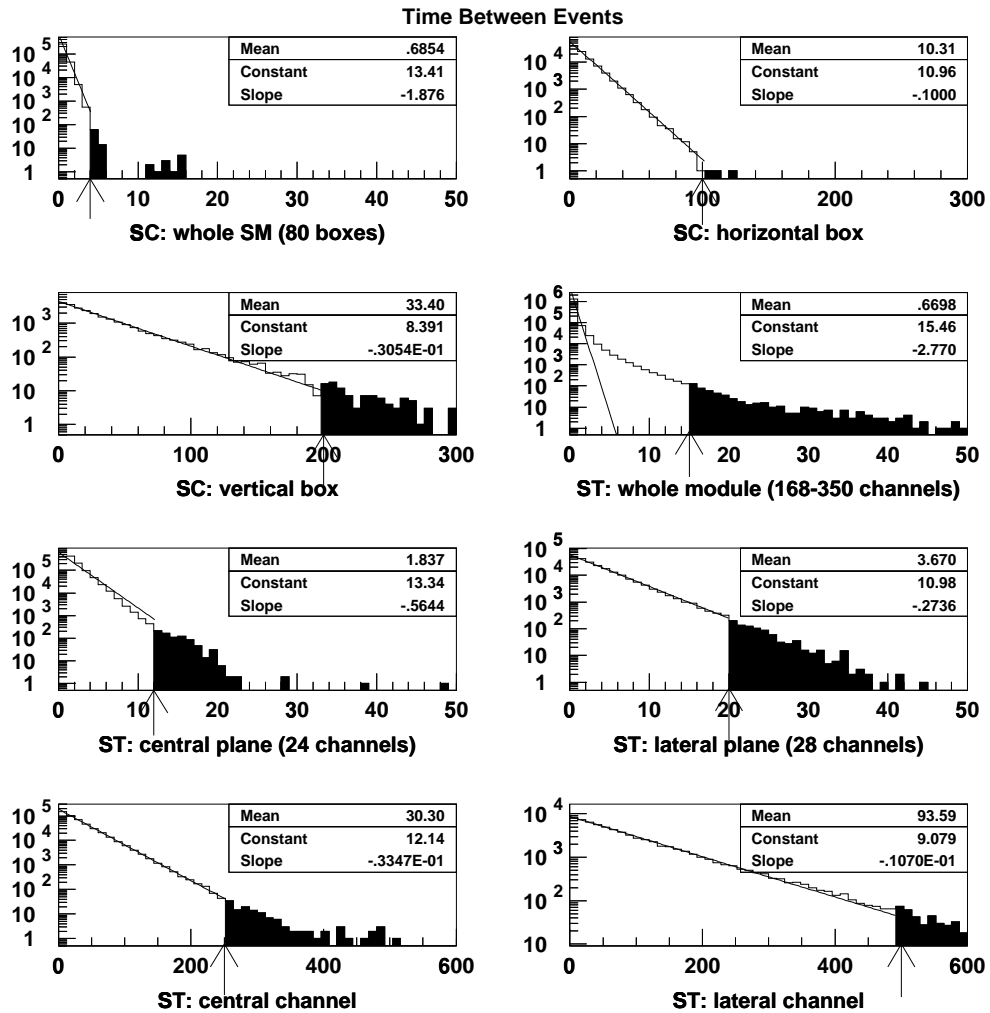


Figure 3.6: Distribution of time between events, with exponential fit, for different types of channels for a typical week. The arrows show the location of cuts; whenever a channel did not fire for a period of time greater than the cut, it was considered dead for that period. To the extent the distribution is truly exponential, the reciprocal of the fit slope is equal to the mean of the distribution, i.e., the mean time between events.

## 3.4 Detector Simulation

### 3.4.1 Why the Detector Must Be Simulated

We know (within the uncertainties to be detailed in Chapter 4) the flux of atmospheric neutrinos and the differential cross sections for neutrino interactions with neutrons, protons, and nuclei. And we know how muons and other particles created in neutrino interactions lose energy in matter and how our detector recorded energy loss. Therefore, it is possible in principle to compute what the apparatus would measure. However, all of these processes are very complicated; what practical strategy can one follow to calculate the prediction?

It is inherent within particle physics that we cannot predict exactly what will happen when a high-energy charged particle traverses matter. This is partly due to our ignorance – we do not know exactly where the molecules of matter are located or how close the high-energy particle will approach them – and partly due to the inherently probabilistic nature of quantum mechanics. While it is possible to analytically calculate average quantities (for example, the average energy loss per unit pathlength of a muon traversing Gran Sasso rock), one can calculate efficiencies and acceptance of complex experimental apparatus more accurately using an approach called Monte Carlo simulation.

In the Monte Carlo approach, we use a computer program to simulate the event of interest thousands or millions of times. For example, we may simulate 100,000 interactions of atmospheric neutrinos in the MACRO apparatus. For every high-energy particle produced by the interaction, the program “tracks” the particle through the apparatus. This means it propagates the particle forward one small step, then rolls the quantum mechanical dice to decide if it undergoes a hard interaction, losing significant energy and changing direction and possibly creating secondary particles, or if it merely loses a little energy and continues on. The program has a model of the geometry of the detector so that it may track the particle from one type of volume (say crushed rock) to another (say structural iron). If the particle is going through an active detector element (in MACRO, that means liquid scintillator or streamer tube

gas), the energy loss is recorded, and at the end of the event the program calculates what the detector would have recorded for that event.

For any one event, the results of the Monte Carlo are not reliable. For example, it might happen that a real neutrino of a certain energy and momentum interacts at a certain point in the real detector one day, producing an upgoing muon that hits two scintillators and is counted by the analysis software. However, if one were to simulate that interaction just once, it might happen that the upgoing muon chooses to undergo a hard interaction, changes course, and exits the detector through a crack. It is only on average, if one simulates tens of thousands of neutrinos of all energies and directions, interacting at all points in the detector, that one obtains a reliable estimate of the probability of detecting events of certain characteristics.

There is an implicit requirement of using judgment to formulate variables that are sufficiently generic to allow a meaningful comparison (in physics terms) between the Monte Carlo prediction and the physical measurement. Nature has given us only about 100 events in this analysis. There is no way a Monte Carlo program could predict, “There will be one event that originated in the 5th plane of the 4th Supermodule, hitting boxes 4C14 and 5W12; and one event that...” However, a Monte Carlo could accurately predict “Only 20% of the detected events will originate below the 5th plane.”

### 3.4.2 Geant and GMACRO

Geant 3.21 [58], part of the CERN Programming Library, is not so much a program as a set of facilities for creating Monte Carlo programs. It provides the following facilities (among others):

- **Detector Geometry.** Geant provides subroutines for defining the detector geometry, which will be used by the tracking package.
- **Physics Processes.** Geant allows various processes that may occur as high-energy particles traverse matter to be turned on or off, and parameters governing the processes to be varied.

- **Tracking.** A subroutine call can introduce a primary particle at an interaction vertex, and Geant will subsequently track the particle. As a result of the tracking, energy may be deposited in active detectors traversed by the primary particle, and secondary particles may be produced (which will subsequently also be tracked.)
- **Hits Management.** For detector volumes that are considered active volumes, Geant will keep track of all the energy deposited by all the primary and secondary particles. Geant makes this information available after tracking is finished, when the detector response is being calculated.

GMACRO is an extension of Geant customized for the MACRO detector. GMACRO includes calls to the Geant Geometry routines to define the MACRO geometry, as well as event generators to randomly create initial conditions for various classes of events (single atmospheric muons, multiple muons, isotropic muon flux, atmospheric neutrino-induced upgoing muons, etc.). Relevant generators will be discussed in a little more detail below. GMACRO also contains code to calculate how the actual MACRO detectors would respond to the energy loss determined by Geant. For the scintillators, GMACRO uses the time and amount of energy loss to compute whether a box would create an ERP trigger, and to compute the ADCs and TDCs that would be recorded in the ERP. (It does this by inverting the reconstruction equations from Section 2.3.1, utilizing a special calibration database filled with nominal values, identical for all boxes.) In streamer tubes, GMACRO probabilistically simulates the generation of streamers and the charge induced on streamer tube wires; simulates the charge induced on nearby strips; and determines which wires and strips are above threshold. Finally, GMACRO can write the output of each event in a format almost identical to that written for real events in the lab, so that both real and simulated data can be analyzed by the same analysis software. In addition to the simulated readout hardware values, the event record for GMACRO events also contains a record of “Monte Carlo truth values,” values known at the time the event is simulated that cannot be determined perfectly from the hardware. For example,

if the event is a simulated neutrino interaction, the energy of the parent neutrino is recorded in the event record.

The contained-neutrino interaction generator has a very central role in this analysis, and will be described in some detail in Chapters 4 and 5. Here is a brief description of two other GMACRO event generators that play a smaller role in this analysis.

### The Atmospheric Muon Generator

MACRO recorded the passage of several million atmospheric muons per year (compared to just a few hundred neutrino-induced muons) so the starting point to verify the accuracy of the simulation is to compare simulated atmospheric muons with real data. At the surface, the initial muon intensity goes approximately as  $\sec(\theta_{zen})$  where  $\theta_{zen}$  is the angle with respect to the vertical (the so-called *zenith angle*) – this approximation assumes a flat atmosphere, and is good to within about  $60^\circ$  of vertical. The energy distribution (for energies above 1 TeV, for which the muon has a chance of penetrating down to Hall B) is approximately a power law, going as  $E^{-3.7}$ , as derived from the power law distribution of primary cosmic rays reaching earth and the scaling laws governing shower evolution [59]. (These scaling laws will be elucidated a little further in Chapter 4, in the context of atmospheric neutrino production.)

The angular distribution of events reaching MACRO is determined not only by this initial distribution at the surface but also by the shape of the mountain. Obviously in directions where the mountain cover is thicker, a larger fraction of the initial atmospheric muons will range out and not reach the detector. An elevation map of the region around MACRO was incorporated into the GMACRO atmospheric muon generator, and iteratively corrected until now the mountain map is based on the observed muon intensity from each direction. In each direction, the generator computes the initial distribution and then applies an energy loss to that distribution according to the thickness of material. Figure 3.7 compares the zenith and azimuth distributions for real data and simulated atmospheric muons, for events passing the standard muon analysis. The figure suggests the simulation of acceptance as a function of angle is accurate. However, the energy spectrum at the detector is not entirely accurate.

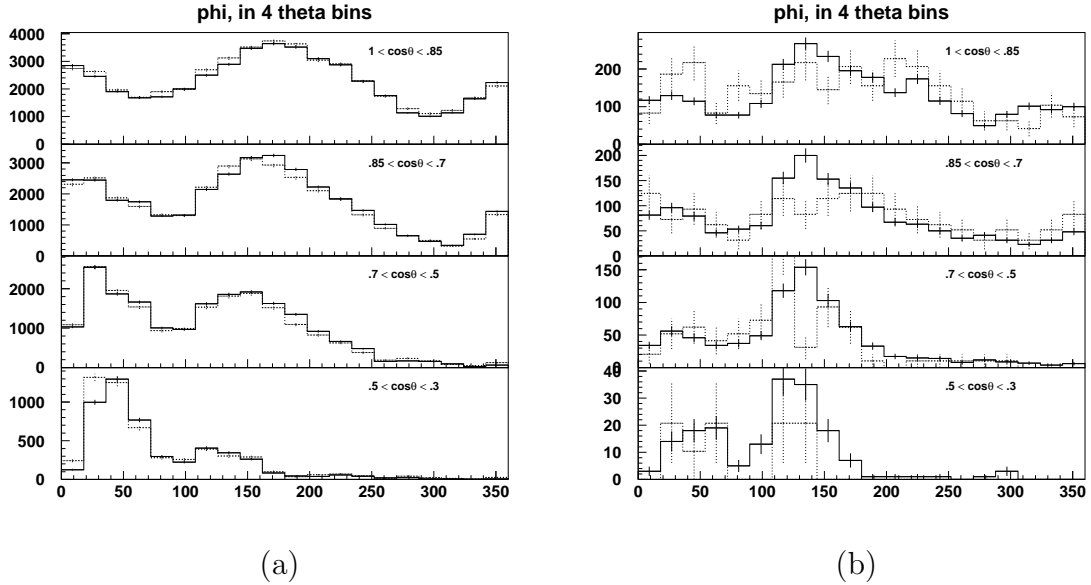


Figure 3.7: Comparison of the zenith and azimuth distributions of real data and simulated atmospheric muons. (a) All muons. (b) Stopping muons. Each graph shows the azimuth distribution for a slice of zenith angle values. Real data is represented by the solid line, simulated data by the dotted line.

Standard GMACRO uses a simple power-law spectrum of muons at the surface, but a more accurate, and harder, surface spectrum given by Gaisser [59] is

$$E_{\mu}^{-\gamma} \left\{ \frac{1}{1 + \frac{1.1E_{\mu} \cos \theta_{zen}}{115\text{GeV}}} + \frac{0.054}{1 + \frac{1.1E_{\mu} \cos \theta_{zen}}{850\text{GeV}}} \right\} \quad (3.1)$$

where the first term arises from pion decay and the second from kaon decay. Muons need about 1 TeV at the surface to reach MACRO; at that energy, the simple power law overestimates the vertical flux by 19%, while by  $E_{\mu} \cos \theta_{zen} = 1000$  TeV the power law is indistinguishable from Equation 3.1. Also, standard GMACRO propagates muons from the surface to the detector using average energy loss with no straggling. Using standard GMACRO, the ratio of identified stopping muons to muons passing the standard analysis (mostly throughgoing) is 0.78%, while in real data the ratio is 0.88%. Thus, the number of simulated stopping muons is too low by 11%. I modified GMACRO to implement Equation 3.1 at the surface, and to propagate the muons

to the detector probabilistically using the survival probabilities calculated for Gran Sasso rock by Bilokon, *et al.* [60]. This resulted in a stopping fraction of 0.83%, i.e., 5% fewer stopping muons in the simulation than in the real data. With only 527 simulated stopping muons, the error due to counting statistics on the simulated stopping fraction is 4.4%, i.e., the simulated stopping fraction is  $0.83\% \pm .04\%$ . In my judgment, the discrepancy in stopping rate can be entirely accounted for by counting statistics and uncertainties in the power law exponent and the Gran Sasso rock values of critical energy and length scale for radiative loss.

### The Upgoing Muon Generator

The upgoing muon generator used in this analysis, developed by MACRO collaborator Colin Okada, provides more detail in the Monte Carlo truth values than the standard generator distributed with GMACRO. The generator starts with a tabulated version of a published atmospheric neutrino flux calculation (see Chapter 4 for a discussion of what goes into a neutrino flux calculation). Ignoring any opening angle between the parent neutrino direction and the muon direction, as well as fluctuations in the energy loss of muons propagating through the rock toward the detector, we can semi-analytically transform the neutrino flux into an upgoing muon flux at the detector according to the equation

$$\frac{d^3\Phi_\mu(E_\mu, E_\nu, \Omega)}{dE_\mu dE_\nu d\Omega} = \frac{\rho N_A}{\frac{dE}{dx}(E_\mu)} \frac{d^2\Phi_\nu(E_\nu, \Omega)}{dE_\nu d\Omega} \int_{E_\mu}^{E_\nu} dE_\mu^\circ \frac{d\sigma(E_\nu, E_\mu^\circ)}{dE_\mu^\circ}$$

where  $\Phi_\mu(E_\mu, E_\nu, \Omega)$  is the flux of muons with energy  $E_\mu$  derived from a parent neutrino with energy  $E_\nu$  from direction  $\Omega$ ;  $\rho$  is the density of rock in  $g/cm^3$ ,  $N_A$  is Avagadro's number,  $\frac{dE}{dx}$  is the muon energy loss per unit length, which is a function of muon energy;  $\Phi_\nu(E_\nu, \Omega)$  is the flux of neutrinos;  $\frac{d\sigma(E_\nu, E_\mu^\circ)}{dE_\mu^\circ}$  is the cross section for a neutrino of energy  $E_\nu$  to undergo a charged current interaction in the rock and produce a muon of energy  $E_\mu^\circ$ . In this scenario, the muon is produced with energy  $E_\mu^\circ$  some distance from the point where the flux is measured, by which time the muon has lost energy to  $E_\mu$ .

The neutrino cross section is computed by integrating the naive parton model cross section for neutrino-nucleon interactions over the parton distribution functions GRV94-LO [61]. The average muon energy loss in rock surrounding the detector is taken from the computation by Lohmann, *et al.* [62] (and recall energy loss fluctuations are ignored).

The generator produces muons at the detector according to the calculated flux. The event record stores the parent neutrino energy, the zenith angle of the parent neutrino with respect to vertical at the detector, the initial muon energy (before energy loss while propagating from the interaction point to the detector), the distance the muon has traveled to reach the detector, and the muon energy at the detector.

### 3.4.3 Tuning the Monte Carlo

Both Geant and GMACRO provide a number of discrete and continuous parameters which must be chosen carefully to provide an accurate simulation without wasting too much computer time calculating irrelevant processes. The parameters used in this analysis are as follows:

```

TRAK 1
HITS 1
DIGI 1
RAWD 1
NSMOD 6
NHMOD 2
MULS 1
LOSS 1
ANNI 1
BREM 1
COMP 1
DRAY 1
PAIR 1

```

```

MUNU 1
RAYL 0
DCAY 1
PFIS 2
PHOT 1
HADR 5
CUTS 10*0.0005
SETS 1='CPLS' 'LPLS' 'FPLS' 'CPLT' 'LPLT' 'FPLT'
SETS 7='HTPT' 'TPT1' 'TPT2'
SETS 10='HTPS' 'TPS1' 'TPS2'
SETS 13='SQTP'
c WNOI 1
c SNOI 1
TIME 0. 0. 0
TRHW 120*6.87
TRHS 1=2.55 3*3.15 2.55 3*3.0 2.55 3.0
      (Same TRHS parameters repeated for all twelve modules)
ELAT 0.85
TRWT 6.5
TRST 2.65
TRLT 9.5
TROT 200.
BACK 'BOTH'
ERPP 1=1 2=10 3=5 4=12 5=07
ERPP 6=0.55 7=0.55 8=1.4 9=.7 11=1
PNRM 2.

```

One would have to read the Geant and GMACRO documentation to know the exact meaning of each card, but some of the more important choices are described here.

All relevant physics processes are turned on except Rayleigh scattering. All types of particles are tracked until they have lost energy and have less than 0.5 MeV remaining (as controlled by the CUTS parameters).

The propagation of low energy neutrons in the detector requires some special attention. GHEISHA [63], the default hadron tracking code in Geant, is only valid down to neutron energies of about 20 MeV. However, this is not really adequate. Even a very low energy neutron may propagate up to a few meters through the rock in the interior of the detector. And if a neutron reaches a scintillator tank, even if its kinetic energy is less than an MeV, it may be captured by a carbon nucleus with the release of several MeV – enough to fire the ERP trigger. Thus, it is necessary to track neutrons below 20 MeV. However, Figure 3.8 shows that GHEISHA gives implausibly long and complex tracks when asked to track neutrons as they lose energy all the way down to 0.5 MeV. To improve the situation, an alternative hadron tracking code purported to track low-energy hadrons more accurately, MICAP [64], was incorporated into Geant and selected by setting the HADR parameter to 5. As seen in the figure, it gives plausible results for the low-energy neutrons.

Measurements made by MACRO are not perfect. The timing and position derived from the high-threshold TDCs do not agree perfectly with the low-threshold TDCs, nor does the position derived from ADCs agree perfectly with position derived from TDCs. Sometimes these problems arise because more than one particle hits the same box, at different places and different times (this is especially likely in contained-vertex neutrino interactions). If only one particle hits the box, GMACRO could give almost perfectly-consistent results in all channels provided that certain non-ideal behaviors were not simulated.

GMACRO models errors in timing as due to two sources – a gaussian error due to details of how the light propagates from its point of generation to the tank end where it is detected, and a gaussian error in the accuracy of time digitization in the ERP. The first error results in both TDCH and TDCL at a given tank end making the same (slightly-incorrect) measurement, while the latter introduces differences between the measurements of TDCH and TDCL. The default value of the gaussian error in the

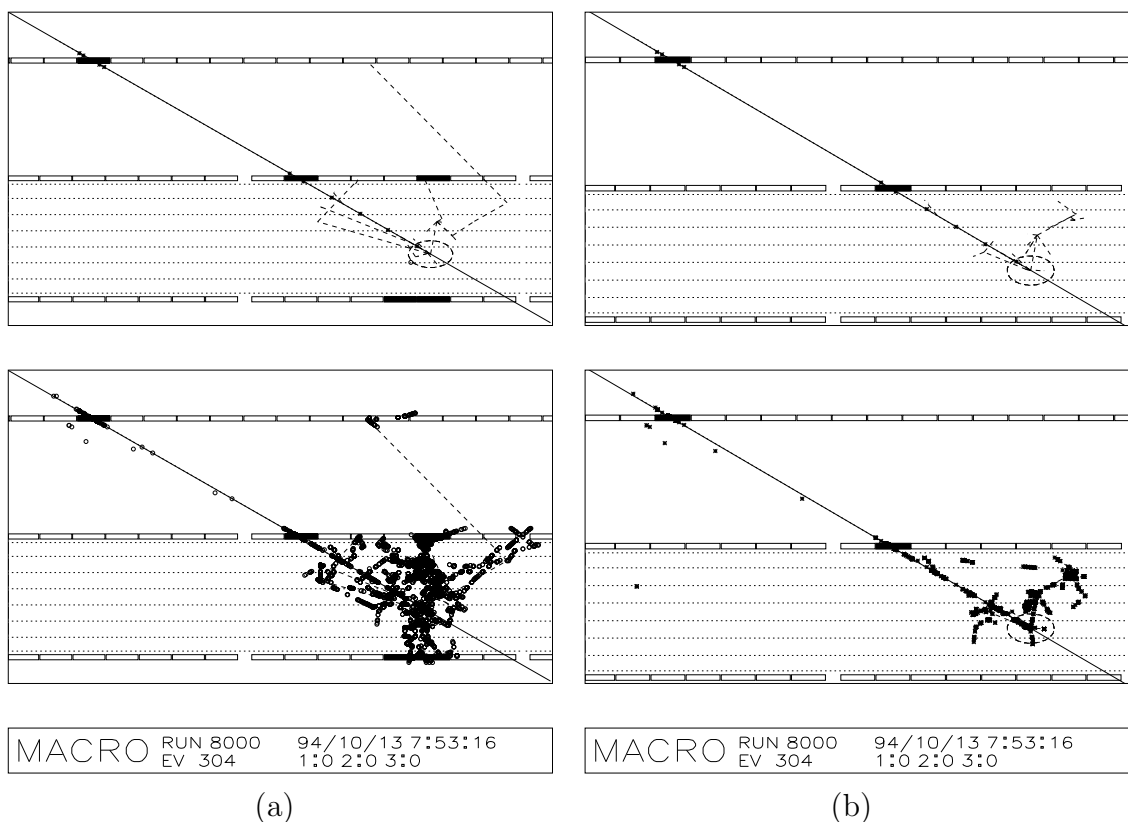


Figure 3.8: Simulation of low energy neutrons. The upper figures show, in addition to MACRO channels that fired, the starting and ending points of secondary particles (dashed lines). The lower figures add indicators of all GMACRO elements through which a particle passed. (a) shows the improper simulation of the GHEISHA hadron code. (b) shows the same event, this time using the MICAP hadron interaction code.

digitization (ERPP 8=0.7 ticks) results in a distribution of  $\text{time}(\text{TDCH}) - \text{time}(\text{TDCL})$  that is too narrow; a value of 1.4 ticks reproduces the data well (see Figure 3.9a). The error for position derived from TDCs is dominated by the uncorrelated variation in time of propagation to the two different tank ends. For real data, our best estimate of where the particle really went through the tank is derived from streamer tube tracks, so ERPP 6 and 7 (for horizontal and vertical tanks respectively) are tuned to match the Monte Carlo and real-data distributions of the distance from a track to a scintillator hit as determined by scintillator timing. The default value of 0.7 ns gives too large a mismeasurement; the value of 0.55 ns fits the data well (see Figure 3.9b).

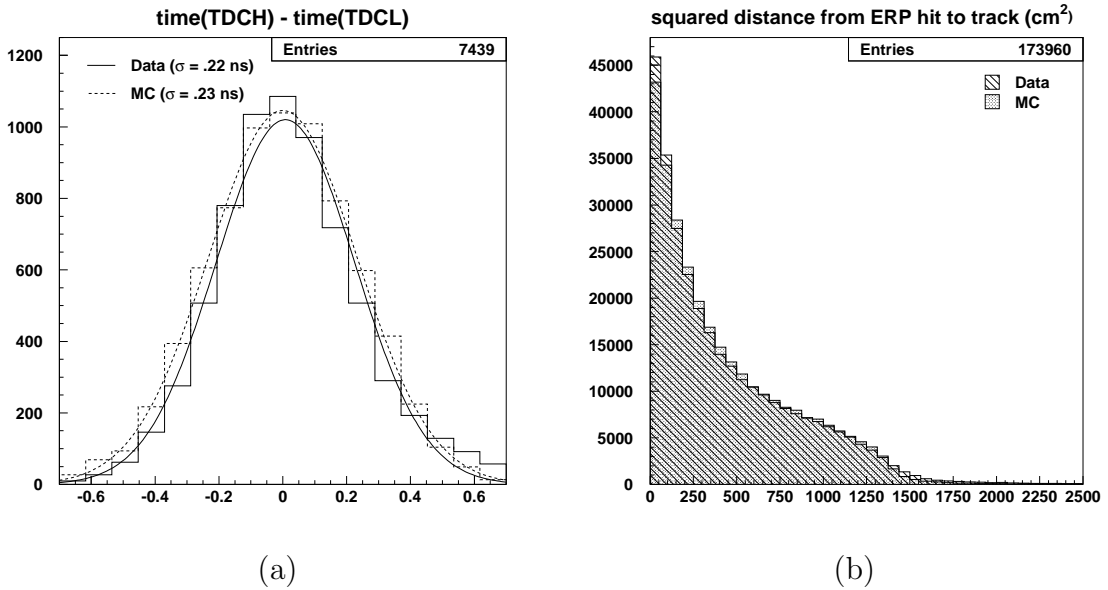


Figure 3.9: (a) Distribution for real and simulated events of the difference between time determined from high-threshold TDCs and time determined from low-threshold TDCs. (b) Distribution for real and simulated events of the square of the distance from the location of a scintillator hit, as determined by scintillator timing, to the associated streamer tube track.

For energy deposition at a given point along the tank, the average number of photoelectrons created at the tank end is proportional (over the energy range of interest) to the energy deposition, where the constant of proportionality is a function of position along the tank (called the response function). To infer the position of an event from ADCs, one searches for a position along the tank where the response function gives the measured ratio of light reaching the two tank ends. The error in this measurement is dominated by fluctuations of photoelectron statistics. For both construction of simulated events and reconstruction of real or simulated data, the product of the response function times the energy deposition is referred to as “photoelectrons.” However, there is ambiguity in the absolute normalization because a multiplicative factor applied to the response function could be compensated by the reciprocal applied to the gain constant. In GMACRO, normally the quantity called photoelectrons is treated as if it were the true number of photoelectrons, and

Poisson fluctuations are taken about that number (ERPP 11=1 turns on the Poisson fluctuations). Comparing GMACRO events to real events, the inaccuracy in position reconstructed from ADC is too great. Therefore, I added code to GMACRO to shift the number of photoelectrons by a constant for purposes of fluctuation; i.e.,

$$P_{GMACRO}(n|\text{mean} = \bar{n}) = P_{Pois}(xn|\text{mean} = x\bar{n})$$

where the value of the normalization factor  $x$  is set by the new control card PNRM. Setting PNRM to 2. gives a reasonable agreement between Monte Carlo and data for the distribution of the difference between position determined by ADC and position determined by TDC (see Figure 3.10).

In real data the collaboration attempted to tune the ERP lookup tables for each box (defined in Section 2.1.2) so that the box had a constant energy threshold for triggering on energy deposition anywhere along the long axis of the box. The threshold was low enough that any muon that passed through a box from top to bottom or side to side would be sure to trigger. However, for corner clippers the particle might or might not trigger depending on the effective trigger threshold. In GMACRO, the energy threshold is perfect so if the energy deposited in the box exceeds the threshold, the box triggers. The threshold is a settable parameter.

In Section 3.3 a procedure to determine the efficiency of each scintillator or streamer tube channel was described. The same procedure can be applied to calculate channel efficiencies for simulated data (although in simulated data there are no dead periods). The Geant/GMACRO parameters used in this analysis are chosen to match the simulated to nominal real efficiencies. For real data, a given type of channel tended to have a nominal efficiency most weeks but on some weeks the efficiency could drop on many or all channels (presumably due to problems with high voltage, readout electronics, or streamer gas). Real data from the week labeled by calibration set 17668 had most channels of all types near nominal, except for strips. The strip efficiencies were quite sensitive to streamer gas composition, and for most weeks a lot of strip channels had efficiencies 10-20% lower than the best channels.

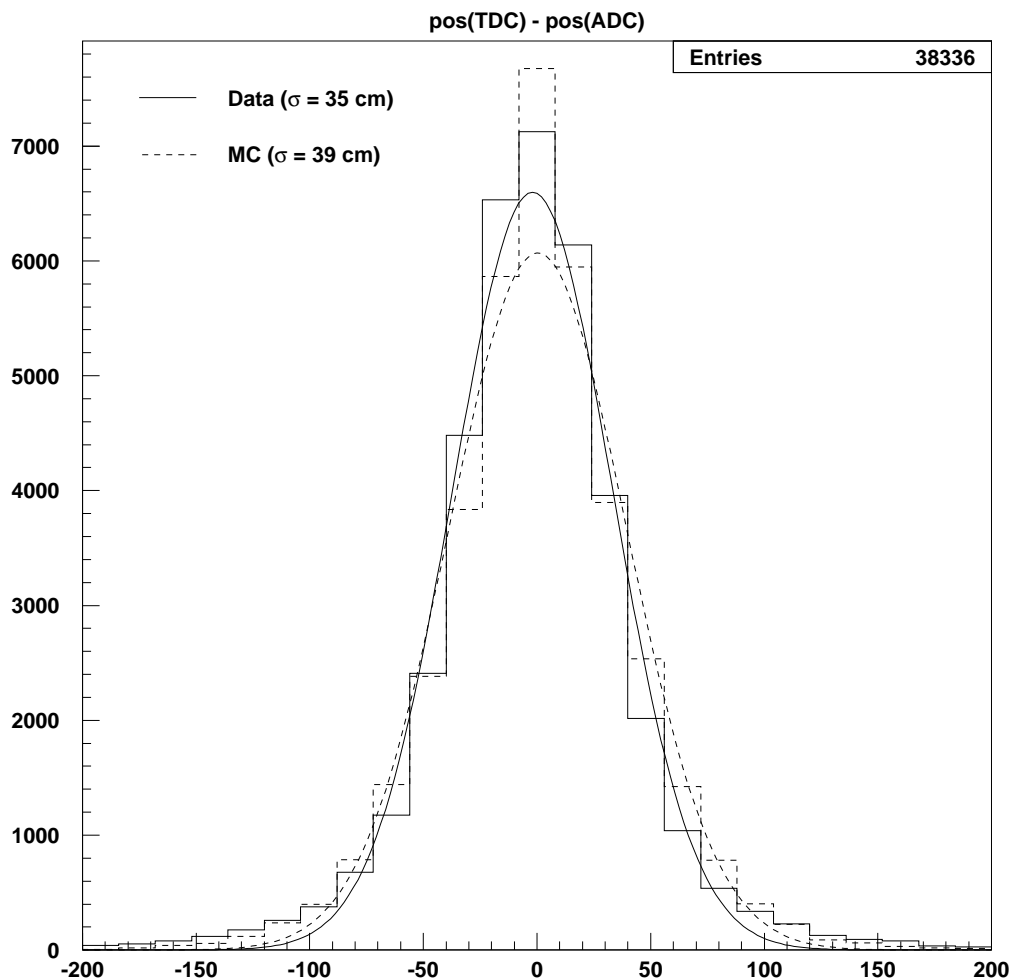


Figure 3.10: Distribution for real and simulated events of the difference between position determined from TDCs and position determined from ADCs.

Calibration set 13936 was one of just a few weeks with a narrower distribution at high efficiencies. So in what follows, set 17668 is used as the real data for comparison with Monte Carlo efficiencies for scintillators and streamer tube wires, and set 13936 is used for strips.

Even in GMACRO, the calculated efficiency is not 100%, nor even exactly the same for all channels of a given type. Inefficiency can occur when particles hit the

box but have a very short pathlength in the box and do not deposit enough energy to trigger; or because of tracking errors due to hard scattering, hits due to secondary particles, or quantization error in the streamer tubes, all of which are simulated. The magnitude of all these effects varies depending on the location of the box. In tuning the Monte Carlo, the goal is to have the distribution of simulated efficiencies match the distribution of measured real efficiencies.

For horizontal boxes of scintillator, the default values of 5 MeV for Elow triggers and 10 MeV for Ehigh triggers (ERPP 2=10 3=5) works well. Figure 3.11 shows good agreement of trigger efficiency for horizontal scintillator boxes in the real and simulated data. In these comparisons, each entry in the histogram is the efficiency for one channel.

For the vertical scintillators, the default trigger thresholds of 5 and 10 MeV for simulated events give measured efficiencies that are too high. There were gaps between scintillation tanks in the vertical layers so slight tracking errors may cause discrepancies, in which a track that appears to hit a box corresponds to a particle that missed the box, or vice versa. It may be that the discrepancy in measured efficiencies is not really due to the trigger thresholds, but due to the probability to have such minor tracking errors. On the other hand, in physics analyses, events that appear to hit the box but really miss it are partially compensated for by events that appear to miss the box by a small amount but really hit it. The latter will be counted as good events in muon analysis, but they will not affect the measured efficiencies. (The efficiency calculation limits itself to events that appear to hit the box, and asks how many of those events caused the box to trigger.) Apparently, minor tracking errors of this type are more likely in real data than in simulated data: for real data, in about 1.3% of events involving a fired vertical box, the track misses the box (in such cases the pathlength is coded as -1 in the histogram in Figure 3.12(b)) while for simulated data the number is just 0.8%. Therefore, the vertical box energy thresholds have been tuned (ERPP 4=12 5=7) to make the measured efficiencies a little high, so the combination of efficiency for tracks that appear to hit the box plus the efficiency for nearby tracks that appear to miss the box are comparable between Monte Carlo

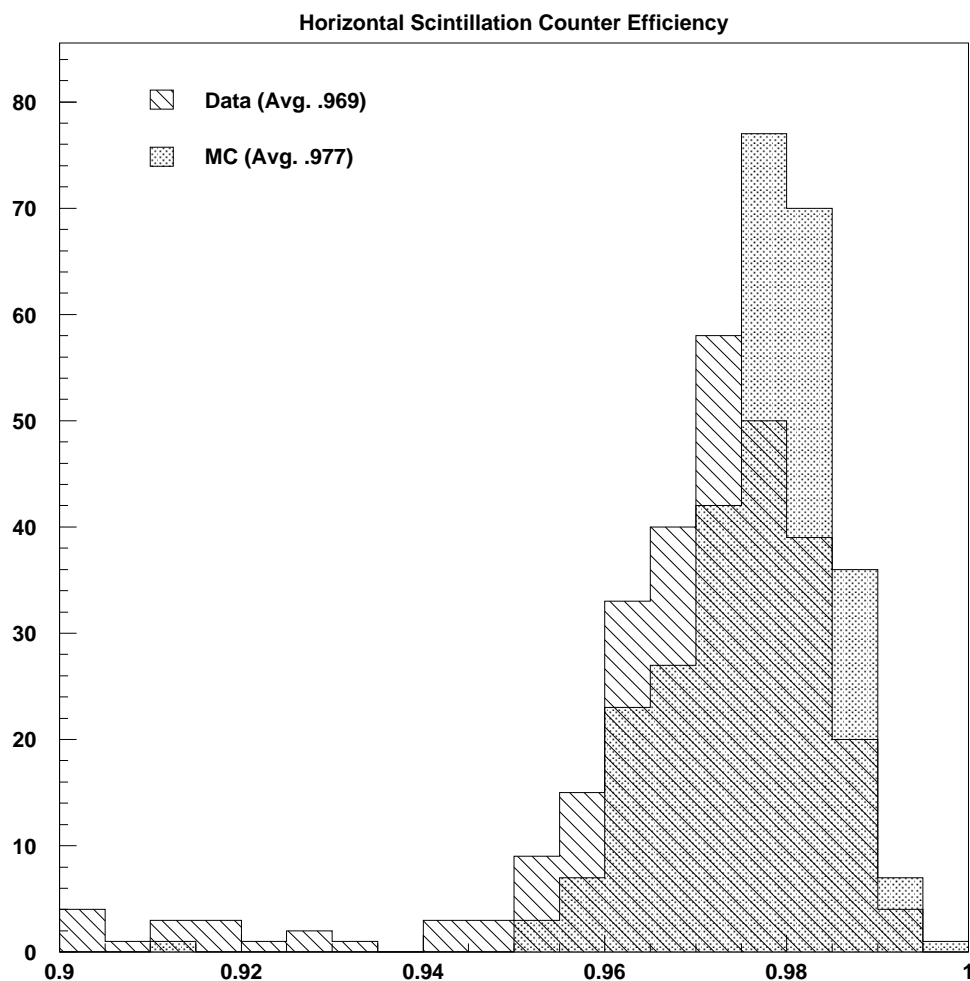


Figure 3.11: Efficiency (as defined in the text) of horizontal scintillators for real and simulated events.

and data.

Each time a particle is tracked through a streamer tube, GMACRO calculates the charge induced on the streamer tube wire, as well as the charge induced on nearby strips. This calculation does not use user-settable parameters. However, the threshold charge above which the Streamer Tube Acquisition System (STAS) considers the channel to have fired is parametrized. Thus, physical inaccuracies in

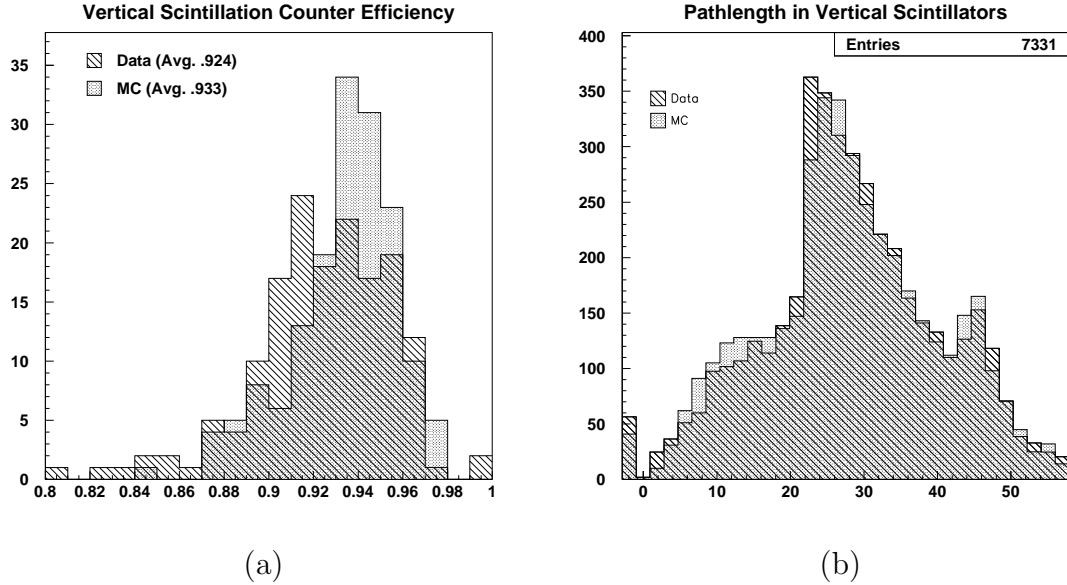


Figure 3.12: (a) Efficiency of vertical scintillation counters for real and simulated events. (b) Distribution of pathlength inside vertical boxes. Events in the artificial bin at -1 appeared to miss the box entirely.

the charge calculation can largely be compensated by choosing the STAS thresholds to reproduce the measured efficiencies and hit width distributions.

For central streamer tube wires, a threshold of  $TRHW=6.87$  (arbitrary units) had been determined some years earlier by MACRO collaborators who tuned the Monte Carlo parameters. Figure 3.13 shows good agreement between simulated and real efficiencies. For the attico planes, there were not any previous efforts to tune the parameter  $TRWT$ . The default value of 7.0 gives low efficiencies, while 6.5 gives good agreement. (Figure 3.13 is summed over lower and attico planes but each alone gives good agreement between Monte Carlo and data.)

The situation is more complicated for central streamer tube strips. Streamer tubes in the first, fifth and ninth streamer tube planes bore a considerable weight (of scintillator tanks or track etch detector) and the plastic tubes deformed, with the result that the strips were  $\sim 1$  mm closer to the wires in these planes than in other planes. Thus, a larger charge tended to be induced on these strips. This effect is not

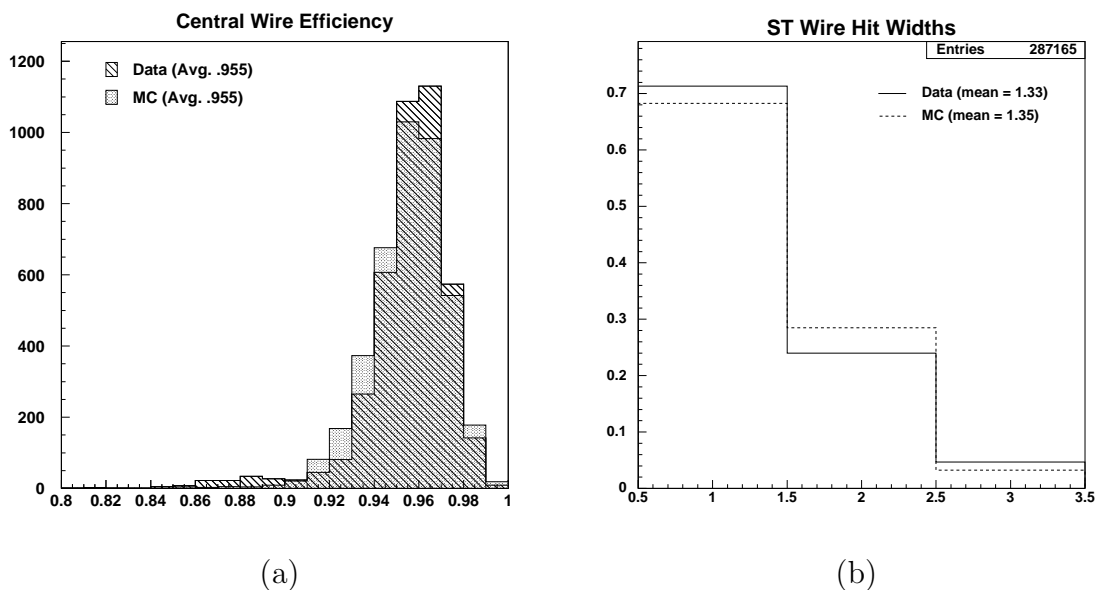


Figure 3.13: (a) Efficiency of central streamer tube wires for real and simulated events. (b) Distribution of number of adjacent wires fired in a plane.

directly simulated in GMACRO. However, one can apply a lower STAS threshold to these planes in GMACRO (using the TRHS parameter) and achieve an equivalent effect – an increase in the probability the STAS considers the channel fired. Again, values that had been determined earlier by MACRO collaborators (specifically, 2.55 for planes 1, 5, and 9; 3.15 for planes 2-4; and 3.0 for planes 6-8 and 10) give a good match between data and Monte Carlo. For attico horizontal strips, the default value of TRST=3.8 works well. (Figure 3.14.)

For the lateral and frontal planes of streamer tube wires in the lower detector, the default parameters result in measured efficiencies greater than in real data. Perhaps this is not really due to an inaccurate simulation of streamer tube efficiencies, but rather reflects a greater accuracy of reconstructed tracking parameters in simulated events. Thus, if (in a real event) the reconstructed track points into a lateral streamer tube channel, the real particle may have missed that channel. However, in the simulated data the probability of such a misreconstruction is lower. The only parameter available to tune the lower lateral streamer tube efficiencies is “ELAT.”

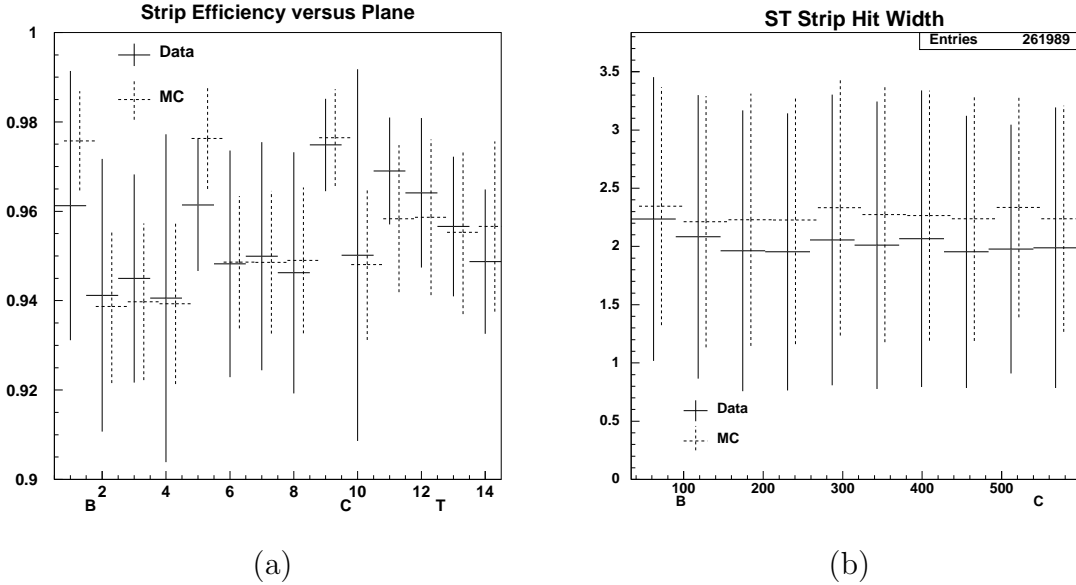


Figure 3.14: (a) Efficiency of central streamer tube strips for real and simulated events, plotted separately for each plane. The datapoints give the mean and RMS of the efficiencies for all channels in that plane. Note the elevated efficiency in planes 1, 5 and 9. (b) Number of adjacent strips fired in a plane of central streamer tube strips. In both figures, the statistical uncertainty on the mean is a tiny fraction of the RMS, and the vertical separation between data and Monte Carlo is statistically significant. The horizontal separation is artificial, for clarity of presentation.

Setting ELAT to 0.85 means that any time the tracking software thinks a lateral streamer tube should fire, it is only put in the acquisition as having fired 85% of the time. However, atmospheric muons typically strike two adjacent cells when passing through most lateral planes, and our definition of efficiency considers the hit efficient if *either* of the cells fire. Thus, it would be necessary to reduce ELAT to ridiculously low values to cause the measured efficiencies of simulated events to change significantly. The lowest value of ELAT I was comfortable with, 0.85, results in measured efficiencies of simulated events still a percent or two too high. For the attico, the standard GMACRO code does not provide a parameter to vary the efficiency of the attico lateral planes independently of the lower planes. However, it was not possible to set the parameter to match the efficiencies of both kinds of streamer tubes. There-

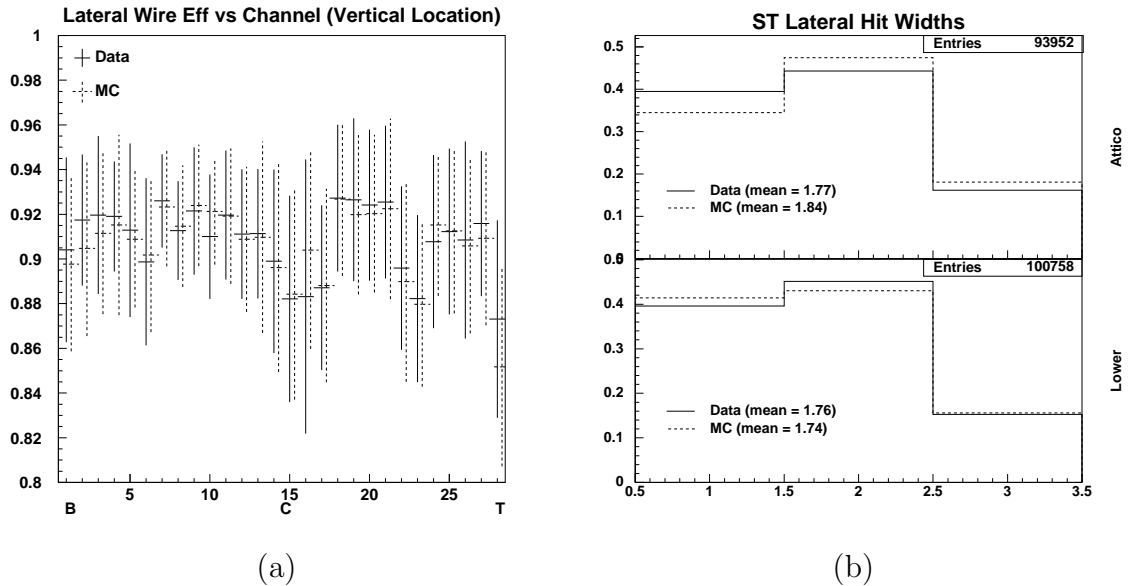


Figure 3.15: (a) Efficiency of lateral streamer tube wires for real and simulated events. (b) Hit width distribution. The upper figure is for attico, and the lower for the lower part of the detector.

fore, I coded a new threshold parameter, `TRLT`, into `GMACRO` to control the attico lateral planes separately from the lower detector. Setting `TRLT` to 9.5 gives a good match of the efficiencies. (Figure 3.15.)

Lateral strips are not used in this analysis, so their performance has not been tuned.

### 3.4.4 Simulating Problems with the Real Hardware

With the nominal Monte Carlo, we can make predictions of what would have been observed if the detector operation had always been nominal. However, during the data-taking there were a number of hardware problems that degraded the detector performance, some minor (for example an ERP channel that must be excluded from offline analysis because it gives unreliable timing for a week or two) and some major (for example an entire supermodule that was excluded from the acquisition for a few days because of a bad high voltage power supply). To draw conclusions about the

neutrino flux based on the observed rate of neutrino interactions, the effect of the observed hardware irregularities must be estimated.

For MACRO high energy neutrino analyses, in which the neutrino-induced muon traverses the entire detector, the topology of neutrino events is similar enough to the topology of the copious downgoing atmospheric muons that we may use a clever technique called *equivalent livetime*. In this approach, for a period of running when the detector is known to have been operating well in all channels, the rate of downgoing muons is calculated. Then for the entire dataset, the equivalent livetime is defined as the total number of downgoing muons observed divided by the nominal rate. The idea is that if there were a period of time, say 100 hours, during which detector problems were severe enough to cause the loss of 5% of the downgoing muons (so the rate during that period was 95% of the nominal rate), that would be equivalent to having run for 95 hours at nominal efficiency.

Around 800 downgoing muons stop in the detector each week, giving a topology similar to the semi-contained upgoing neutrino interactions with which this analysis is concerned. We might hope to define an equivalent livetime procedure using the rate of downward stopping muons to monitor detector efficiency. However, on reflection we must abandon this approach. First of all, detector problems could cause the rate to go either up or down. For example, widespread detector problems could cause events to be not detected at all and reduce the measured rate. On the other hand, streamer tube inefficiency could cause an event that really had throughgoing topology to appear as if it were semi-contained. Thus, the more numerous throughgoing events could bleed over and infect the apparent semi-contained rate. Because the ratio of downward throughgoing muons to downward stopping muons (about 100:1) is much greater than the ratio of (neutrino-induced) upward throughgoing muons to upward semi-contained events (about 10:1), measuring an increased rate of apparent stopping muons does not give a good estimate of the expected increase in the rate of apparent semi-contained neutrino events. Furthermore, the distribution of which streamer tube planes are most important is different for downgoing stopping muons than for semi-contained neutrino events. For these reasons, the equivalent livetime approach can

give only a rough idea of the effect of hardware problems but cannot give a good quantitative estimate.

Therefore, instead of relying on the equivalent livetime approach, the detailed measurement of dead periods and inefficiencies in the real data (described in Section 3.3) are applied to the simulated data. For each week of real data-taking, a database has been created listing for each channel the dead periods, as well as the efficiency during the non-dead periods. To simulate the detector during a given week, first, events are generated using the nominal Monte Carlo. Then, for each event, a time during the week is picked at random and the event record is altered by removing channels that were dead and probabilistically removing channels that were inefficient at the chosen time. After channels are eliminated, then the event is analyzed. If any microcuts are in effect for that week, they are applied by the analysis software.

### **How Well Does It Work?**

Starting with a Monte Carlo sample of 100,000 downgoing atmospheric muons that reach the detector, if no detector irregularities are simulated, 63,340 muons pass all cuts of the muon analysis. Then a series of jobs analyze all 100,000 input events while simulating conditions (dead periods, inefficiency, and microcuts for each channel) of each analysis week (one job for each week). About 1/3 of the weeks give more than 60,000 reconstructed muons; the greatest is 61,759. Thus, even during the very best weeks, the simulation indicates that non-ideal performance of the detector (most significantly the computer deadtime) caused about a 2.5% reduction in efficiency, from 63,340 events detected to 61,759.

Also for each week, the number of real events that reconstructed as good muons, divided by the number of minutes of data-taking that week, yields a rate. Half the weeks show a rate between 10.5 and 11.3 muons per minute. If one or more supermodules was turned off for long periods during the week, the rate is much lower. With about 100,000 real muons reconstructed each week, the statistical error on the measured rate is around 0.3%.

The atmospheric muon generator in GMACRO has no concept of time or rate; it

produces a flux with the proper angular and energy distributions, but does not say anything about the predicted rate. The Monte Carlo prediction may be normalized using the weeks in which the effect of detector problems was least; that is, the weeks in which the measured rate was greatest. In a scatter plot of number of simulated muons passing all cuts versus rate in the real data (Figure 3.16), the 5 weeks with the highest real rates (all within 0.6% of each other) (the weeks were 15647, 16017, 16049, 16080, and 16184) also have some of the highest numbers of simulated muons (all within 0.5% of each other). The average of the rates (11.19) and the average of the number of simulated muons (61,679) for these 5 weeks is used to determine the livetime of the Monte Carlo sample as  $\frac{61,679 \mu}{11.19 \mu/min} = 5510$  min. With this assumption, the number of simulated muons reconstructed for each week can be used to predict the real data rate for that week. This choice of how to normalize the Monte Carlo is obviously quite arbitrary; if instead of using the 5 weeks with highest rate, we chose a different number of weeks between 1 and 9, the calculated livetime of the simulation would differ by no more than 0.2% from the original choice.

The simulation predicts the measured rates fairly well (Figure 3.17). Most weeks have rates near the nominal  $\sim 11$ /min, and the simulation predicts that. Some weeks have significant irregularities (for example, two supermodules may have been turned off during the entire week), and the simulation does a good job of predicting the rate during those weeks as well. The error (predicted rate minus measured rate) appears like a random variable with variance (according to a gaussian fit to the error histogram) of 2%. Actually, this error is too large to be accounted for by counting statistics in the number of muons. Apparently the simulation algorithm, which is not exact, sometimes overestimates and sometimes underestimates the effect of irregularities but does so in a random way. Summing over all 262 analysis weeks, the errors tend to cancel. In fact, if we multiply the predicted rate for each week times the real livetime for that week, the simulation predicts the total number of muons in the entire dataset to within 0.3% (23,790,000 predicted versus 23,726,256 observed).

Another way to frame the same problem is to ask the simulation to predict the inefficiency in any given week due to detector irregularities. (Here the term inefficiency

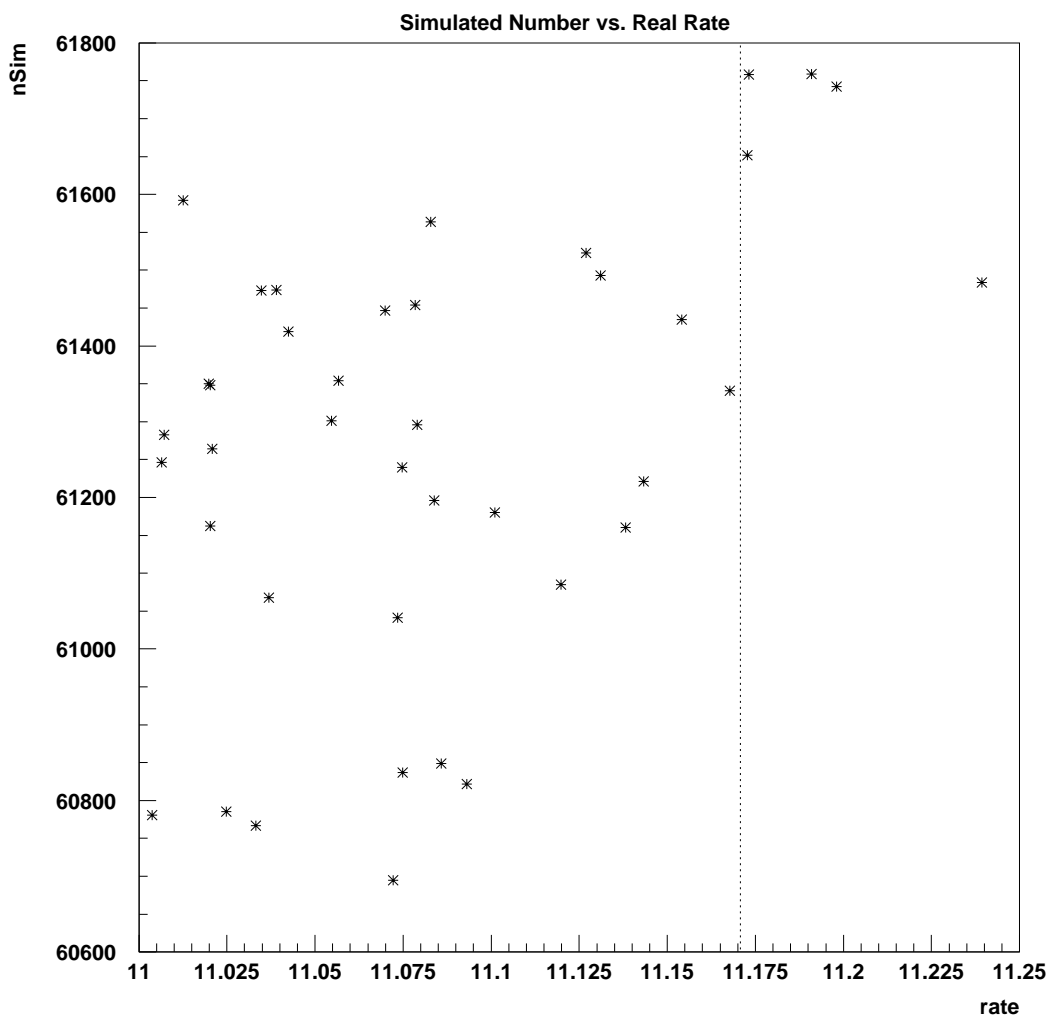


Figure 3.16: Weeks with the highest measured rates. Each point represents one week; the measured muon rate in real data is on the x-axis while the y-axis gives the number of simulated muons that reconstruct when the conditions for that week are simulated. The five weeks in the upper right are averaged to set the normalization of the Monte Carlo.

is used very loosely, to refer to the difference between the muon rate for the week and the nominal rate of 11.19.) Figure 3.18 shows the results, which again are fairly good.

Summed over all weeks, the simulation predicts there would have been 26,970,000

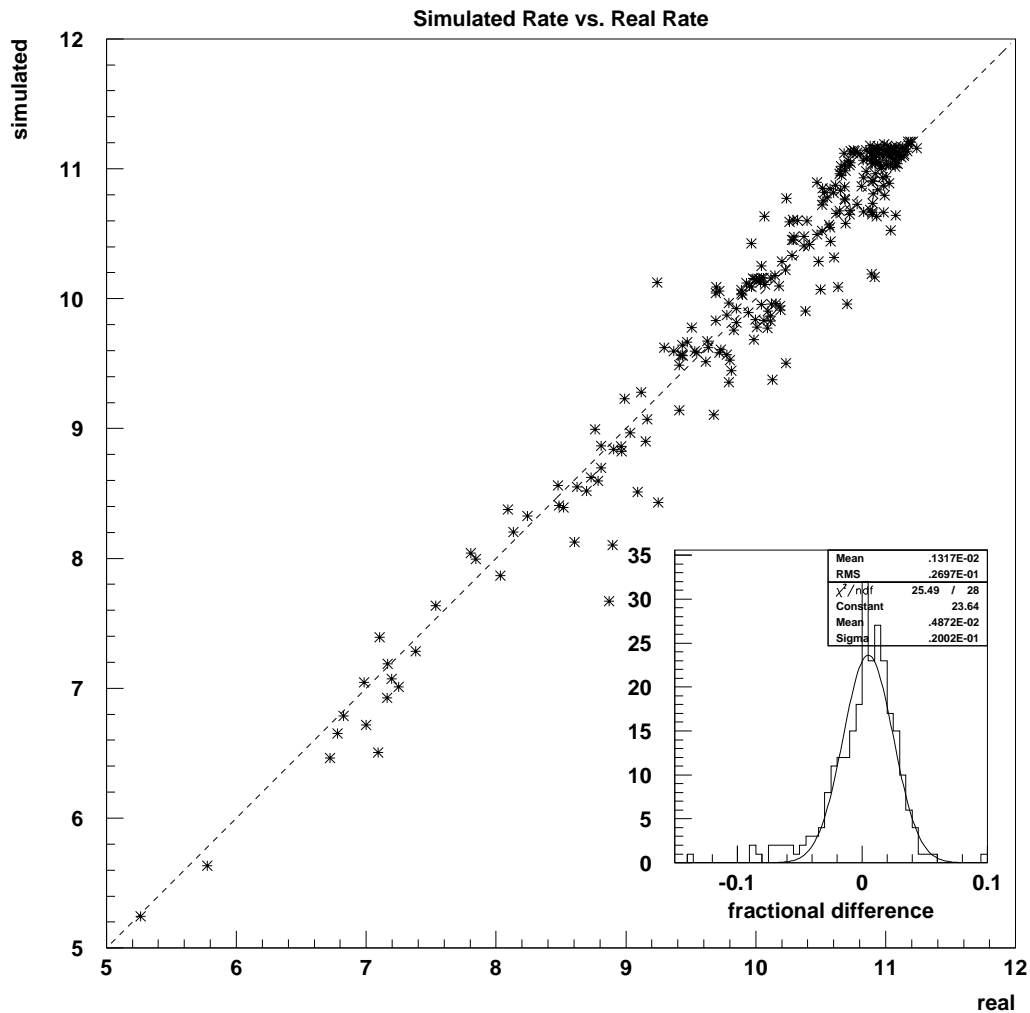


Figure 3.17: Comparison of predicted rate (y-axis) to measured rate for atmospheric muons (mostly throughgoing). Each point represents one week. The dashed line at 45° is not a fit, but shows the ideal locus, predicted = measured. The inset shows the distribution of fractional differences, (predicted - measured)/measured.

muons if there had been no hardware problems (assuming the normalization of the simulation livetime above is correct). The prediction is reduced by 11.8% taking hardware problems into account, while the observed number is 12.0% less than the no-problem prediction. As before, all the week-by-week errors canceled and the prediction of inefficiency summed over all weeks is accurate.

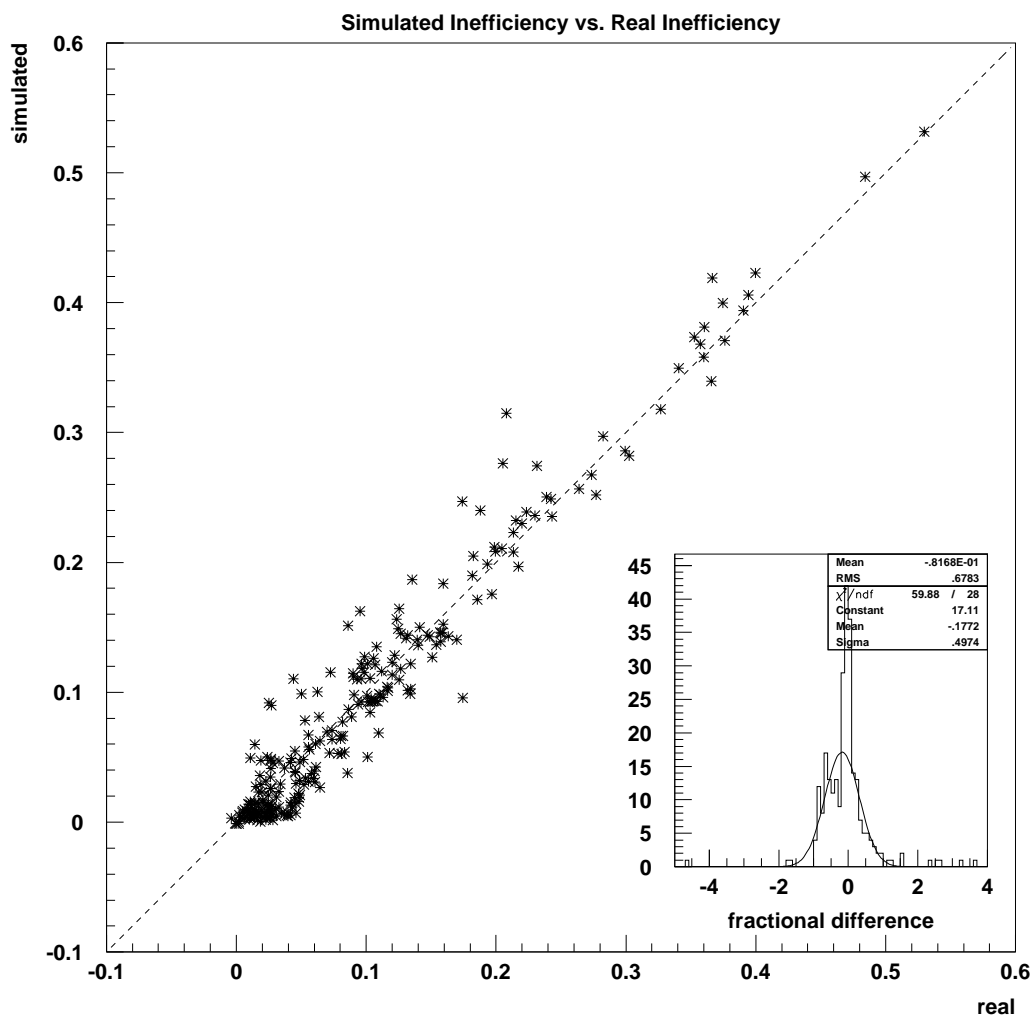


Figure 3.18: Comparison of predicted inefficiency (y-axis) to measured inefficiency.

The task of predicting the efficiency for throughgoing muons is easier than the task of predicting the efficiency for the semi-contained events with which this thesis is concerned. In Chapter 5, criteria will be defined for muons that appear to either originate (upgoing) or stop (downgoing) in the detector. Compared to throughgoing muons, the rate of such muons is more sensitive to exactly how many channels have problems when and where. Less than one upgoing neutrino-induced event of this topology occurred per week; however, between 600 and 1000 downward stopping at-

mospheric muons were recorded most weeks. If the simulation can accurately predict the rate of stopping muons week by week, that would give us some confidence that the efficiency it predicts for the neutrino analysis is reliable.

Of the 100,000 simulated downgoing muons (the same sample used above), 527 are identified as stopping muons when hardware problems are not simulated. Simulating hardware problems, half the weeks show 480 or more simulated stopping muons. As discussed in Section 3.4.2, the simulation does not get the muon spectrum underground exactly right, and underpredicts the rate of stopping muons by 5.0%. We could use the above calculation, that the livetime of the simulation is 5510 min, and convert the number of stopping simulated muons to a prediction of the real rate of stopping muons. However, that would just recover the fact that the overall normalization of the stopping fraction is off by 5.0%. Instead, let us re-normalize the simulation to get a simulation livetime for stopping muons.

Using the same weeks identified above that have high rates of throughgoing muons (ostensibly, these are the weeks that had the least significant hardware problems), the measured rates average to 0.0966 stopping muons per minute, and all 5 weeks are within 4% of this average. (The error due to counting statistics is greater when considering the stopping muon problem, on the order of 3.5% (800 events) for the real data and 4.5% (500 events) for the simulated data.) The number of simulated stopping muons averages to 514.6, and all 5 weeks are within 2.6% of this average. That suggests a simulated livetime of 5326 minutes. (Using a different number of weeks between 1 and 9 to set the normalization yields a livetime differing by no more than 1% from the original choice.) Using this equivalent livetime, summing over all 262 weeks the simulation predicts there would have been 227,800 stopping muons if there were no hardware problems, or 204,700 taking the hardware problems into account. The measured number is 207,831. The predicted total is off by about 1.5%. To put the same result another way, the predicted inefficiency due to hardware problems is 10.1% while the measurement (difference between number of muons expected if all weeks had nominal performance and the number of muons actually observed) is 8.8%.

In conclusion, over the course of the run, the procedure for estimating the effect

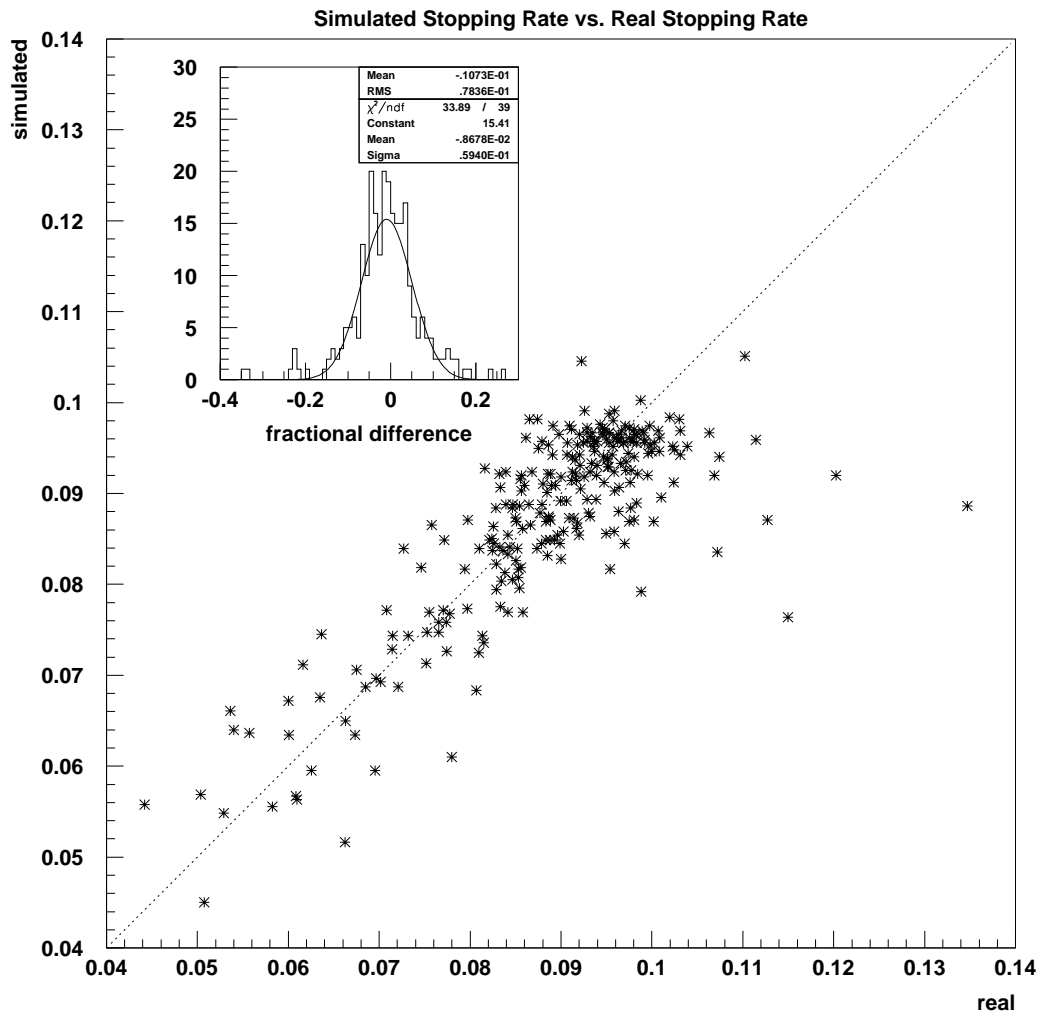


Figure 3.19: Comparison of predicted rate of stopping muons (y-axis) to measured rate.

of hardware problems appears to be accurate to around 1.5% for a set of events quite similar to the neutrino-induced muons with which this thesis is concerned.

## Chapter 4 Predicting the Atmospheric Neutrino Interaction Rate

To search for evidence of neutrino oscillations, we must have a good understanding of the expected event rate in the absence of oscillations, and how it changes as a function of the oscillation parameters. For the experimental signatures considered in this analysis, the neutrino energies must be hundreds of MeV or higher (i.e., above  $\nu_\mu$  charged current threshold). In this regime, almost all neutrinos are atmospheric neutrinos, i.e., neutrinos from hadronic showers that develop when high energy cosmic rays hit the atmosphere. One can use knowledge of the primary cosmic ray flux and hadronic interaction models to make predictions about the flux of atmospheric neutrinos. The flux may be folded with a charged current cross section as the basis of event rate calculations.

This chapter is organized as follows: The first section is about calculating the neutrino flux. It starts with some general principles, then explains some of the subtleties involved in making accurate calculations. The Bartol flux, a calculation used to make predictions in this analysis, is discussed in a little more detail. The second section is about the neutrino cross section. First, a number of calculational approaches are described. Then two particular calculations are detailed: the Lipari model, upon which predictions in this analysis are based, and NEUGEN, an alternative cross section calculation that has been used as an independent check on the predictions.

### 4.1 Atmospheric Neutrino Flux

When primary cosmic ray particles (typically protons) reach the atmosphere of earth, hadronic interactions will occur (the atmosphere is about eight nuclear interaction lengths). Atmospheric neutrinos typically descend from mesons (pions or kaons) in

the hadronic shower, through one of the processes

$$\begin{array}{ll}
 p + X \rightarrow \pi^+ X & p + X \rightarrow \pi^- X \\
 \hookrightarrow \mu^+ \nu_\mu & \hookrightarrow \mu^- \bar{\nu}_\mu \\
 \hookrightarrow e^+ \bar{\nu}_\mu \nu_e & \hookrightarrow e^- \nu_\mu \bar{\nu}_e
 \end{array}$$

where the charged  $\pi$  may be replaced with a charged K, which decays to  $\mu$  about 70% of the time, or a  $K_L^0$ , which decays leptonically 66% of the time.

To first order, a flux calculation requires only a knowledge of the flux of primary cosmic rays as a function of energy, the density profile of the atmosphere, and a model of hadronic interactions (as well as leptonic interactions, which are well-known). However, if more precision is desired, a number of subtleties must be considered.

Flux calculations have passed through several generations. The first calculations were made in the early 1960s, within the first decade after reactor neutrinos had been detected; and the first observations of atmospheric neutrinos were reported in 1965 [65, 66]. A revival of calculations occurred in the 1980s as atmospheric neutrino interactions constituted a background in searches for nucleon decay deep underground. When some observations showed a discrepancy from the predicted ratio of  $\nu_e$  to  $\nu_\mu$ , attention turned to the possibility of neutrino oscillations. Experimenters demanded greater precision, and progress was made steadily from 1987 until about 1996. The flux calculation used in this analysis dates from 1996. The definitive observation of oscillations by Super-Kamiokande in 1998 reinvigorated the field. Since then, many technical improvements have been demonstrated; unfortunately at this time no complete calculation has been performed taking the new findings into account. The computational intensity of the calculations is scaling along with the computational resources of the authors.

### 4.1.1 Transport Equations

The simplest models are analytic (or semi-analytic) solutions of *transport equations*. This approach does not simulate individual interactions but rather treats the flux of a particular particle species as a time-independent field which evolves as a function

of energy and depth in the atmosphere. The transport equation approach dates back at least to the 1941 work of Rossi and Greisen on electromagnetic cascades in the atmosphere [67], and has been successfully extended to consider all the particles discovered in cosmic ray cascades since then. To be tractable, the equations must ignore any transverse momentum imparted to secondary particles; the showers are taken to evolve collinearly with the primary particle's momentum.

If we ignore the production of nucleons by non-nucleonic secondary hadrons, and ignore continuous ionization loss, the transport equation for nucleons is then

$$\frac{d\Phi_N(E, X)}{dX} = -\frac{\Phi_N(E, X)}{\lambda_N(E)} + \int_E^\infty dE' \frac{\Phi_N(E', X)}{\lambda_N(E')} \frac{F_{NN}(E, E')}{E}$$

Here  $\Phi_N(E, X)$  is the flux, differential in  $E$ , of nucleons that have traversed a distance  $X$  (measured in  $\text{g}/\text{cm}^2$ ) through the atmosphere. On the right-hand side of the equal sign, the first term is a sink in which nucleons of energy  $E$  interact and go to a lower energy (possibly producing mesons at the same time), while the second term is a source in which nucleons of higher energy  $E'$  interact to produce nucleons of energy  $E$  (and possibly some mesons).  $\lambda_N(E)$  is the *interaction length* of nucleons in air, so that the differential probability of a hard interaction while traversing  $dX$  is  $dX/\lambda_N$ . At typical cosmic ray energies (1 TeV),  $\lambda_N$  is about  $80 \text{ g}/\text{cm}^2$ .  $F_{NN}(E, E')$  is a dimensionless quantity, defined such that  $1/E F_{NN}(E, E')dE$  gives the probability that, when a nucleon of energy  $E'$  undergoes a hard scattering process, a nucleon of energy  $E$  results.

For unstable hadronic secondaries ( $\pi, K$ ),

$$\frac{d\Phi_{i=\pi, K}(E_i, X)}{dX} = -\left(\frac{1}{\lambda_i} + \frac{1}{d_i}\right) \Phi_i(E_i, X) + \sum_j \int dE_j \frac{\Phi_j(E_j, X)}{\lambda_j} \frac{F_{ji}(E_i, E_j)}{E_i}$$

where  $i$  and  $j$  indicate particle species, which in the source term includes nucleons. The  $d_i$  term is a sink due to particle decay. The decay length must be given in units of matter traversed (i.e.,  $\text{g}/\text{cm}^2$ ); therefore, one must adjust the naive decay length to account for the density of air at that point, as well as the Lorentz dilation of the

particle lifetime. One finds that

$$d_i = \rho \gamma \tau_i$$

where  $\rho$  is the local density of air,  $\gamma$  is the Lorentz factor and  $\tau_i$  is the proper lifetime of the particle.  $\rho$  depends on the altitude rather than the slant depth, so the angular dependence enters explicitly. The atmospheric profile is to a good approximation exponential, and we can derive

$$d_i = \frac{E \tau_i X \cos \theta_{zen}}{m_i h_0} = \frac{E}{\epsilon_i} X \cos \theta_{zen}$$

where  $h_0$  is the scale height of the exponential density profile, a few kilometers, and the definition of  $\epsilon_i$  is obvious. A long-lived particle has small  $\epsilon$ . Numerically,  $\epsilon_{K^\pm} = 850$  GeV,  $\epsilon_{\pi^\pm} = 115$  GeV, and  $\epsilon_{\mu^\pm} = 1$  GeV. For energies much greater than  $\epsilon$ , the particle will probably interact or range out before it decays. For energies much less than  $\epsilon$ , the particle will probably decay before interacting.

Muons arise from the decay of pions rather than from interacting hadrons, and we write (neglecting muon interaction and ionization loss),

$$\frac{d\Phi_\mu(E_\mu, X)}{dX} = -\frac{\Phi_\mu(E_\mu, X)}{d_i} + \int dE_\pi \frac{\Phi_\pi(E_\pi, X) \epsilon_\pi}{E_\pi X \cos \theta_{zen}} \frac{F_{\pi\mu}(E_\mu, E_\pi)}{E_\mu}$$

where the source term is based on  $(\frac{d\Phi_\pi}{dX})_{decay}$ . For electrons and neutrinos, similar transport equations apply. The  $e$  and  $\nu_e$  equations have no interaction or decay term, and a source term due to muon decay. The  $\nu_\mu$  equation has no interaction or decay term, and source terms due to both pion decay and muon decay.

The neutrino probabilities in the muon decay term  $F_{\mu\nu}$  must not be calculated by averaging over angle in the muon's rest frame. The muon is produced by a weak interaction fully polarized in the pion rest frame, and after boosting back into the lab frame the muons retain some net polarization along the direction of flight. If the muon decays, it tends to throw the electron neutrino forward and the muon neutrino

backward, increasing the  $\nu_e/\nu_\mu$  ratio at a given energy.

The various transport equations are coupled, and can in principle be solved, given the initial conditions that  $\Phi_N(E, 0)$  is the input primary spectrum and  $\Phi_i(E, 0)$  is zero for all other species. In practice, analytic solutions can be found if the input spectrum is a power law in  $E$ ,  $\Phi_N(E, 0) = E^{-\gamma}$  (approximately true), and if the cross sections are assumed to scale, so that

$$\lambda_i(E_i) = \lambda_i$$

$$F_{ji}(E_i, E_j) = F_{ji}\left(\frac{E_i}{E_j}, 1\right)$$

independent of energy (also approximately true over most of the relevant energy range).

Gaisser [59] gives some exact and some approximate results from solving the transport equations with a certain model for the hadronic interactions. Qualitatively, for nucleons the shape of the power law spectrum remains unchanged while the magnitude of the flux attenuates exponentially through the atmosphere with attenuation length  $120 \text{ g/cm}^2$  (the vertical column of the atmosphere is about  $1 \text{ Atm}/g_{grav} \approx 1000 \text{ g/cm}^2$ ). The attenuation length is greater than the interaction length for nucleons because it includes the effect of regeneration due to scattering of higher-energy nucleons. Pions and kaons have the same energy spectrum as nucleons. Their fluxes initially rise as they are produced by plentiful nucleons, peaking around  $100 \sim 200 \text{ g/cm}^2$ ; but after the nucleon source attenuates, the meson sink due to decay or interaction becomes more important and the meson fluxes attenuate, eventually exponentially. The lepton fluxes are quite energy-dependent, as they depend on the relative sizes of the meson interaction and decay terms. The probability of a high-energy pion decaying before it interacts goes as  $1/E$ , so at high energy the muon flux goes as  $E^{-\gamma-1}$ . At lower energy all the pions decay and the muons, like the hadrons, go as  $E^{-\gamma}$ . For muons of low enough energy that they cannot reach the earth, the daughter neutrinos follow the energy dependence of the muons. At low energy the

fraction of muons from kaon parents is 8%, increasing to 27% asymptotically (well above 1 TeV). This is because kaons are so short-lived; at higher energies for which the pion usually interacts the kaon continues to decay. Due solely to kinematics, the fraction of muon neutrinos due to kaons is greater than the fraction of muons due to kaons, and becomes greater than 50% around 85 GeV [68].

For high energy muons and neutrinos there is an explicit zenith angle dependence, making horizontal leptons more numerous than vertical. This arises from the meson decay term. For a pion produced from a nucleon at fixed  $X$ , a slanting track will be higher in the atmosphere than a vertical track, and the less-dense atmosphere reduces the interaction term relative to the decay term, making muon production more likely. For an exponential atmosphere, and approximating the atmosphere as flat rather than curved above the detector, the resulting dependence is exactly  $1/\cos\theta_{zen}$ . This approximation works well for zenith angles up to  $60^\circ$ , and is borne out by measurements of atmospheric muons deep underground. For more horizontal leptons the formula must be altered, but it remains true that the flux increases monotonically with zenith angle.

At high energy, another zenith angle dependence enters implicitly. A 2.5 GeV muon has  $\gamma c\tau = 17$  km and many will reach the earth and be stopped before they decay to give high-energy neutrinos. For a given zenith angle, the neutrino flux underground is that calculated at the value of  $X$  corresponding to the surface of the earth. For slanted tracks,  $X$  at the surface is greater (the tracks have seen more  $\text{g}/\text{cm}^2$  of atmosphere), the muons have had more chance to decay, and the neutrino flux is increased. This effect also goes as  $1/\cos\theta_{zen}$  near vertical, and increases the horizontal flux. For the lowest energy showers, all the pions decay and all the muons decay so neither of these effects is operative, and the neutrino flux is isotropic.

Above 1 GeV in the lab, the cross section for neutrino interactions on nucleons is around  $10^{-38} \text{ cm}^2 * \frac{E}{1\text{GeV}}$ , and a trip through the earth encounters on the order of  $10^9 \text{ g}/\text{cm}^2$ , or  $10^{33} \frac{\text{nucleons}}{\text{cm}^2}$ . So for neutrino energies less than a TeV the neutrino beam is essentially unattenuated, while the probability of interaction in the earth is of order unity for neutrinos above 100 TeV. Under the approximations used in this transport

equation approach, the flux is up-down symmetric below a TeV, because a detector sees an identical column of atmosphere at  $\theta_{zen}$  and  $(\pi - \theta_{zen})$ . These assumptions also yield an azimuthally-symmetric flux. The most likely primary energy to have produced a neutrino of energy  $E_\nu$  is around  $10 E_\nu$ .

### 4.1.2 More Precise Calculations

The simple transport equations above give a good qualitative understanding of the neutrino flux underground; however, they are inadequate for quantitative work because a number of important effects have been neglected entirely, and others approximated. Some clever people have made heroic efforts to incorporate many effects into the semi-analytic calculation through *ad hoc* mechanisms; but the most reliable calculations resort to Monte Carlo techniques that simulate individual showers and/or individual trajectories. Monte Carlo programs can easily incorporate effects that were ignored in the semi-analytic calculations, such as muon ionization loss and non-scaling cross sections.

Modern experiments have based their analyses on either of two Monte Carlo calculations: Super-Kamiokande uses the 1995 work of Honda *et al.* [69], referred to as HKKM, while Soudan-2 and MACRO (including this analysis) refer to the Bartol group's high-energy [70] and low-energy [71] calculations of 1995 and 1996, collectively referred to as Bartol. Both HKKM and Bartol are "one-dimensional" calculations which ignore transverse momentum of secondaries. The most interesting new calculation to appear on the scene since 1996 is that of Battistoni *et al.* [72] which includes a new hadronic interaction code (FLUKA) as well as adding in some of the three-dimensional effects ignored by the other two calculations. However, this calculation is still under development and is not yet ready to be used as the main prediction for serious experimental analyses.

Discussion follows on several points that must be considered by the authors of calculations. Generally, the choices made by HKKM and Bartol will be indicated. Afterward, the Bartol calculation (which is used to make predictions for this analysis)

is summarized.

### **Primary Cosmic Ray Flux**

At the time Bartol and HKKM were written there was controversy about the overall normalization of the primary flux above 3 GeV, with the measurement of Weber 79 [73] more than 50% higher than Leap 87 [74] around 10 GeV and above. HKKM based its calculation on a flux that split the difference, while Bartol used a flux just a few percent above the Leap 87 result. In the 1990s, a number of new measurements were made which all generally fall within  $\pm 10\%$  of the Leap 87 measurement (see Figure 4.1). Future calculations will probably disregard Weber 79 and fit the remaining data.

The composition of the primary cosmic rays is also somewhat important, because neutrons produce a few more negative pions and protons produce more positive. This is important for the experiments because the cross sections of neutrinos and antineutrinos differ.

At energies below a few GeV, the primary flux varies with the 11-year solar cycle. When the sun is most active and the solar wind is strongest, it carries a magnetic field that excludes the lowest-energy primaries from the solar system. Bartol and HKKM both use good models of the solar modulation.

### **Nucleon-Nucleus Interactions**

Most of the primaries that interact are protons, and heavier primaries can be considered as a superposition of independent nucleons; thus the relevant primary reaction is nucleon-nucleus where the nucleus is a component of air. A hadronic interaction model determines several quantities, which are in general energy-dependent: the multiplicity of produced mesons, the energy spectrum of produced mesons, the  $\pi^+/\pi^-$  ratio and the  $\pi/K$  ratio. All of these will directly impact the neutrino fluxes. Note that the approximation that cross sections scale, necessary to find an analytic solution, has been abandoned in the Monte Carlo approach in favor of energy-dependent functions.

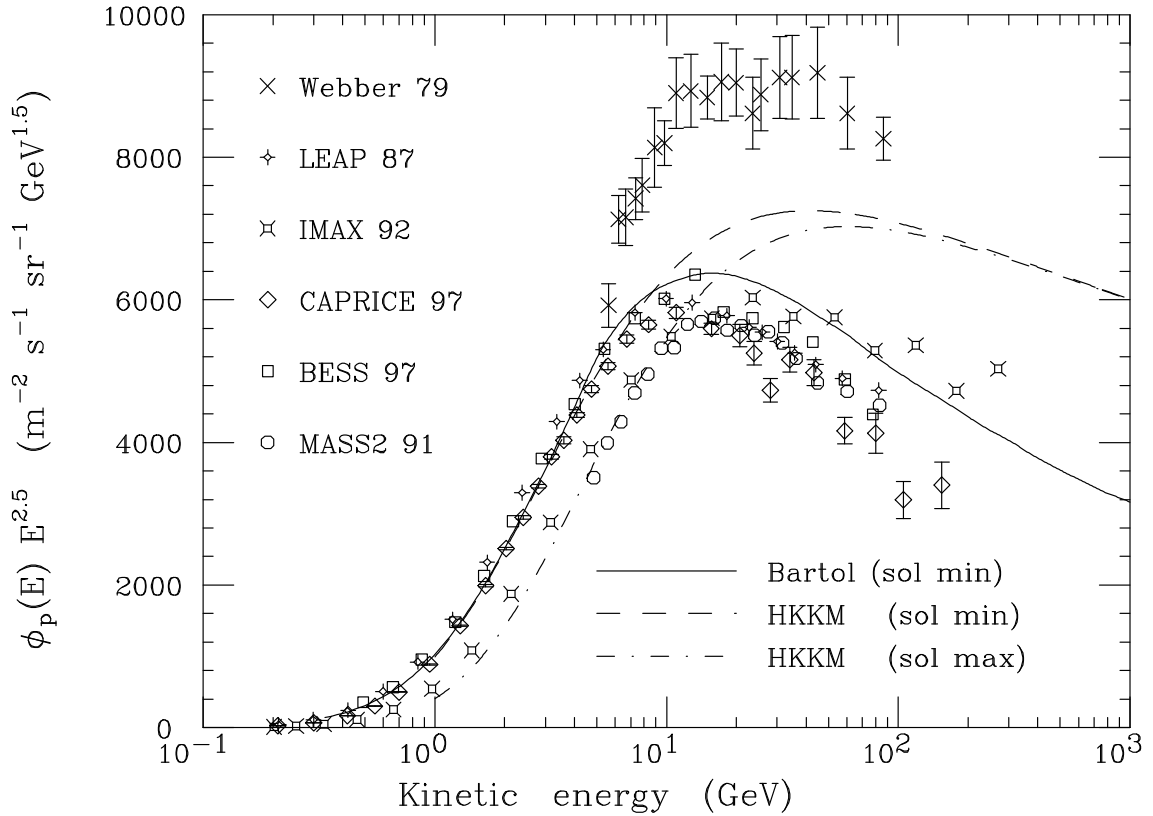


Figure 4.1: Measurements of the primary flux of cosmic ray protons. Note that the flux below 10 GeV depends on solar epoch; IMAX [75] and MASS2 [76] made their measurement near solar maximum while LEAP [74], CAPRICE [77] and BESS [78] were near minimum. Also shown are the flux models used by the Bartol and HKKM calculations. (Figure is due to Lipari [79].)

The multiplicity and spectrum of pions in proton-nucleus interactions is well-measured only for those pions that carry off a large fraction of the primary nucleon's energy (e.g.,  $>\approx 20\%$  for protons on beryllium at 20 GeV). For softer pions, the extrapolation is entirely based on the model of nuclear effects used in the calculation, with HKKM using the Lund color string-based model FRITIOF [80], and Bartol using their own TARGET model, based on a parametrization [81] of pseudorapidity distributions in nucleon-nucleus reactions.

## Atmospheric Muon Fluxes

Muon fluxes are necessarily calculated as an intermediate step in the calculation of neutrino fluxes, so the model can be checked by comparing it with experimental muon data. The calculated flux of high-energy muons that reach the ground can be compared with reliable high-statistics measurements of muons at ground-level. However, at lower energy muons decay in flight so measurements must be made in the atmosphere. There have been several recent measurements of atmospheric muons as a function of height, taken during the ascent of balloon experiments. In the flux calculations, a wrong primary flux can be compensated by a wrong lepton yield per primary particle to yield a correct muon flux. Indeed HKKM and Bartol have differences of order tens of percent in their primary fluxes and interaction models in compensating directions, so that both models match the muon data at ground level, and predict very similar neutrino fluxes. Their agreement with higher altitude muons is less impressive.

The Monte Carlo approach can add in two terms that were ignored in the analytic calculation: ionization loss of propagating muons in the atmosphere (which would amount to about 2 GeV for a muon traversing the entire atmosphere) and hard interactions of muons in air.

## The Earth's Magnetic Field

The geomagnetic field plays a significant role in modifying the neutrino flux, especially at neutrino energies below about 1 GeV. The most important effect is the suppression of low-energy primaries. As charged particles approach the earth they begin to bend in the earth's magnetic field, with the degree of bending determined by the particle's rigidity, which is the ratio of momentum to charge. The lowest-rigidity particles will be bent away so that they will never reach the earth.

For calculation, it is more fruitful to think of the problem backwards. Is it possible for a primary to approach from a certain angle at a certain point in longitude and latitude? By running the equations of motion backward it is possible to determine

if the particle originated from infinity. If the particle’s past trajectory is trapped in the earth’s magnetic field, or if the past trajectory passed through the earth, the trajectory is not a possible source of primaries. We will refer to such trajectories as “forbidden,” and all other trajectories as “allowed.”

The problem was solved analytically by Störmer [82] in 1930 for a perfect dipole field, and neglecting the shadowing effect of the solid earth. If the dipole strength is  $M$ , at a given magnetic latitude  $\lambda_M$ , a positive particle is allowed to approach from position  $(r, \theta_{zen}, \phi)$  (where  $\theta_{zen}$  is the local zenith angle,  $r$  is the radius measured from the dipole’s center, and  $\phi$  is a local azimuthal angle measured clockwise from local magnetic north) if its rigidity is greater than the Störmer rigidity,

$$R_S^+(\lambda_M, r, \theta_{zen}, \phi) = \left( \frac{M}{2r^2} \right) \left\{ \frac{\cos^4 \lambda_M}{[1 + (1 - \cos^3 \lambda_M \sin \theta_{zen} \sin \phi)^{1/2}]^2} \right\}$$

Note that the rigidity cutoff is greatest at the magnetic equator and vanishes at the poles (where a particle can ride in along a magnetic field line). The zenith angle dependence shows that in the  $\sin \phi > 0$  hemisphere, horizontal particles have a higher cutoff than vertical; while the opposite holds in the other hemisphere. Finally, the cutoff is greatest for particles arriving from the east and moving to the west (see Figure 4.2). This last result breaks the azimuthal symmetry of the neutrino flux, and is known as the east-west effect. It was measured in charged particles in 1933 [83, 84]. Super-Kamiokande recently made the first observation of the effect in neutrinos [85]. For the earth, the maximum Störmer rigidity is for a horizontal particle traveling east at the magnetic equator,  $(R_S)_{max} = M_{\oplus}/2r_{\oplus}^2 = 60$  GV. (The unit GV is 1 GeV divided by the charge of one electron, so 60 GV would correspond to a 60 GeV proton or a 120 GeV alpha, etc.) For most locations on the earth and most directions of approach, the cutoff is substantially less.

Geomagnetic effects also break the up-down symmetry of the neutrino flux. Consider a detector at low magnetic latitude, where the cutoff is larger than average. All the downgoing neutrinos originate within tens of kilometers, and have the same cutoff, so the flux of downgoing neutrinos will be lower than average. However, the

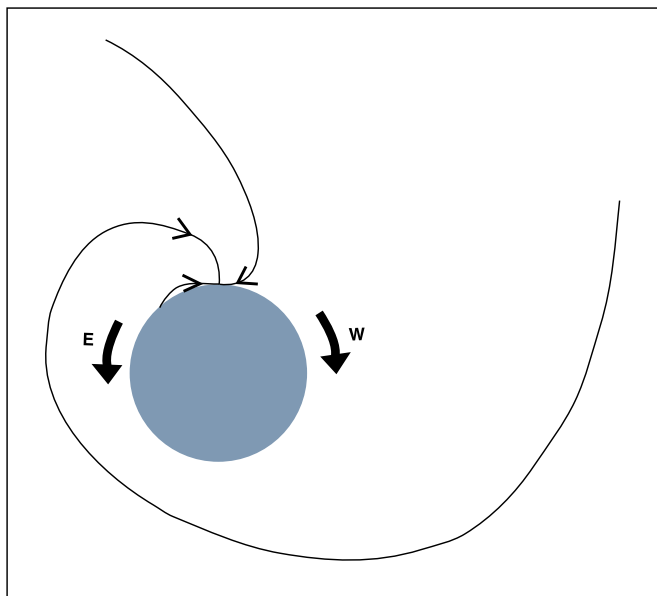


Figure 4.2: The origin of the east-west effect. The circle is a slice of earth perpendicular to the magnetic axis. Three trajectories are shown approaching the same point on earth, for positively-charged particles with the same rigidity but different origins. The west-going trajectory is forbidden, so the west-going flux is reduced. Likewise, the rigidity cutoff for the vertical trajectory would be more than that for the east-going trajectory.

upgoing neutrinos come from all over the earth and their flux will be close to average. Thus, that detector will see fewer downgoing neutrinos than upgoing. For detectors at high latitude, the asymmetry goes the other way. However, at neutrino energies above a few GeV, the neutrinos come from primaries that are above cutoff and the up-down symmetry is restored.

A multipole expansion of the earth's magnetic field shows it is 90% dipole; however, both Bartol and HKKM forgo the perfect dipole model and calculate the trajectories in a detailed model of the actual geomagnetic field, the International Geomagnetic Reference Field [86].

By Liouville's Theorem, the flux remains constant along a trajectory in a magnetic field. Therefore, the geomagnetic cutoff can be implemented in a Monte Carlo calculation by simply throwing an isotropic flux of primaries and then eliminating those that come from forbidden trajectories.

All modern calculations consider the effect of the geomagnetic field on primaries, but so far no detailed calculations have included geomagnetic effects on secondaries. Muons travel long distances and can be affected by the earth's field. Lipari has recently shown [87] that near horizontal, the east-west effect is enhanced for decay products of  $\mu^+$  (i.e.,  $\nu_e$  and  $\bar{\nu}_\mu$ ) and depressed for the daughters of  $\mu^-$  (i.e.,  $\nu_\mu$  and  $\bar{\nu}_e$ ). Due to the different cross sections for neutrinos and antineutrinos, this affects the zenith angle distribution. It is most significant for neutrinos below 1 GeV.

### Transverse Momentum of Secondaries

Probably the most important limitation of HKKM and Bartol is that they suppress the three-dimensional kinematics of the interactions in the atmosphere. This results in an enormous simplification of the computation. One can initially calculate the distribution of neutrino yield from nucleons in the atmosphere of various energies, independent of angle. Then one can generate events choosing only primaries that point at the detector. If the trajectory of the primary is allowed (in the sense defined in the previous section), the neutrino yield is sampled from the pre-calculated distribution. If the trajectory is forbidden, it makes no contribution to the neutrino flux.

It was long assumed that any effects due to the non-collinearity of real shower development would average to zero, or at least something negligible. For high-energy neutrinos, where the opening angle in each reaction or decay is small, this is approximately true. However, for low-energy neutrinos which can have wide opening angles, it becomes possible for trajectories to migrate preferentially out of a high-density region of phase space into a lower-density region and the distributions can be greatly affected. For example, the FLUKA-3D calculation has shown that the near-horizontal flux of neutrinos below 1 GeV is greatly enhanced by including transverse momentum with wide opening angles, and Lipari has given a qualitative explanation [88].

Including the effect of the geomagnetic field on secondary muons (discussed above) is a second example of three-dimensional effects ignored by HKKM and Bartol.

### 4.1.3 The Bartol Flux

This analysis uses the Bartol flux for acceptance studies and to make predictions of no-oscillations and oscillated measurements in MACRO. The flux tables were computed including geomagnetic effects for the Gran Sasso location by Todor Stanev, using the procedures described in Reference [71] for neutrino energies a GeV and below, and Reference [70] for energies above 1 GeV.

For energies below 10 GeV, the calculation was done separately for solar minimum and solar maximum epochs. When running the code, a solar midcycle choice is also available, which just returns the average of the solar minimum and solar maximum fluxes. Also, geomagnetic effects on primaries were only considered for neutrino energies below 10 GeV. Both of these effects are negligible for neutrinos above 10 GeV. So above 10 GeV the flux is up-down symmetric, while for energies below 10 GeV the fluxes are different for upgoing and downgoing particles. While an east-west effect would have appeared in the original Monte Carlo events on which the tables are based, the tables were calculated integrating over azimuthal angle.

The final tables depend on three indices – neutrino type ( $\nu_\mu, \nu_e, \bar{\nu}_\mu, \bar{\nu}_e$ ), neutrino energy, and zenith angle. For a given neutrino type, the flux at a given energy and zenith angle is found by finding three energy bins surrounding the desired energy and interpolating across angle bins for each to find the flux at the given angle, and then interpolating across these energies to find the flux at the given energy and angle. The data is binned in 63 energy bins, spaced logarithmically from 50 MeV to 100 TeV, and in 12 angular bins for  $\cos\theta_{zen} = (1.00, 0.75, 0.50, 0.25, 0.15, 0.05, -0.05, -0.15, -0.25, -0.50, -0.75, -1.00)$ . The flux is assumed to be the same in all azimuthal directions.

Figure 4.3 shows some results of the flux calculation.

## 4.2 Neutrino Cross Section

After the flux is calculated, the other major ingredient of a neutrino interaction rate calculation is the neutrino cross section. This section introduces the basic concepts,

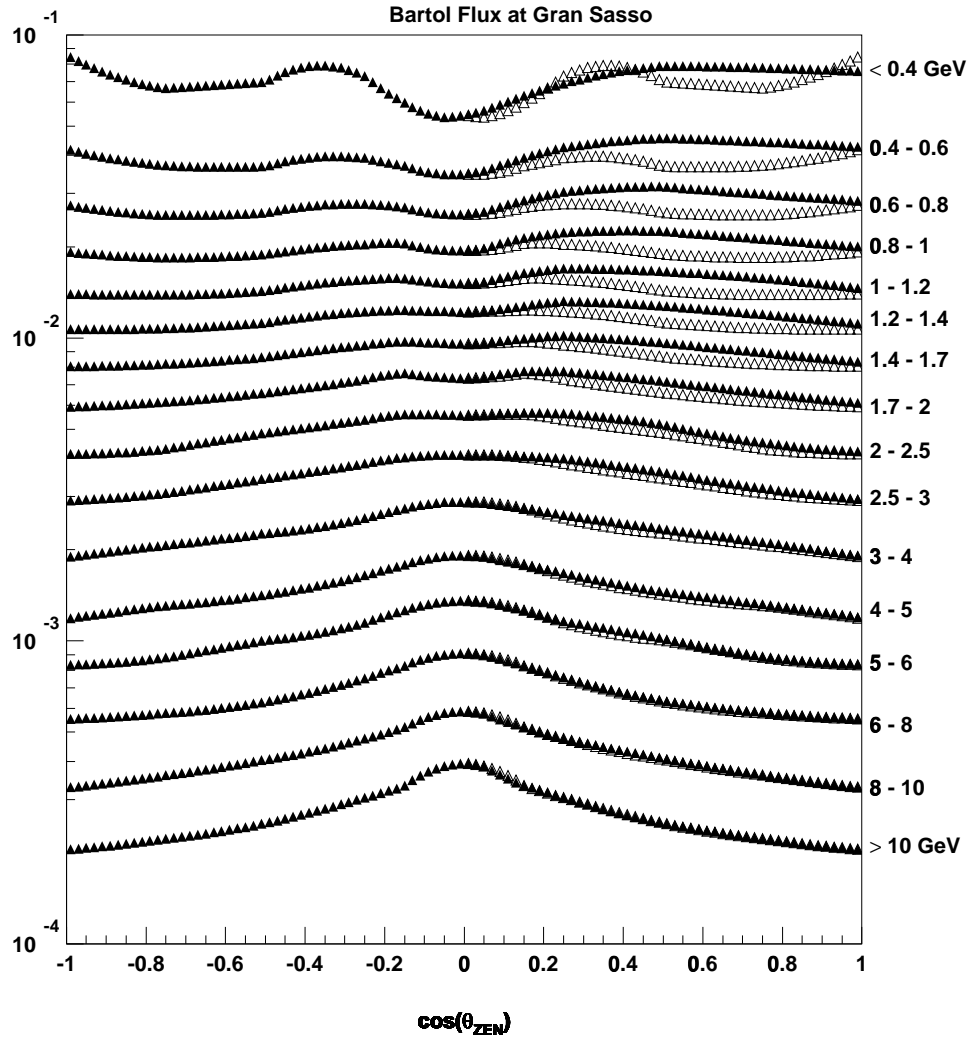


Figure 4.3: The Bartol flux, calculated using geomagnetic effects at Gran Sasso. As a function of zenith angle, the flux is shown in several energy bands. The relative normalization shown is not always accurate, having been adjusted to cleanly separate each band in the figure. The open symbols are the upgoing flux reflected across the horizontal to give a sense of the up-down asymmetry. Less than 1% of detectable events in this analysis come from neutrinos below 0.4 GeV.

and explains a number of models and approximations that have been used. Finally, two particular calculations are described – the Lipari model, on which the predictions for this analysis are based, and the NEUGEN model which has been used as an

independent check.

Most atmospheric neutrinos pass through MACRO without depositing any measurable energy. It is only the rare neutrino that undergoes a hard interaction that produces a detectable event. (A 1 GeV neutrino traversing MACRO from top to bottom has an interaction probability of a few per trillion.) The present work measures primarily muons resulting from the charged current interaction of muon neutrinos or antineutrinos. Neutral current and electron neutrino interactions must also be considered as a lesser source.

The weak cross section for a neutrino to scatter off a point particle of mass  $M$  goes as  $s$ , the Mandelstam variable, which is  $M^2 + 2 M p_{\text{LAB}}$ . In ordinary matter the number of electrons is of the order of the number of nucleons but the cross section is around three orders of magnitude lower due to the low electron mass; so we can neglect neutrino-electron scattering and concentrate on neutrino-nucleon scattering.

Different conceptual models are used to discuss neutrino-nucleon interactions in different regimes. We can discuss all of them with a common set of kinematic variables, illustrated in Figure 4.4. In the figure, quantities represented as  $\vec{x}$  are four-vectors.

At high  $Q^2$ , the neutrino is interacting with the partons within a nucleon, and the formalism of Deep Inelastic Scattering (DIS) is applicable. The standard model gives exact formulas for the coupling of neutrinos to partons. Published phenomenological *parton distribution functions* give the probabilities of partons carrying a given fraction of the nucleon momentum. Parton distribution functions have been determined using a variety of experimental probes – electron-nucleon scattering, muon-nucleon scattering, neutrino-nucleon scattering and nucleon-nucleon scattering. If the parton model were perfect, all of these probes would give the same result. In reality, there are small but significant differences, and not all structure functions reproduce neutrino scattering data well.

The lepton kinematics can be fixed in inelastic events by choosing two independent scalar variables. Most Monte Carlo calculations choose  $x$  and  $y$ .  $y$  is chosen according to  $\frac{d\sigma}{dy}$  integrated over all  $x$ , and after  $y$  is fixed  $x$  is chosen with the aid of the parton

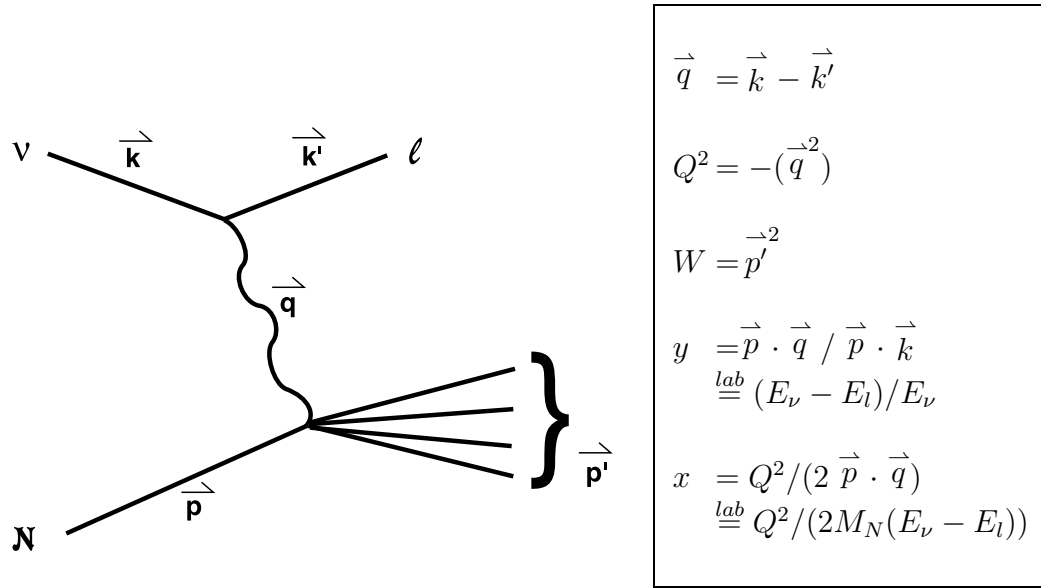


Figure 4.4: Neutrino interaction kinematics.

distribution functions.

The choice of  $x$  and  $y$  gives the lepton kinematics unambiguously; however, the hadronic situation is confused. After the interaction, there is a struck parton plus spectator partons at rest in the lab. Some phenomenological hadronization prescription must be applied to produce the observable hadrons.

At smaller  $Q^2$ , the neutrino “sees” the nucleon as a coherent whole, and perturbative calculations are not applicable. Most of the non-perturbative portion of the cross section is included in two cases: quasi-elastic scattering ( $\nu n \rightarrow l^- p$  or  $\bar{\nu} p \rightarrow l^+ n$ ) and single pion production (QEL and 1PI, respectively). Note that while most of the cross section of high energy (multi-GeV) neutrinos is deep inelastic, even very high energy neutrinos may sometimes participate in a low  $Q^2$  event, so the non-perturbative cross section applies at all energies.

In the quasi-elastic case, the final hadronic mass is predetermined and one variable (perhaps  $Q^2$ ) suffices to specify the kinematics. Due to Lorentz invariance and other symmetries, the uncertainty in quasi-elastic scattering may be confined to a few form factors, as in the classic treatment of Llewellyn Smith [89]. The hadronic current is

written in terms of scalar, pseudoscalar, vector, axial vector and tensor form factors. The scalar and tensor factors are assumed zero due to the non-observation of “second-class currents.” The pseudoscalar factor contributes proportional to  $M_l/M_N$  and may be ignored. The vector form factor may be related to well-determined electromagnetic form factors via the “Conserved Vector Current” hypothesis. Only the axial vector form factor is undetermined. Its value at  $Q^2 = 0$  is known from nuclear beta decay, and in neutrino scattering experiments it has been determined that the  $Q^2$  dependence is consistent with a dipole form,

$$F_A(Q^2) = \frac{-1.23}{(1 - Q^2/M_A^2)^2}$$

with  $M_A$  around 1 GeV.

Because the neutrino usually reacts with a bound nucleon rather than a free nucleon, the naive cross section is modified by nuclear effects. The most important are the Fermi motion of nucleons confined to the nucleus, and Pauli blocking in which some low-energy-transfer events are forbidden because the scattered nucleon is excluded from the energy level to which it would otherwise go.

The situation for single pion production is more complex. The extra degrees of freedom make a simple form factor approach unworkable. Fogli and Nardulli [90] have calculated differential cross sections in good agreement with available data using a number of restrictive assumptions, applying some form factors known from quasi-elastic scattering, and summing a number of effective Feynman diagrams using exact propagators of all relevant resonances. They also include a non-resonant background and calculate interference terms with the resonances. Rein and Segahl [91] have taken a different approach, modeling the nucleon as three point particles with harmonic oscillator potentials between each pair using a hamiltonian suggested by Feynman, Kislinger and Ravndal [92]. Each excited state of the nucleon can be related to a real baryonic resonance by comparing quantum numbers, and the matrix elements for a weak charged current interaction to excite the ground-state nucleon to a particular resonance can be calculated exactly.

Because the hadronization process in DIS is not straightforward, there is no clear boundary between DIS and resonant production. If one takes account of single pion production completely in the exclusive channel, any events in the inclusive (DIS) channel that result in single-pion production may be double counting that part of the cross section. Two approaches have been taken to this problem.

One may omit the calculation of the exclusive channels (quasi-elastic or resonant scattering). By considering higher order QCD effects in extrapolating structure functions to small  $x$  (where experimental measurements do not extend), one may hope to be effectively compensating for non-perturbative effects. In the 1990s, due to the electron-proton collider HERA, structure functions became available which were valid to lower values of  $x$  than any earlier structure functions.

Other models do a full calculation in both the inclusive (DIS) and exclusive channels, but apply some prescription for subtracting a fraction of one or both cross sections to eliminate the double-counting.

### 4.2.1 The Lipari Cross Section Model

The final results in this analysis are compared with the theoretical prediction incorporating a cross section model due to Lipari<sup>1</sup>. The main feature of the Lipari model is that it incorporates the no-double-counting prescription of Lipari, Lusignolo and Sartogo [93] which calculates three cross sections:

$$\sigma_{\text{TOT}} = \sigma_{\text{QEL}} + \sigma_{\text{1PI}} + \sigma_{\text{DIS}}$$

where the 1PI cross section is restricted to final state hadronic mass  $\sqrt{W}$  (see Figure 4.4) of less than 1.4 GeV and the DIS cross section to above 1.4 GeV. This eliminates the low  $Q^2$  events, which are dominated by the exclusive channels, from being counted as part of the DIS cross section.

This model reproduces well the total cross section data at high energy, as well as the Brookhaven data at sub-GeV energies (see Figure 4.5). However, experimental

---

<sup>1</sup>Lipari is a MACRO collaborator, but the code is freely available.

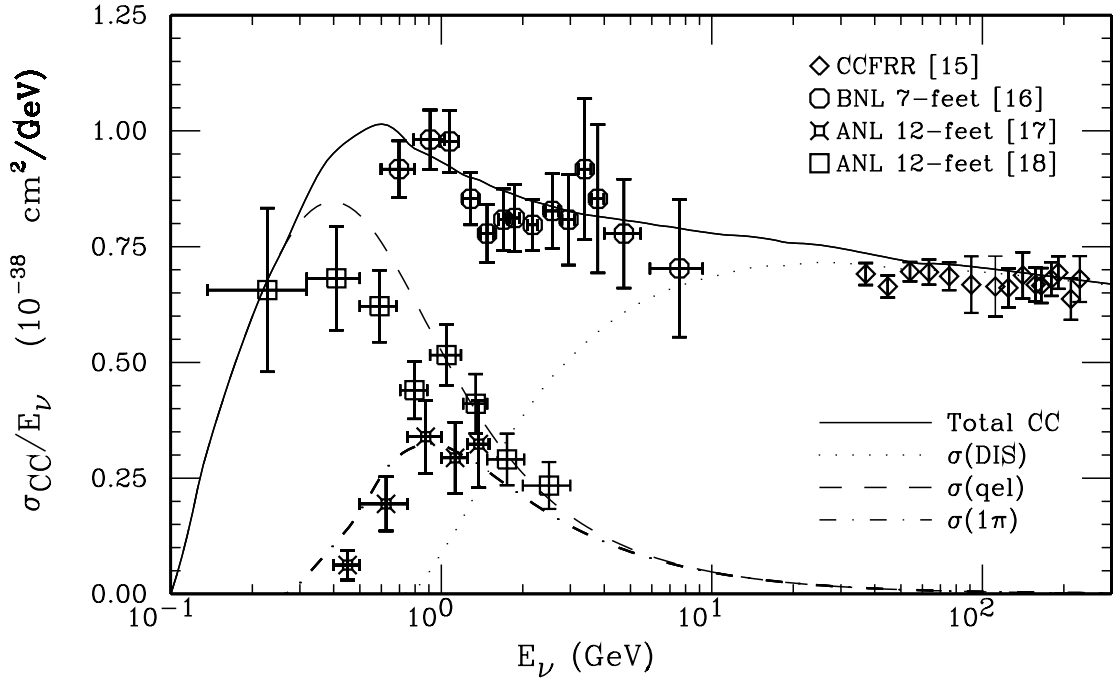


Figure 4.5: Comparison of the  $\nu_\mu$  charged current cross section with selected experimental data. Figure is reproduced from Reference [93].

data exists in contradiction to the Brookhaven data. Furthermore, where this model predicts an enhancement of the antineutrino cross section at sub-GeV energies, existing data seem to show a decrease.

For the quasi-elastic cross section, Lipari uses the equations of Llewellyn Smith described above, with axial mass  $M_A = 1$  GeV. Neutral current elastic scattering is omitted from the model.

Lipari calculates the one-pion cross section according to

$$\sigma_{1\text{PI}}(Q^2) = \int_0^{W_{max}} dW \sigma_{FN}(Q^2, W)$$

where  $\sigma_{FN}$  is the cross section of Fogli and Nardulli (described above) and  $W_{max}$  is  $(1.4 \text{ GeV})^2$ ; i.e., his one-pion total cross section at some value of  $Q^2$  is the total cross section of Fogli and Nardulli with the portion resulting in a final hadronic mass over 1.4 GeV subtracted out. However, to simplify the calculation, the exact differential

cross section of Fogli and Nardulli is not used; instead the process is assumed to pass through the  $\Delta$  baryonic resonance, with the resonant mass sampled from the  $\Delta$  Breit-Wigner distribution ( $M_\Delta = 1.2$  GeV and  $\Delta M_\Delta = 120$  MeV) and a simple phase space decay to a nucleon and one pion. Note that any final states with a hadronic mass less than 1.4 GeV and more than one pion cannot be produced in this model. Finally, note that the lepton spectrum is exactly that of Fogli and Nardulli; only the hadronic state is affected by the approximation.

In the code provided by Lipari, the deep inelastic cross section is calculated to leading order, and any leading-order parton distribution functions may be used, via the CERNLIB code PDFLIB [94]. We choose the GRV94-LO set [61]. (The authors have published a minor update, GRV98-LO [95]. The new version changes total cross section by less than 1/2% and does not noticeably change the lepton kinematic distributions.) Immediately after the charged current interaction, the hadronic system consists of a struck parton and two spectator partons, which are handed to the Lund string fragmentation model [96] to produce the final hadronic state. Beginning with a quark and a diquark, Lund will correctly produce an energetic leading hadron in the lab frame containing the struck quark, and will conserve baryon number.

### 4.2.2 The NEUGEN Cross Section Model

As a consistency check, the prediction of the Lipari model has been compared with a prediction incorporating a completely independent cross section model, NEUGEN, which was originally developed for the Soudan experiment by Giles Barr [97] and subsequently extended by Hugh Gallagher [98] and Geoff Pearce. It is now maintained by the MINOS collaboration.

This model also computes separate cross sections for quasi-elastic, resonant, and deep inelastic scattering processes. The prescription to avoid double counting is less sophisticated than Lipari; a fixed fraction of the low-multiplicity part of the deep inelastic cross section is suppressed by hand.

The quasi-elastic calculation is essentially identical to that of Lipari, with an axial

mass  $M_A = 1.032$  GeV.

The resonant cross section implements the model of Rein and Segahl (described above), considering 17 different resonances of the baryon.

The neutrino-parton cross section for the deep inelastic process is computed using any available parton distribution functions from PDFLIB; we again choose GRV94-LO. The hadronic final state is considered as a coherent whole, with a mass and momentum given by the kinematic variables  $x$  and  $y$ . A final hadronic multiplicity is picked based on the mass according to the KNO distribution [99], and the various kaons, pions and nucleon are assigned momentum probabilistically according to available phase space. This leads to inaccurate momenta distributions for high  $Q^2$  events, with no energetic leading hadron.

## Chapter 5 Measurement of Neutrino Interactions in the Detector

### 5.1 Topologies of Neutrino-Induced Muons in MACRO

Neutrino-induced muons detectable by MACRO can exhibit any of several topologies (see Figure 5.1).

Category (a), Throughgoing Upward Muons, are the most numerous detectable neutrino-induced events in MACRO. MACRO has been publishing results on this topology since 1994. This thesis does not update results on this topology.

Categories (b) (Throughgoing Downward Muons) and (c) (Stopping Downward Muons) are unfortunately indistinguishable in MACRO from the overwhelming background of atmospheric muons (muons produced in the atmosphere by cosmic ray showers) and MACRO cannot discern anything about neutrinos from these topologies.

Category (d) (Contained-Vertex Upward Muons) is the topic of this analysis. In this topology, the direction (upward or downward) must be determined to distinguish category (d) from stopping atmospheric muons which have the same topology as (c). In MACRO the direction is determined by scintillator timing between two layers (by observing whether the lower box was hit before or after the upper box). Therefore, this analysis requires the muon to hit the Center layer and a higher tank.

Categories (e) (Contained-Vertex Downward Muons) and (f) (Stopping Upward Muons) are indistinguishable from each other in MACRO. The direction (upward or downward) cannot be determined because the muon does not hit two scintillator layers. However, all the events of these categories are neutrino-induced, and it is possible to make neutrino measurements based on this topology. MACRO has published

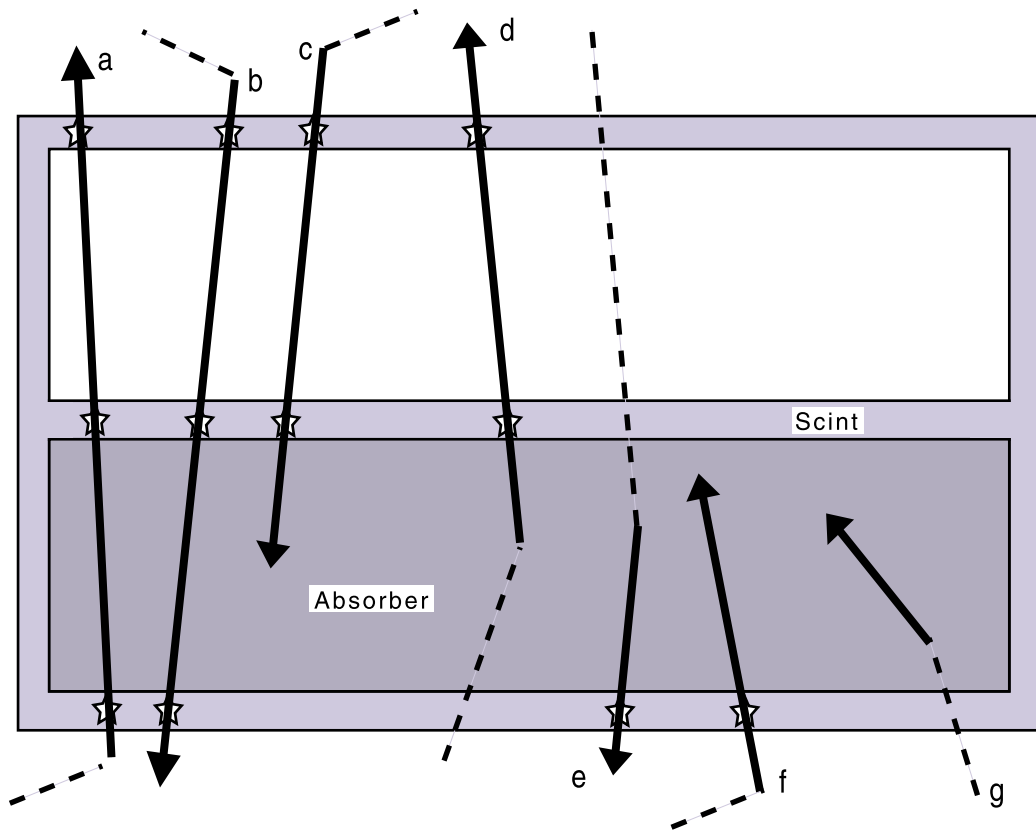


Figure 5.1: Topologies of neutrino-induced muons in MACRO. The sense (upgoing or downgoing) can be determined only for those tracks with two or more scintillator hits (represented by white stars). (a) Throughgoing Upward Muons – ANALYZED; (b) Throughgoing Downward Muons – NOT ANALYZED; (c) Stopping Downward Muons – NOT ANALYZED; (d) Contained-Vertex Upward Muons – ANALYZED IN THIS WORK; (e) Contained-Vertex Downward Muons – ANALYZED; (f) Stopping Upward Muons – ANALYZED; (g) Fully-Contained Muons – NOT ANALYZED.

results on this topology [52]. This analysis does not update results on this topology, although it does rely on updated results in Chapter 6, Interpretation.

Finally, category (g) (Fully-Contained Muons) could perhaps be measured. However, MACRO is too granular to make this measurement well, and no attempt has been made at its analysis.

For the three topologies that have been analyzed ((a), (d) and (e)+(f)), Figure 5.2 gives the energy distribution (from a Monte Carlo calculation assuming  $\nu_\mu$  disappearance with maximal mixing and  $\Delta m^2 = 3.2 \times 10^{-2} \text{ eV}^2$ ) of the parent neutrinos

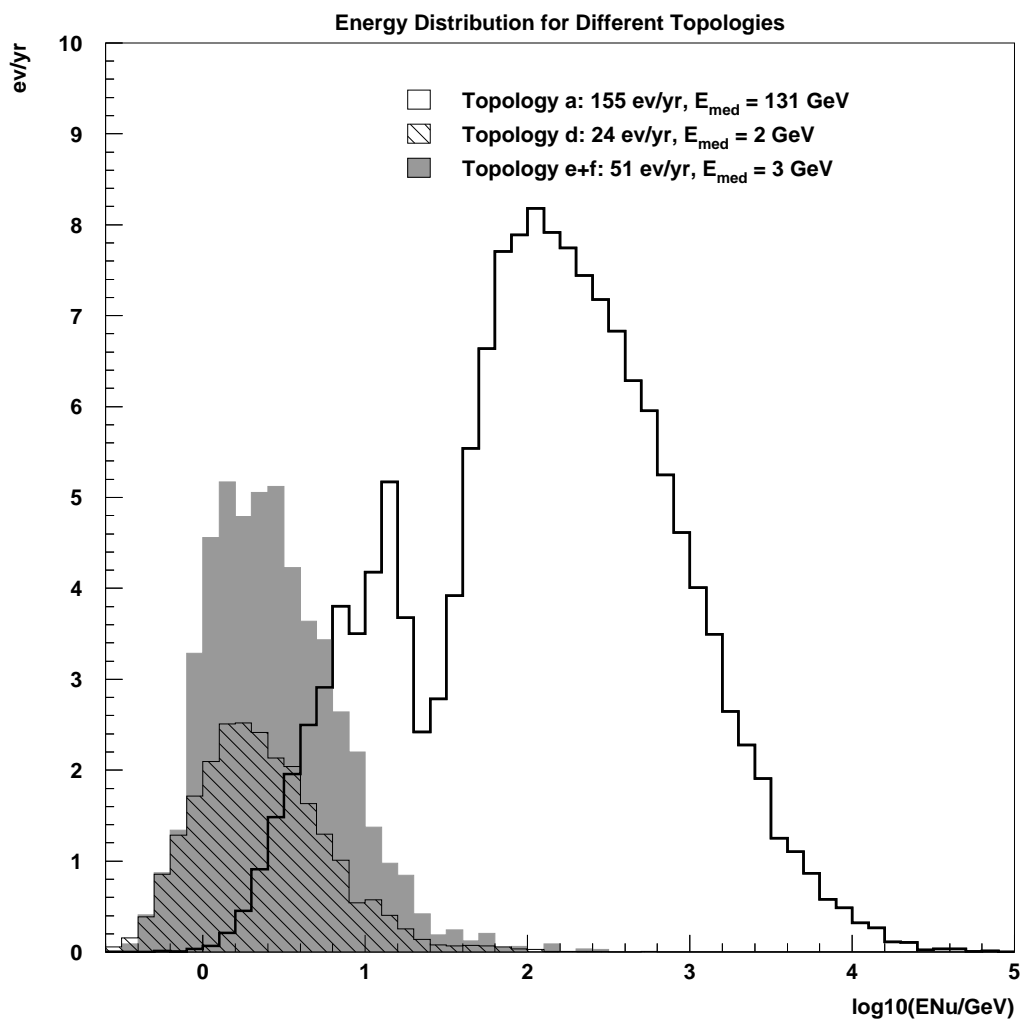


Figure 5.2: Energy distribution of parent neutrinos giving rise to detectable events in MACRO.

giving rise to detectable events, based on the cuts made in the analyses identifying the events.

### 5.1.1 Topology Criteria for This Analysis

About five kilotonnes, 89% of the mass of MACRO, resided below the tenth layer of streamer tubes (which rested on the Center layer of scintillation tanks). Most of the

mass was in the crushed rock absorber, the iron trays containing the absorber, and the structural iron. This region of MACRO will be referred to as “lower MACRO.” The neutrino interactions in the detector follow the mass distribution (approximately – the interaction rate also depends on the  $Z/A$  ratio, which varied between 0.47 (iron) and 0.51 (oil) in the various materials making up MACRO). This analysis limits itself to neutrino interactions in lower MACRO which produce an upgoing muon that fires a scintillator box in the Center layer as well as a higher scintillator box.

In overview, the analysis proceeds by identifying a candidate streamer tube space track associated with fired scintillator boxes in the C layer and the attico. Next, a containment cut is applied to ensure that the track begins in lower MACRO (or ends in lower MACRO if it is a downgoing stopping muon). The event is then examined and rejected if it has any characteristic that casts the accuracy of the timing in doubt. Finally, those events with time of flight consistent with an upgoing muon are selected as the event sample.

## 5.2 The Dataset

### 5.2.1 Data Flow and Analysis Software

Fundamentally, we want to use the streamer tubes to identify the track of a penetrating particle in the detector, and use the scintillator timing to determine if the particle was upgoing (which means it was almost certainly neutrino-induced) or downgoing (probably an atmospheric muon). Practically, we want to write a computer program that utilizes all the information recorded in MACRO events to identify muons of various classes.

In the Gran Sasso lab, whenever electronics (e.g., the ERP) monitoring the apparatus identified a “trigger” condition (e.g., ERP muon trigger), the status of various streamer tube and scintillator electronics were read by a computer and stored on disk as one “event.” A “run” is a collection of consecutive events; a run typically lasted a few hours and contained about  $10^4$  events (many events caused by other triggers had

no muons), although it was possible for a run to be much shorter. All of the events from one run are kept in one file on disk.

The file containing all the events in a run may be converted to new formats or archived to tape. The dataset on which this analysis is based is composed of runs that had irrelevant information deleted and were stored in a compact format called the Muon Analysis Data Summary Tape (MUADST). MUADSTs were created on a VAX/VMS computer using unformatted FORTRAN WRITE statements. MUADST files arrived at Caltech by many different routes. Many were transferred to tape in a raw format and read on the Caltech High Energy Physics IBM RS/6000 computers utilizing a machine translation algorithm. Some runs were converted by MACRO collaborator Colin Okada to a transportable format called DSTZ and brought to Caltech on tape. Still other runs were transferred over the internet from Gran Sasso computers in raw MUADST format.

Regardless of the format in which received, all runs were converted to a common format called Fisica Analisi Rete Facendo Altrimenti Letargico Lavoro Allegro (FARFALLA)<sup>1</sup> [100]. FARFALLA is a C++ class library (developed by me and MACRO collaborator Chris Walter) for creating and using custom data summary files (DSTs). FARFALLA stores data in a tree structure in which small nuggets of related information are placed into a “node” on the tree. For example, all of the ERP information (raw values of ADCs and TDCs, as well as reconstructed values such as energy and time) for a single hit scintillator box resides in one node. In the FARFALLA DST files on disk or tape, all of the nodes with information from the same event are collected together into one event tree (see Figure 5.3). A file consists of many trees (i.e., many events). Walter and I created a software distribution called MACROFAR which contains FARFALLA node definitions for several different kinds of information that would commonly be used in DSTs for MACRO. Many of these nodes contain reconstructed data, including ERP timing reconstructions and reconstructed streamer tube tracks. The FARFALLA DSTs created for this analysis contain only nodes defined

---

<sup>1</sup>This is very bad Italian, which literally translates Physics Analysis Network Making Otherwise Dull Work Exciting and Gay. The acronym, FARFALLA, is the Italian word for butterfly.

in MACROFAR, enumerated in Figure 5.4.

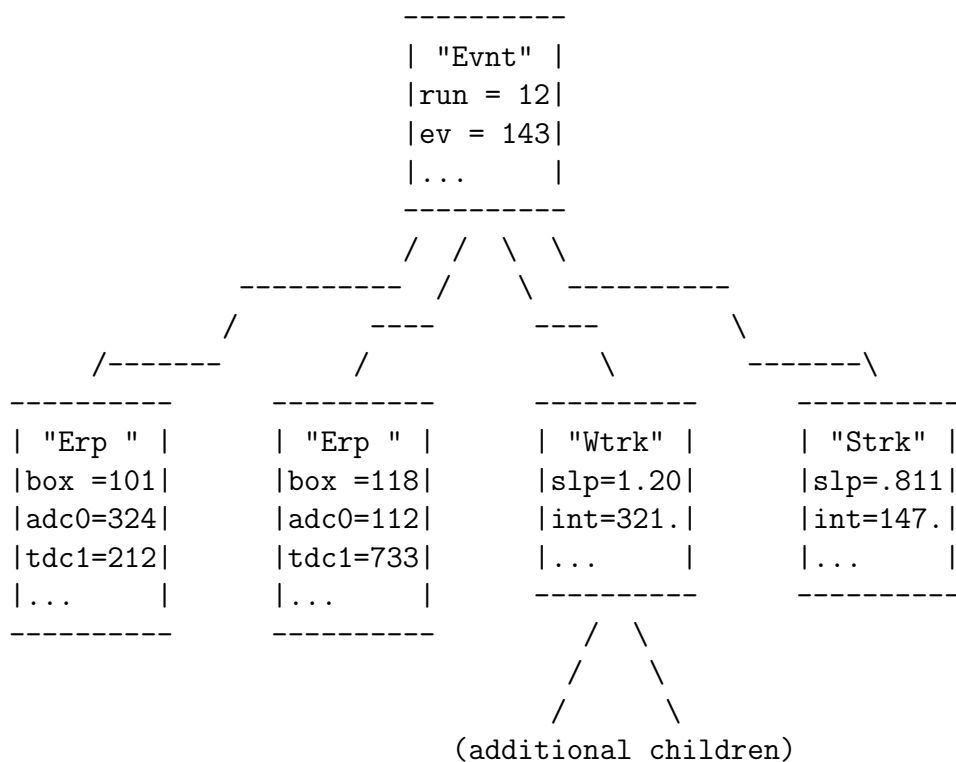


Figure 5.3: An example of a FARFALLA event tree.

<b>triggerNode</b>
<b>timeNode</b>
<b>erpNode</b>
<b>interErpNode</b>
<b>wireTrackNode</b>
<b>stripTrackNode</b>
<b>lateralTrackNode</b>
<b>otherWireHitsNode</b>
<b>otherStripHitsNode</b>
<b>otherLateralHitsNode</b>
<b>otherFrontalHitsNode</b>
<b>otherLstripHitsNode</b>

Figure 5.4: Nodes in the DSTs forming the dataset for this analysis.

Analysis of the FARFALLA DSTs takes place in a software environment called Data Analysis SHell (DASH) [101], developed by MACRO collaborator Ed Kearns. When integrated with FARFALLA, DASH reads one event tree from disk into memory, and then calls several user-written “modules” to operate on the tree in memory. Some modules might create new nodes and add them to the tree, which will be visible on the tree to subsequent modules. Some modules act as “filters,” meaning they make a decision whether processing will continue (i.e., whether subsequent modules will be called) or the event will be rejected without further processing. After one event is either processed fully or rejected, the next event is read in and processed.

Some of the DASH modules used in this analysis utilize the services of Tracks And Boxes Object-Oriented (TABOO), a class library I wrote that can take information from MACROFAR nodes and do such things as the following:

- Combine streamer tube tracks in different views to form a track in three-dimensional space.
- Given a space track, create a list of scintillator boxes intersected by the track.
- Given a space track, create a list of streamer tube channels intersected by the track.

### 5.2.2 Real Data

The dataset for this analysis extends from Run 7473, 29 Apr 1994, to Run 17701, 02 Jun 1999, a calendar time of 5.1 years.

All runs with run numbers less than 80,000 in the MUADST dataset for this period were converted to FARFALLA. At the time each run was converted, several variables were checked to ensure the quality of the data. I made a subjective decision for each run whether it appeared to be a calibration run (a run with many firings of the calibration LEDs or laser), or if it appeared to have hardware problems so severe they could cause excessive downtime or other inefficiencies (the latter are referred to

as “bogus” runs). Calibration and bogus runs are listed in Figures 5.5-5.6 and were eliminated from the dataset.

As described in Section 3.3, a database was created with the dead periods and weekly efficiency for each scintillator and streamer tube channel. Actually, in creating the database it was found necessary to eliminate a handful of runs that had inconsistent times in the event records. (The time used is that written to the event record by the acquisition computer’s clock, which the MACRO collaboration calls VAX time. The time available from the LNGS atomic clock, when it was working properly, is in principle far more accurate than VAX time; unfortunately, it was also far more prone to malfunctions.) There was nothing really wrong with these runs except that the VAX time irregularity made it difficult to calculate time between events for the efficiency database. The runs that were eliminated at this stage are shown in Figure 5.7.

Remaining are 8362 runs, with 66.4 million events including 23.7 million downgoing events passing the standard muon analysis. Summing the total livetime yields 4.5 years. The difference of 0.6 years between the livetime and the calendar time of 5.1 years is presumably due to scheduled downtime for maintenance and calibrations, short periods of downtime due to acquisition crashes, long periods of downtime due to major equipment failures, and the effect of eliminating runs from the dataset.

### 5.2.3 Simulated Data

The Monte Carlo dataset was generated by running GMACRO, using the GMACRO parameters determined by comparison with downgoing atmospheric muons (Section 3.4.3), with the neutrino flux of the Bartol group (Section 4.1.3) at the Gran Sasso location, and the neutrino event generator of Lipari (Section 4.2.1). Three aspects of the marriage of the detector-independent flux and cross section calculations to the GMACRO detector simulation are discussed below: adjusting the flux to the solar cycle conditions in effect during the data-taking, computing the total interaction rate of atmospheric neutrinos in MACRO, and placing the vertex of the interaction

7489, 7490, 7491, 7492, 7493, 7494, 7495, 7496, 7526, 7527, 7529, 7532,  
 7534, 7535, 7571, 7572, 7573, 7574, 7575, 7577, 7595, 7596, 7597, 7598,  
 7599, 7600, 7601, 7602, 7603, 7604, 7640, 7641, 7642, 7643, 7644, 7645,  
 7646, 7647, 7648, 7649, 7650, 7661, 7680, 7681, 7682, 7683, 7684, 7685,  
 7687, 7688, 7713, 7714, 7715, 7716, 7717, 7718, 7719, 7720, 7721, 7722,  
 7766, 7767, 7768, 7769, 7770, 7775, 7776, 7815, 7816, 7817, 7818, 7819,  
 7820, 7852, 7853, 7854, 7855, 7856, 7857, 7881, 7882, 7883, 7884, 7886,  
 7887, 7888, 7889, 7890, 7891, 7892, 7919, 7920, 7921, 7922, 7923, 7924,  
 7925, 7926, 7927, 7978, 7979, 7980, 7981, 7982, 7983, 7984, 7985, 7986,  
 8022, 8023, 8024, 8025, 8026, 8027, 8058, 8059, 8060, 8061, 8062, 8063,  
 8085, 8086, 8087, 8088, 8089, 8090, 8091, 8092, 8128, 8129, 8130, 8131,  
 8132, 8133, 8134, 8135, 8161, 8163, 8164, 8165, 8166, 8167, 8168, 8169,  
 8170, 8171, 8172, 8173, 8174, 8175, 8199, 8200, 8201, 8202, 8203, 8204,  
 8205, 8206, 8207, 8208, 8218, 8219, 8220, 8257, 8258, 8259, 8260, 8261,  
 8262, 8263, 8264, 8265, 8266, 8267, 8268, 8269, 8270, 8271, 8272, 8273,  
 8274, 8315, 8316, 8317, 8318, 8319, 8320, 8321, 8322, 8323, 8324, 8325,  
 8374, 8375, 8376, 8377, 8378, 8379, 8380, 8381, 8415, 8416, 8417, 8418,  
 8419, 8420, 8421, 8422, 8423, 8424, 8425, 8426, 8470, 8472, 8473, 8476,  
 8477, 8478, 8479, 8480, 8481, 8482, 8522, 8523, 8524, 8525, 8526, 8527,  
 8544, 8545, 8546, 8547, 8670, 8671, 8672, 8673, 8674, 8675, 8676, 8711,  
 8712, 8713, 8714, 8715, 8716, 8717, 8718, 8719, 8767, 8768, 8769, 8770,  
 8771, 8800, 8801, 8803, 8808, 8809, 8811, 8812, 8814, 8854, 8855, 8856,  
 8857, 8858, 8859, 8913, 8914, 8915, 8958, 8959, 8960, 8961, 8962, 9067,  
 9068, 9069, 9070, 9071, 9072, 9073, 9074, 9075, 9076, 9115, 9116, 9117,  
 9165, 9166, 9167, 9168, 9169, 9170, 9171, 9172, 9173, 9174, 9175, 9176,  
 9222, 9223, 9224, 9225, 9226, 9227, 9274, 9275, 9276, 9277, 9278, 9321,  
 9322, 9323, 9324, 9325, 9360, 9361, 9362, 9404, 9405, 9406, 9407, 9408,  
 9409, 9473, 9474, 9475, 9534, 9535, 9536, 9537, 9538, 9577, 9578, 9579,  
 9580, 9581, 9635, 9636, 9637, 9638, 9639, 9640, 9641, 9642, 9643, 9644,  
 9701, 9702, 9703, 9704, 9705, 9813, 9814, 9815, 9864, 9865, 9866, 9910,  
 9911, 9913, 10136, 10137, 10138, 10263, 10264, 10469, 10470, 10520,  
 10521, 10572, 10573, 10575, 10576, 10631, 10632, 10633, 10717, 10723,  
 10724, 10725, 10758, 10759, 10800, 10801, 10802, 10803, 10804, 10805,  
 10806, 10809, 10811, 10815, 10816, 10858, 10860, 10862, 10863, 10864,  
 10865, 10900, 10903, 10904, 10906, 10908, 10909, 10945, 10946, 10951,  
 10994, 10996, 10997, 10998, 10999, 11035, 11036, 11037, 11038, 11039,  
 11040, 11041, 11042, 11043, 11072, 11117, 11625, 11626, 11627, 11628,  
 11695, 11696, 11697, 11698, 11699, 11700, 11701, 11702, 11703, 11704,  
 11705, 11706, 11707, 11708, 11709, 11710, 11711, 11712, 11713, 11753,  
 11754, 11755, 11756, 11757, 11758, 11759, 11760, 11761, 11762, 11763,  
 11764, 11765, 11766, 11767, 11768, 11769, 11770, 11771, 11772, 12507,  
 12508, 12509, 12510, 12512, 12513, 12546, 12547, 12549, 12550, 13184,  
 13186, 13187, 13599, 13637

Figure 5.5: Calibration runs eliminated from the dataset.

7701, 7702, 7735, 7736, 7737, 7758, 7759, 7786, 7787, 7811, 7821, 7822, 7823, 7969, 7970, 7971, 7972, 7973, 7974, 7976, 7987, 8007, 8008, 8009, 8010, 8011, 8055, 8056, 8072, 8105, 8302, 8343, 8369, 8370, 8371, 8391, 8392, 8393, 8504, 8543, 8566, 8575, 8577, 8633, 8732, 8828, 8884, 8894, 8922, 8923, 9119, 9120, 9349, 9352, 9364, 9412, 9413, 9414, 9415, 9416, 9427, 9433, 9446, 9456, 9457, 9520, 9594, 9631, 9649, 9650, 9651, 9669, 9670, 9679, 9709, 9711, 9713, 9714, 9715, 9716, 9717, 9720, 9721, 9730, 9780, 9781, 9782, 9783, 9784, 10594, 10609, 10760, 10761, 10828, 10829, 10969, 10970, 10971, 10972, 10973, 10974, 10975, 11073, 11198, 11199, 11368, 11369, 11414, 11415, 11416, 11417, 11449, 11483, 11484, 11573, 11799, 11801, 11802, 11809, 11812, 11814, 11815, 11816, 11839, 11840, 11841, 11842, 11843, 11844, 11861, 12094, 12193, 12275, 12276, 12283, 12284, 12288, 12309, 12847, 12879, 12977, 12978, 12979, 12980, 12981, 12982, 12983, 12984, 12985, 12986, 12987, 13028, 13049, 13051, 13600, 13601, 13602, 13604, 13605, 13606, 13629, 13630, 13638, 13639, 13640, 13642, 13671, 13702, 13718, 13720, 13723, 13725, 13726, 13727, 13728, 13990, 14007, 14015, 14059, 14075, 14114, 14173, 14210, 14250, 14283, 14381, 14382, 14383, 14384, 14385, 14729, 14753, 14754, 14758, 14759, 14760, 14761, 14762, 14764, 14765, 14766, 14767, 14769, 14770, 14773, 14774, 14775, 14776, 14777, 14882, 14883, 14907, 14908, 14909, 14910, 14923, 15342, 15348, 15349, 15350, 15351, 15579, 15696, 15745, 15813, 15837, 15838, 15850, 15851, 15877, 15897, 15898, 15964, 15965, 16016, 16122, 16123, 16259, 16260, 16265, 16266, 16269, 16303, 16304, 16306, 16307, 16400, 16418, 16490, 16585, 16585, 16587, 16641, 16642, 16782, 16789, 16842, 16843, 17143, 17144, 17148, 17149, 17150, 17151, 17152, 17153, 17233, 17345, 17346

Figure 5.6: Bogus runs eliminated from the dataset.

7724, 8722, 8882, 8907, 8933, 8943, 9094, 9110, 9140, 9195, 9737, 9744, 10071, 10121, 10401, 10402, 10454, 10455, 10480, 11231, 12051, 12816, 13203, 13213, 13991, 14609, 15036, 16426, 17288

Figure 5.7: Runs eliminated from the dataset due to inconsistent VAX times.

in MACRO.

## The Solar Cycle

As mentioned in Section 4.1.2, the neutrino flux at the lowest energies is dependent on the solar cycle. Figure 5.8 shows an actual measurement [102] of solar activity

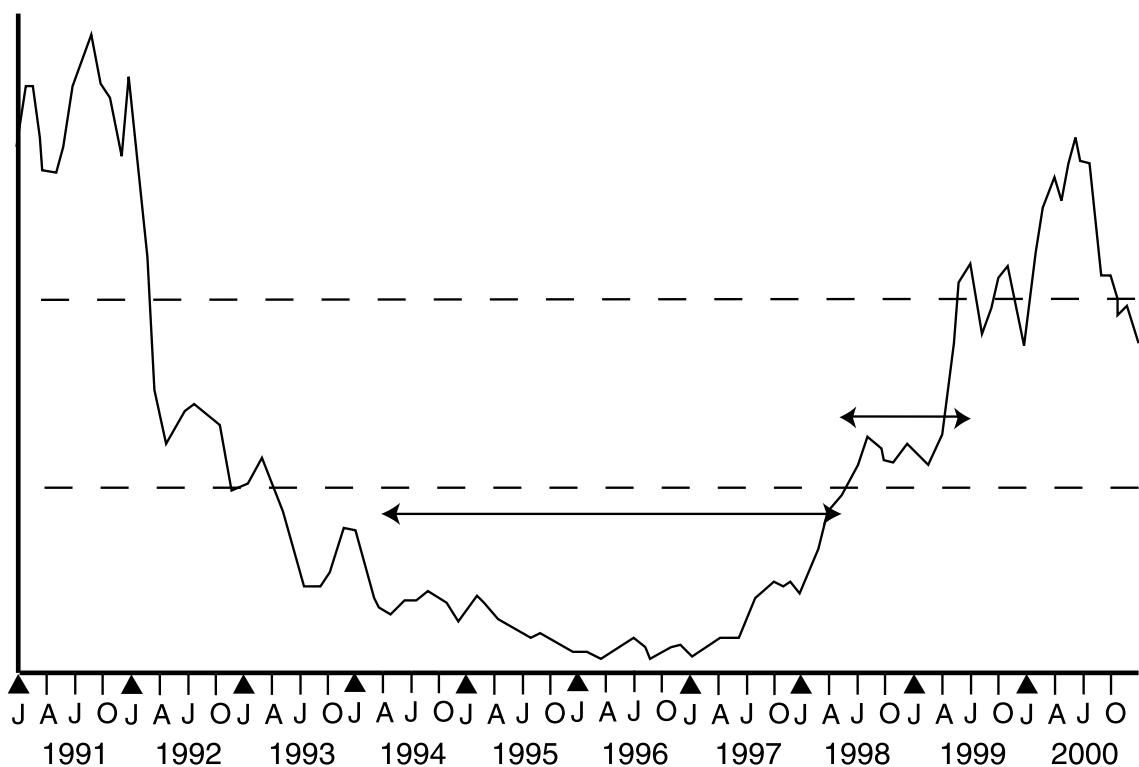


Figure 5.8: Solar activity, as defined and measured in Reference [102], as a function of time. The long arrow shows the period of this analysis modeled as solar minimum, and the shorter arrow is solar midcycle.

during the period of data-taking for this analysis. Using the divisions shown in the figure, we may model the period from the beginning of data-taking (April 1994) to April 1998 as solar minimum, and from April 1998 to the end of the dataset (June 1999) as solar midcycle. The first period has 77% of the minutes of data-taking, so 77% of the the Monte Carlo livetime is generated using the Bartol solar minimum flux, and the remainder using the Bartol solar midcycle flux. Because the interaction rate is slightly higher in the solar minimum epoch, 77.9% of the generated events are from that epoch to correspond to 77.0% of the generated livetime.

### Interaction Rate and Mass of MACRO

The subject of this analysis is neutrino events with vertices in the detector. To utilize the results of an event generator, consisting of a flux and a cross section model, the

event vertex must be placed randomly in the detector according to the probability of a neutrino interaction at each point. The cross section on electrons is negligible, so the interaction probability at a point depends on the density of protons and neutrons at that point. The cross section on neutrons is 75% higher than that on protons, so the  $Z/A$  ratio at the point is also relevant. If  $Z/A$  were constant across all the materials in MACRO, the interaction probability would be proportional to the mass density at each point. The detector consisted of a number of different materials – liquid scintillator, plastic scintillator tanks and streamer tubes, crushed rock absorber, and various shapes of steel, including structural I-beams and containers for the crushed rock.  $Z/A$  ranges from 0.466 in iron to 0.506 in liquid scintillator.

During construction the composition of MACRO was monitored closely – not with a mass calculation in mind but with energy loss calculations in mind – and the observations were incorporated into GMACRO, the detector simulation software. Scrutinizing the mass information implicit in the GMACRO geometry, I saw where uncertainties could significantly affect the result, and verified or updated the parameters, and even modified the GMACRO geometry slightly to conform with known masses of components. Then, the detector geometry as represented in GMACRO was used as the basis of both the event rate calculation and the random placement of event vertices.

At the end of initialization, the event generator considers the chosen flux and the calculated cross sections, and reports the interaction rate per neutron and per proton. (For Bartol solar minimum flux and Lipari cross section, the rates are  $0.20 \times 10^{-30}$  interactions per proton per second, and  $0.36 \times 10^{-30}$  interactions per neutron per second.) A generation volume enclosing the entire MACRO detector has been defined, and a million random points distributed uniformly in the generation volume are sampled. The Geant volume tree may be walked to determine in what material the point lies; however, because the MACRO geometry in GMACRO is defined with some overlapping volumes (for example, the volume containing structural iron between the two modules of Supermodule 1 overlaps with the volume containing all other Supermodule 1 materials), care has to be taken to be sure Geant does not report

the point is in air when it is really in structural iron or absorber. After sampling, the proportion of the generation volume occupied by each material is known. For each material, knowing the volume it occupies, its density, and its  $Z/A$  ratio, we may calculate the number of neutrons and protons, and thence the interaction rate, in that material. Summing over all materials gives the total interaction rate in MACRO.

Because the signature of neutrino-induced semi-contained muons requires an up-going muon to hit the center scintillator layer and a higher layer, almost all events detected by the analysis are generated in the lower part of MACRO. Table 5.1 shows the mass, as calculated using GMACRO, for the lower half of MACRO.

Medium	Volume (m <sup>3</sup> )	Density (g/cm <sup>3</sup> )	Mass (tonnes)
Crushed Rock Absorber	1490	2.17	3240
Iron	111	7.87	876
Scintillator	398	0.870	346
Plastic	135	1.63	220
Mineral Oil	20.6	0.870	18.0
Air	7410	$1.2 \times 10^{-3}$	8.93
Streamer Tube Gas	296	$1.0 \times 10^{-3}$	0.296
TOTAL			4709

Table 5.1: Masses of components of lower MACRO.

The above calculations all take place during program initialization. Later, during the event loop, the generated neutrino interactions must be placed in MACRO according to the interaction probability at each point. The generator uses a Monte Carlo rejection algorithm: the interaction vertex is placed at a random point in the generation volume with uniform probability, Geant then walks the volume tree to determine in what material the point exists, and then the choice of location is accepted with probability equal to the ratio of the interaction probability in that material to the maximum interaction probability in any material (iron), taking the density and  $Z/A$  into account. If the vertex is not accepted, another is generated, repeating until one is accepted.

## The Generated Dataset

The generator utilizes neutrinos from all directions (downgoing as well as upgoing) with interaction vertices in a generation volume that contains the entire detector (attico as well as lower MACRO). The generator calculates the event rate at solar minimum, taking into account the mass and Z/A ratio of the actual material in the generation volume, as 886 events/year for  $\nu_\mu + \bar{\nu}_\mu$ , and 452 events/year for  $\nu_e + \bar{\nu}_e$  (not considering oscillations). For solar midcycle, the interaction rates are about 4% lower. The generated dataset consists of 100,000  $\nu_\mu$  and  $\bar{\nu}_\mu$  events (77,527 with the solar minimum spectrum and 22,473 at solar midcycle) and 50,344  $\nu_e$  and  $\bar{\nu}_e$  events (39,516 minimum and 10,828 midcycle), both corresponding to 88 years at solar minimum and 25 years at solar midcycle, a total of 113 years.

Two other generators are used to check for backgrounds. Simulated downgoing atmospheric muons are checked to see if they pass all the cuts and appear to be semi-contained neutrino events. However, the 100,000 generated events correspond to a simulated livetime of less than a half week.

Upgoing muons due to neutrino interactions below the detector are used to estimate the rate of throughgoing upward muons that inadvertently pass the containment cut, thus appearing to be semi-contained. The 100,000 generated events correspond to a livetime of 143.5 years.

## 5.3 Analysis Chain

### 5.3.1 Preparing the Data for Analysis

First a DASH module called **badFilt** applies the microcuts for scintillator quality (see Section 3.2); if an ERP box that fired in the event is marked as bad for the week in which the event occurs, that box is deleted from the event record so subsequent analysis behaves as if the box did not fire. Likewise, if boxes on two supermodules fired and the interERP reconstructions for that pair of boxes are marked as bad for that week, interERP TDC information is deleted from the event record, in such a way that

it will be impossible to reconstruct the timing. In this way, even if equipment marked for a microcut fired during the event, the event may still be accepted if the remaining equipment is adequate to mark the event unambiguously as neutrino-induced.

Next, all ERP reconstructions (see Section 2.3.1) are computed and stored in the event record by the DASH module **recal**. Then, if ERP channels fired on more than one supermodule, an attempt is made to adjust the timing in all hit ERPs so that their relative timing is correct, utilizing the information in the interERP TDCs. The DASH module **ierpAdj** uses the procedures detailed in Section 2.3.1 to adjust all hit boxes in an event to be mutually consistent, if possible. If it is not possible (either because the combination of hit supermodules is intrinsically unadjustable, or because of missing or bad data (underflow or overflow) in the interERP TDCs), the event is rejected at this stage.

By this point in the analysis chain, any event not rejected contains only good boxes with the relative timing reconstructed for all scintillator hits. In the real data, 97.6% of all events survive to this stage; most of those cut are interERP events in which the interERP pair is marked for a microcut (see Section 3.2).

### 5.3.2 Identifying the Best Candidate Track

Now that data has been prepared, to search for neutrino-induced muons the first step is to use reconstructed streamer tube tracks to identify candidate space tracks. As in the standard muon analysis (described in Section 3.1), any event that does not have a viable candidate track is rejected and not processed further. It would be possible to use the generic track finder from the standard muon analysis, and then reject the event if the candidate track chosen does not have the proper topology (recall that this analysis requires scintillator hits in the Center layer and a higher layer). However, to increase efficiency slightly, a customized track finding module, called **scTrack**, was developed. **scTrack** only chooses candidates with the proper topology. Thus, in an event in which one candidate track (perhaps due to an ongoing neutrino-induced muon) has the right topology and one candidate track (perhaps due

to a recoiling pion) has the wrong topology, we can be assured that the track with the right topology will be chosen and the event will not be rejected at this stage.

**scTrack** begins by iterating over every possible pair of reconstructed streamer tube tracks in different views – that is, wire and strip views, wire and lateral views, or strip and lateral views. For each pair, it computes the space track in three dimensions, and then identifies any fired scintillator boxes that are near the track. The position of the scintillator hit is determined by using the scintillator timing to find the coordinate along the box (as described in Section 2.3.1), and the coordinates of the center of the box in the other two dimensions. The shortest distance from the scintillator hit to the space track is computed, and if it is within 75 cm, the hit is considered associated with the track. Figure 5.9 illustrates these concepts. If the space track can be associated with a scintillator hit in the Center layer and another scintillator hit in the attico, the track is considered a candidate. If more than one hit in the Center layer could be associated, the one nearest the track is chosen; likewise the closest attico hit is chosen. Thus, a candidate consists of one space track, one Center hit and one attico hit. Because the wire and strip tracking require four hits to reconstruct a track, this algorithm cannot find muons that traversed fewer than four of the horizontal streamer tube planes.

If no candidate space track is found by iterating over pairs of tracks, **scTrack** attempts to invoke an algorithm called “combined tracking” (or, more informally, “Spurio tracking,” after the name of the MACRO collaborator who developed the algorithm). The combined tracking algorithm uses a single lateral track, in the Y-Z view. Recall (see Section 2.2) that lateral tracks may contain, in addition to hits in the lateral view, combined wire-strip hits that lie along the track in the Y-Z view. Combined tracking utilizes the X and D information from these central hits to reconstruct a track in three dimensions that passes through all the hits. Combined tracking can be successful for muons that crossed as few as two horizontal planes (plus some lateral planes), so it is more efficient for near-horizontal muons than the standard tracking.

For most events in the dataset, whether downgoing atmospheric muons or

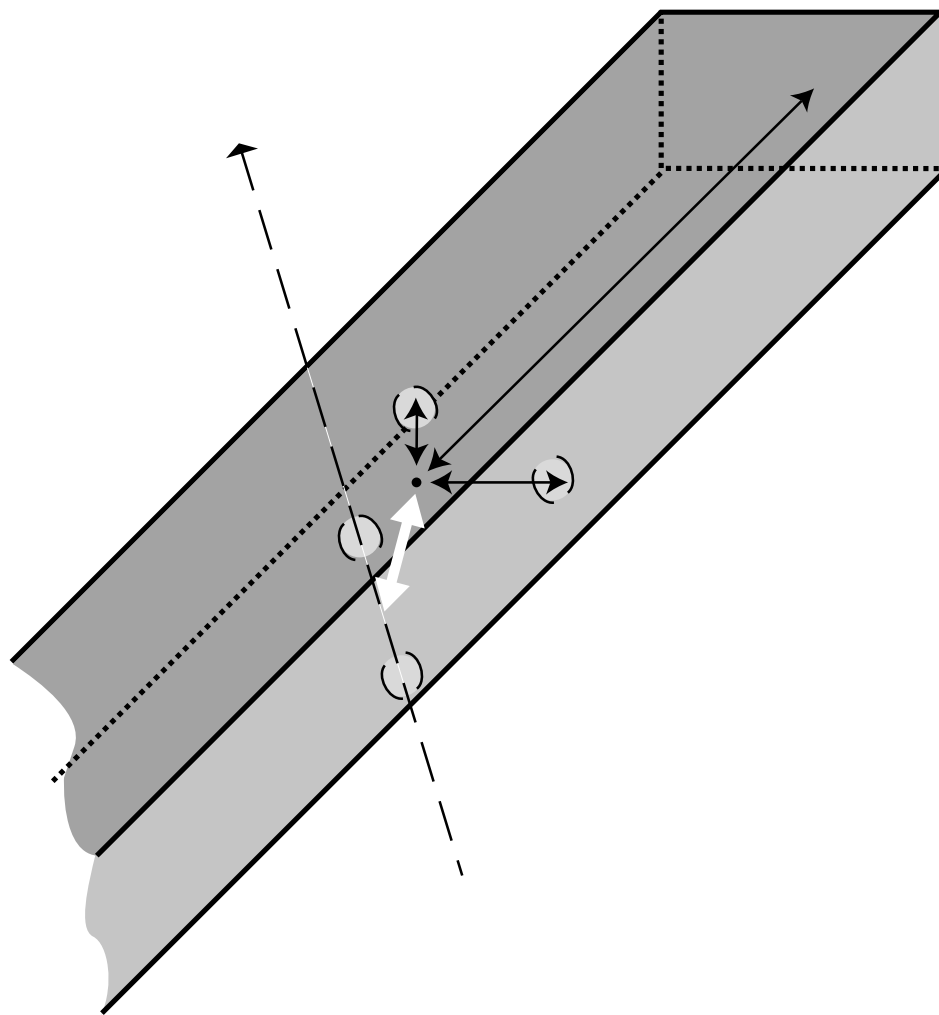


Figure 5.9: A scintillator hit and a space track. The coordinates of the hit are taken to be the center of the box in the two short dimensions, and given by the scintillator timing along the long axis of the box. The solid black arrows indicate the coordinates of the hit. The dashed line is a nearby space track. The white arrow shows the distance from the hit to the space track, at the point of the track’s closest approach to the hit.

neutrino-induced muons or something else, there is at most one candidate track. However, if more than one candidate exists, **scTrack** will choose the “best” track to be processed as the candidate by the remaining modules in the analysis chain. If there are one or more “quality” tracks (defined as a track for which the average of the squared distance from the two scintillator hits to the track is less than  $(50 \text{ cm})^2$ ), the quality track whose time of flight between the two scintillator hits is closest to that

expected for an upgoing relativistic particle is chosen. In this way, if there are upgoing and downgoing candidates, an upgoing candidate will be chosen. If no quality tracks exist, the candidate is chosen that has the lowest average of the squared distance to the track. Information about the chosen candidate is placed on the FARFALLA tree, and is available to all subsequent modules.

In the real data (which includes triggers for other physics processes in addition to downgoing muons), a candidate track is identified for about 1/3 of all events. For simulated downgoing muons, 55% have the right topology to pass this requirement. For simulated neutrino interactions in the detector (including both  $\nu_\mu$  and  $\nu_e$ , and both charged current and neutral current interactions), only 6.4% have a candidate track. Most of the rest range out in the absorber without hitting any scintillators, or they go the wrong direction to hit the Center layer and an attico layer.

### 5.3.3 Containment

At this point the remaining events are generally muons that traversed at least part of the lower detector, the C layer, and a higher scintillator tank. However, the vast majority of these events are throughgoing events. It is necessary to identify a subset of the remaining events that appeared to have their track start (or, in the case of downward muons, end) within the interior of MACRO. This is determined by requiring that the candidate space track hit several channels that did not fire, all below the lowest channel that did fire. This eliminates particles that entered or exited via a lower face of the detector, as well as particles that entered or exited through a known crack in the detector.

A DASH module, **scCrack**, was developed to identify such events. For the candidate space track, a list is generated of the streamer tube channels (defined as a collection of eight wires, about 25 cm wide) and scintillation counters intersected by the track, and it is determined if the hit channels fired in the event. If a channel that is hit but did not fire is in the database of dead channels for the moment the event occurred (see Section 3.3), the hit is deleted from the list and the algorithm proceeds

as if the track did not hit that channel. The lowest fired channel defines the bottom of the track. A hit channel that did not fire may be below the track or within the track.

**scCrack** then implements the logic defining the containment cut. The logic was developed primarily by looking at stopping downward muons in the real data. It became clear that lateral streamer tube channels are unreliable for a containment cut. There were many gaps between streamer tube channels in the lateral walls, and if the actual path of a muon differed slightly from the reconstructed space track, it often happens that the software considers a channel hit when in fact it was slightly missed. Therefore, **scCrack** considers a fired lateral channel on the track to be evidence that the vertex was not contained, but an unfired lateral channel is not considered to be evidence that the vertex was contained. Also, while it is sensible to insist that, to consider a vertex contained, a hit scintillator counter below the track did not fire, in practice it is seen that adding this requirement eliminates very few events that are not eliminated by considering streamer tube information alone. In fact, in the final sample of selected neutrino events, there are no fired scintillators below the track. Therefore the containment logic does not consider the scintillator counter, so that certain uncertainties in the simulation (for example, for slow neutrons that trigger a scintillator far below the vertex) cannot affect the Monte Carlo rate prediction.

Therefore, the final containment logic is quite simple: that two live horizontal streamer tube channels below the track be hit but not fired. Note that if the track extends downward through a lateral wall, and a channel in the lateral wall did fire, the event is not considered contained by this definition because any missing horizontal channels are not below the track. See Figure 5.10 for examples of events passing or not passing the containment cut.

Note that true neutrino interactions near a wall or a crack may not pass the containment cut (nor may stopping muons that stop near a wall or a crack). This cut is similar in spirit to a “fiducial volume” cut in other experiments, although the cut is defined by topology rather than volume. The simulation should predict the rate of interactions passing the cut, as well as true signal events that do not pass the cut.

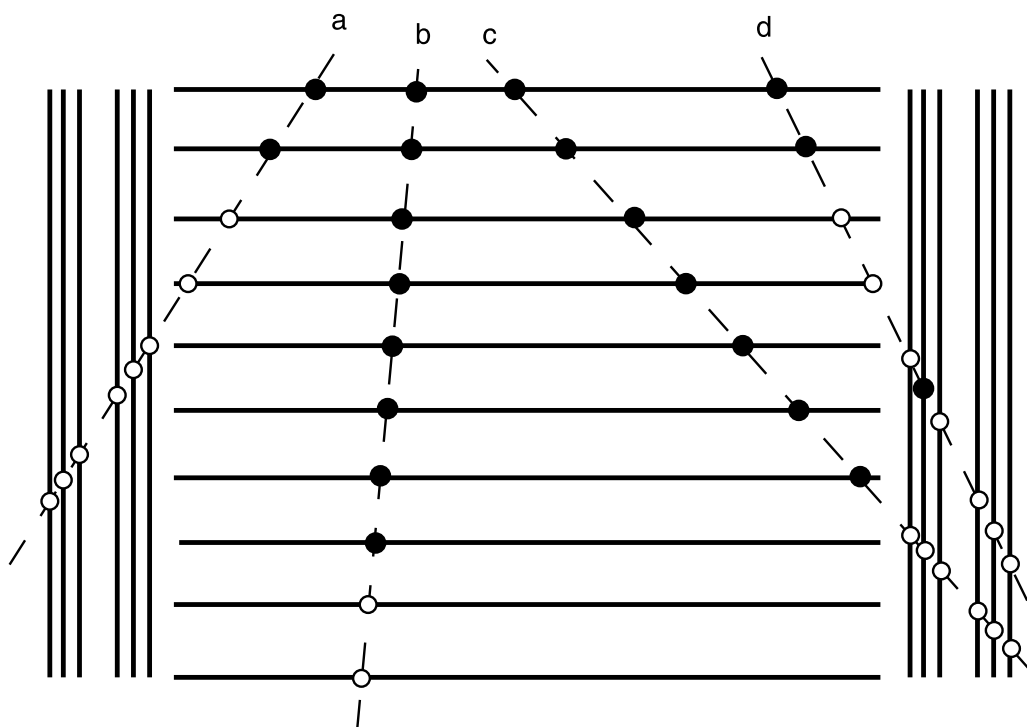


Figure 5.10: How the containment cut works. The dashed line shows the space track, filled circles represent hit channels that fired, and open circles represent hit channels that did not fire. (a) and (b) pass the containment cut because two central channels below the track were hit but did not fire. (c) does not pass the containment cut. Although several lateral channels below the track were hit but did not fire, lateral channels are not considered reliable enough to provide confidence that this event is really contained. (d) does not pass the containment cut. Although the bottom two hit central channels did not fire, they are not below the track due to the lateral channel that did fire.

In the real data (mostly downward throughgoing muons), only 1.4% of events with a candidate track pass the containment cut. For simulated neutrino interactions, 85.7% pass.

For each event selected at the end of the analysis, certain streamer tubes that failed to fire led to the event being declared semi-contained. Let us call these “critical channels.” A final check shows that the critical channels were indeed alive and functioning. Figure 5.11 shows, for each critical channel in each event in the final sample, the last time the channel fired before the event, and the first time the channel fired after the event. The distribution has the expected exponential shape, and there is no

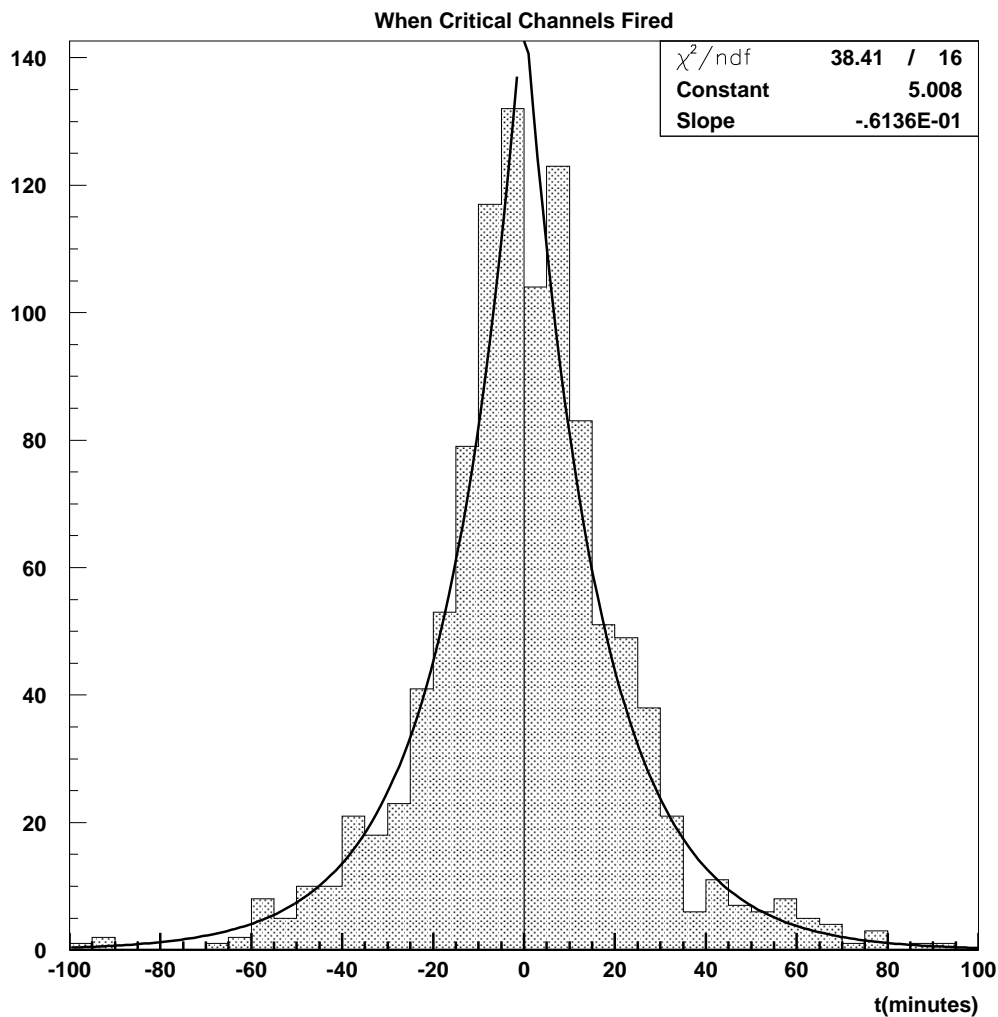


Figure 5.11: Timing in critical channels. The entries at negative time show how many minutes before the event the channel last fired, while the positive entries show how many minutes after the event the channel next fired.

evidence that any of the tubes were experiencing any problems firing.

### 5.3.4 First Background-Reducing Cuts

The vast majority of candidates identified by the above procedure are correctly measured. However, there are hundreds of thousands of downgoing atmospheric muons

for each neutrino-induced muon identified by this analysis, so even a tiny fraction of mismeasured events could overwhelm the signal. Therefore, it is necessary to apply a number of cuts to reject any events that may mismeasure the direction of the particle.

The cuts applied at this point can choose either upgoing or downgoing particles. The first cut requires that the values recorded by the TDCs of the boxes on the track are within the normal valid range – between 1000 and 4050 counts. The second cut requires the time reconstructed by high-threshold and low-threshold TDCs agree within 10 ns for each of the two boxes. Only a fraction of a percent of real events fail these two cuts. The third cut requires the two scintillator hits to be at least 300 cm apart, so a mistake of 20 ns would be required to turn a downgoing relativistic particle into upgoing. This cut eliminates over 10% of all candidates, but it also eliminates the majority of mistimed events at negative  $\beta$ . Figure 5.12 shows the effect of these cuts on the distribution of  $1/\beta$ . (Recall that for fixed pathlength, the error in  $1/\beta$  is proportional to the error in the measured time of flight.) After these cuts, 275,606 events remain, 436 of them upgoing, and a clear signal peak is emerging at  $\beta = -1$ . However, there is still obviously a large background from mistimed events. The precision of the measurement can be improved by making additional efforts to reduce background.

### 5.3.5 Further Background Suppression Methods

Seven different additional cuts, which will be referred to as “optional cuts,” have been developed and tested. All the previous cuts were capable of being passed by either downgoing or upgoing particles; however, much of the remaining background at negative  $\beta$  is initiated by downgoing particles. A downgoing particle may create backscattered upgoing particles in the detector by photonuclear interactions or other processes; a bundle of 2 or more muons that originated from the same high energy primary cosmic ray may arrive at different times in such a way as to mimic upgoing timing; or particles that initiate large electromagnetic showers in or near the detector may cause several particles to enter one box at different times and places, making

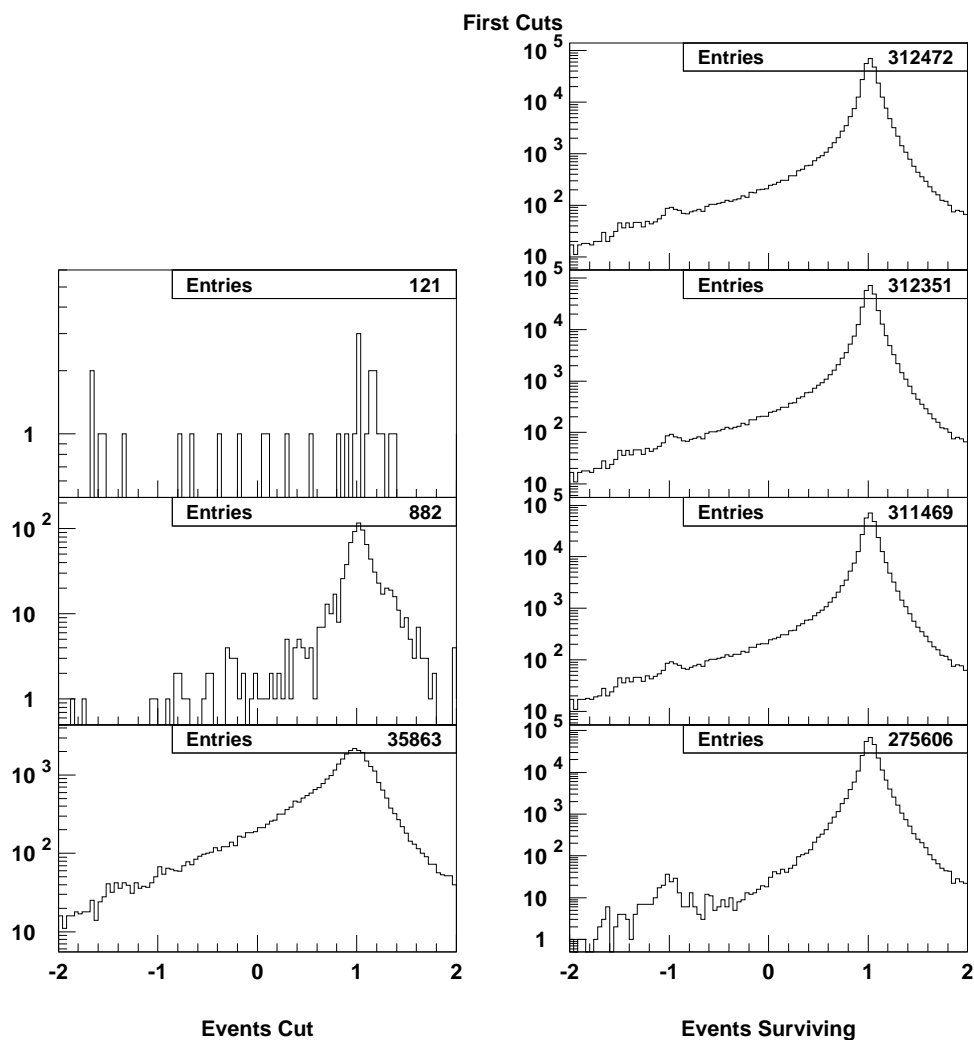


Figure 5.12: The effect of the first background-reducing cuts. The top graph shows the  $1/\beta$  distribution of all semi-contained events before cuts. For each of the three cuts, the left column shows events eliminated by the cut and the right column shows events surviving the cut. The three cuts are, from top to bottom, Valid TDCs, TDCH-TDCL Agreement, and Pathlength.

the timing and position reconstructions unreliable. Therefore, many of the following cuts will reject an event if there is any indication of a downgoing particle; thus, the analysis is no longer up-down symmetric.

EARLIER FACE CUT: Generally one expects the earliest scintillator hit on the

candidate track to be the earliest hit in the event; if not, it could be because one or more boxes are mistimed. However, often nearby hits in the same face as the earliest hit on the track are a few nanoseconds earlier. This cut rejects the event if there is an earlier scintillator hit (off the track) in a different face than the earliest hit on the track. This cut is up-down symmetric. It incurs some inefficiency for real neutrino events because a secondary may hit a lower box before the muon reaches the Center layer.

CLUSTER CONSISTENCY CUT: Usually a group of scintillator hits near each other in space are within a few nanoseconds of each other in time; if not, it could be because one or more boxes are mistimed. This cut rejects the event if there is a scintillator hit within 250 cm of a hit on the candidate track which differs by more than 10 ns in time. This cut is up-down symmetric. It incurs some inefficiency for real neutrino events because a slow particle from the vertex or a secondary particle created elsewhere may hit a nearby box at late times.

ERP MULTIPLICITY CUT: Large showering events, which often have inaccurate timing in some boxes, usually cause triggers in several ERP boxes. This cut rejects the event if there are four or more fired scintillator boxes not intercepted by the track. Although only two boxes are officially associated with the candidate track, any other boxes hit by the track are not counted toward the number of hits off the track. This cut is up-down symmetric. It incurs some inefficiency for real neutrino events because high energy neutrino events can have a high multiplicity of secondary particles moving in different directions.

NO DOWNGOING TRACK CUT: Sometimes a downgoing muon in the detector creates an upgoing secondary. This cut checks all candidate tracks other than the chosen candidate, and rejects the event if any candidate has associated scintillator hits with downgoing time of flight measurements.

LEAST SQUARES FLOW CUT: This cut determines parameters  $a$  and  $b$  for the equation  $t = az + b$  by minimizing the squared error over the set of all  $(z, t)$  coordinates, one coordinate for every ERP hit. This cut rejects the event if  $a$  is negative, which indicates the general flow of the event is downgoing.

MAJORITY OF PAIRS UPGOING CUT: For every pair of ERP hits, if they are at different heights, it is determined if the pair timing is upgoing or downgoing. This cut rejects the event if half or more of the pairs are downgoing.

ALL PAIRS UPGOING CUT: This cut rejects the event if even one pair of ERP hits has a non-tachyonic downgoing time of flight. However, it is less strict than the previous cut in determining the pair to be downgoing: it will not count a pair as downgoing if the time difference is small, or if it is less than the amount of time needed to connect the two hits at the speed of light. Thus, for events with ambiguous timing, it is possible to pass this cut and fail the Majority of Pairs Upgoing Cut. It incurs some inefficiency for real neutrino events because events with an upgoing muon may have other downgoing secondaries.

Figure 5.13 shows the effect of each cut individually, as well as the effect of requiring events to pass all seven optional cuts.

An investigation was made to discern if any particular combination of optional cuts could optimize signal and background in such a way as to reduce the statistical uncertainty of the neutrino flux measurement. Two kinds of background must be considered. First, there are events for which the time of flight is mismeasured, either due to transient hardware failure or unusual conditions in the scintillator box. For these events, there is no preference for  $\beta = -1$ . One can estimate the background in the  $\beta = -1$  peak by looking at the distribution of events off-peak. Figure 5.14 shows the distribution of  $1/\beta$  for all events passing all the non-optional cuts with none of the optional cuts applied. It is clear that there is a significant signal near  $\beta = -1$ , but with a large background due to mistimed events. The distribution of off-peak events is skewed in the direction of  $\beta = +1$  which suggests they are the (badly-measured) tail of the downgoing muons distribution. If we define the signal region to be  $-1.2 < 1/\beta < -0.8$  (chosen by looking at Monte Carlo events, as described in the next section), we may estimate the background in the signal region utilizing a fit to the background events outside the signal region. In the figure, a linear fit is used which has no motivation other than phenomenological.

For Poisson-distributed signal and background processes, if we estimate the signal

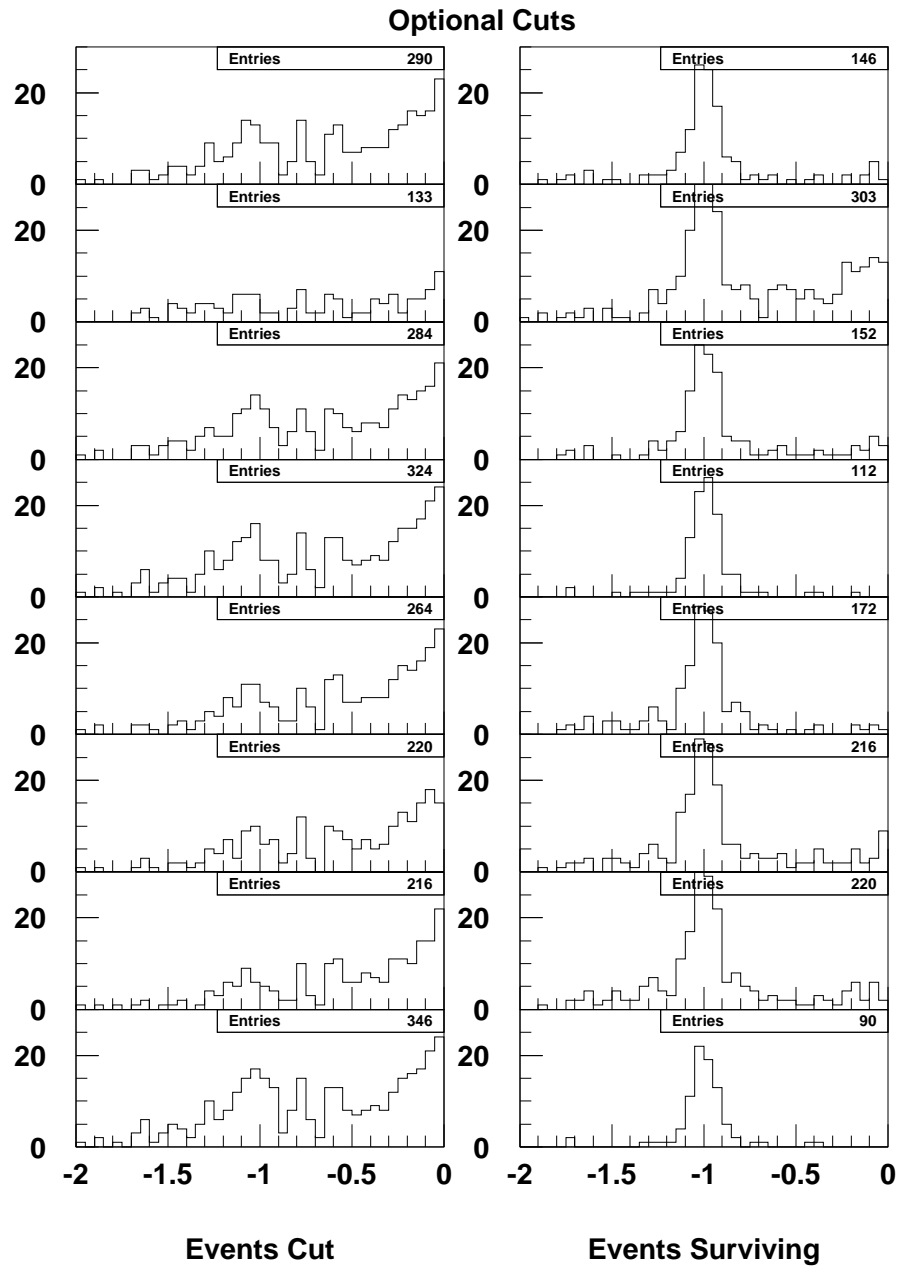


Figure 5.13: The effect of each cut individually on the 436 upcoming candidates; the cuts are not cumulative in these graphs. The first seven rows are, from top to bottom, the optional cuts in the order described in the text. The bottom pair shows the effect of requiring events to pass all seven optional cuts.

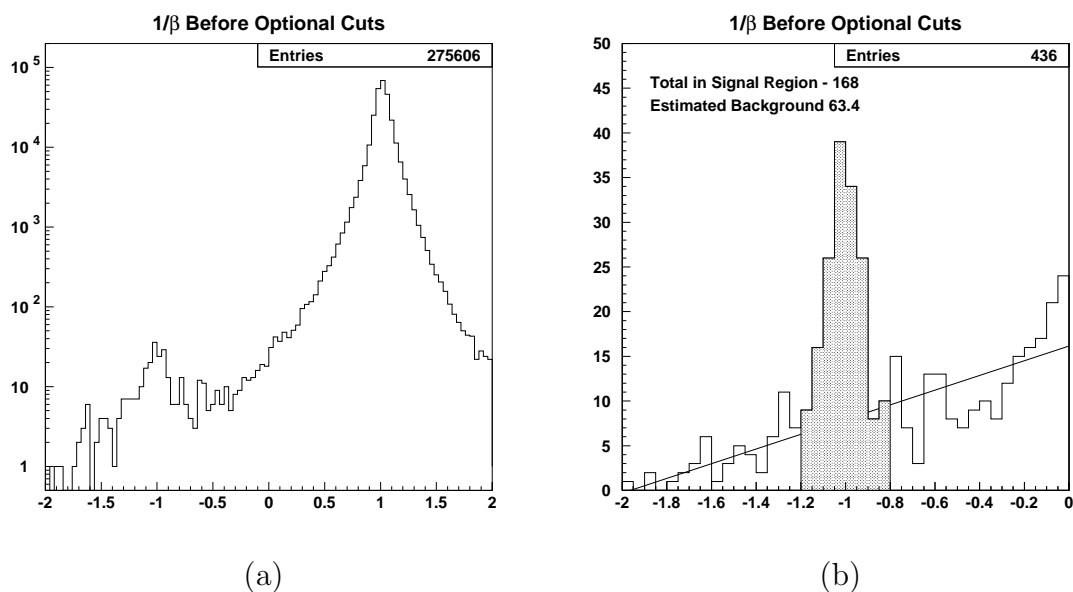


Figure 5.14:  $1/\beta$  distribution for events passing all the non-optional cuts. (a) shows upgoing and downgoing events on a logarithmic scale while (b) shows only upgoing events on a linear scale. The linear fit uses the off-peak regions to estimate the background in the signal region.

$\tilde{S}$  to be the total events  $T$  (in the signal region) minus the expected average  $\bar{B}$  of the background distribution, the fractional error ( $\sigma/\mu$ ) in the determination of signal is  $\sqrt{T}/(T - \bar{B})$ . If we restrict ourselves to insisting the events pass some definite combination of cuts, there are 128 possible combinations of the 7 cuts, ranging from none of the cuts, to just the first cut, through various combinations, finally to applying all 7. We may apply the linear background fit to the  $1/\beta$  distribution of events passing each combination of cuts and compute the fractional precision with which the non-mistimed  $\beta = -1$  signal may be determined. (Actually, the pure signal events in the Monte Carlo have some probability to produce a measured  $\beta$  outside the signal region, so the livetime-adjusted number of Monte Carlo events in the sidebands is subtracted from the real data events in the sidebands before doing the linear fit.) When this prescription is applied, the fractional error ranges over a surprisingly small range, from 10.1% up to 11.6%, as the estimated signal (which is legitimately different

depending on the cuts) ranges from 76 events up to 111 events. Thus, neither a loose set of cuts (which provides more signal) nor a tight set of cuts (which produces less mistimed background) enjoys much statistical advantage over the other.

Then, a second type of background must be considered – true upgoing relativistic particles which are not neutrino-induced (which, in MACRO, are therefore almost certainly induced by downgoing muons). This background cannot be estimated by looking outside the  $\beta = -1$  peak because it truly has  $\beta = -1$ . As stricter cuts are applied, the true signal will be decreased, and the Monte Carlo sample, which consists of 100% signal events, will be increasingly rejected. Ideally, if all backgrounds had been eliminated by earlier processing and the Monte Carlo correctly simulated the chance of signal passing each cut, the estimated signal in real data would be proportional to the number of events passing the cuts in Monte Carlo for whatever set of cuts is chosen. Figure 5.15 shows a scatter plot, for each of the 128 combinations of optional cuts, of the data signal, plotted versus the predicted signal from the Monte Carlo. It is seen that the ratio tends to be larger for looser cuts (i.e., cuts that produce a larger predicted signal). This suggests that the loose cuts are retaining some upgoing background in addition to signal.

Therefore, it appears that to eliminate as much of the  $\beta = -1$  background as possible, it is prudent to utilize all the optional cuts. This will also reduce signal, but it was shown above that because the mistimed background is also reduced, we pay a small price in statistical error by cutting hard.

## 5.4 Results

### 5.4.1 The Selected Events

Figure 5.14 above shows the  $1/\beta$  distribution for events passing all non-optional cuts, including the containment cut, but no optional cuts. The vast majority are downward events ( $\beta = +1$ ) stopping in the detector, while a few events are badly mismeasured, and a signal of neutrino-induced events at  $\beta = -1$  is clearly visible. Figure 5.16

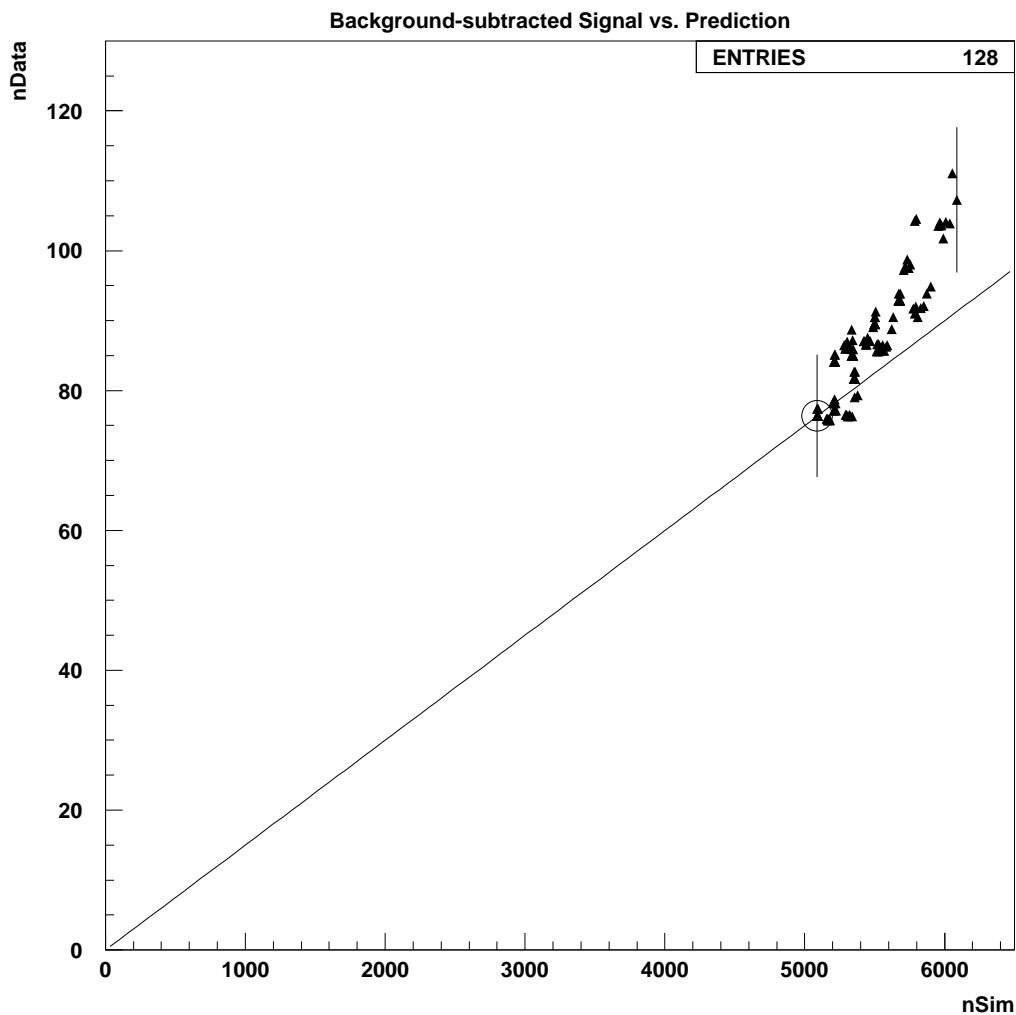


Figure 5.15: Scatterplot of the different possible combinations of 7 optional cuts. Each point represents one possible set of cuts (for example, one point represents all events passing cuts 1, 3, and 7). For each of 128 possible combinations, the estimated background-subtracted signal seen in the real data is plotted against the predicted signal from the simulation (arbitrarily scaled). Poisson errors on the data are shown on the first and last points. The combination of cuts used in this analysis, in which all 7 optional cuts are applied, is circled.

shows that the mistimed background is cleaned up in the negative  $\beta$  sector by the application of all seven optional cuts. Within the signal range of  $-1.2 < 1/\beta < -0.8$ , 77 events are found.

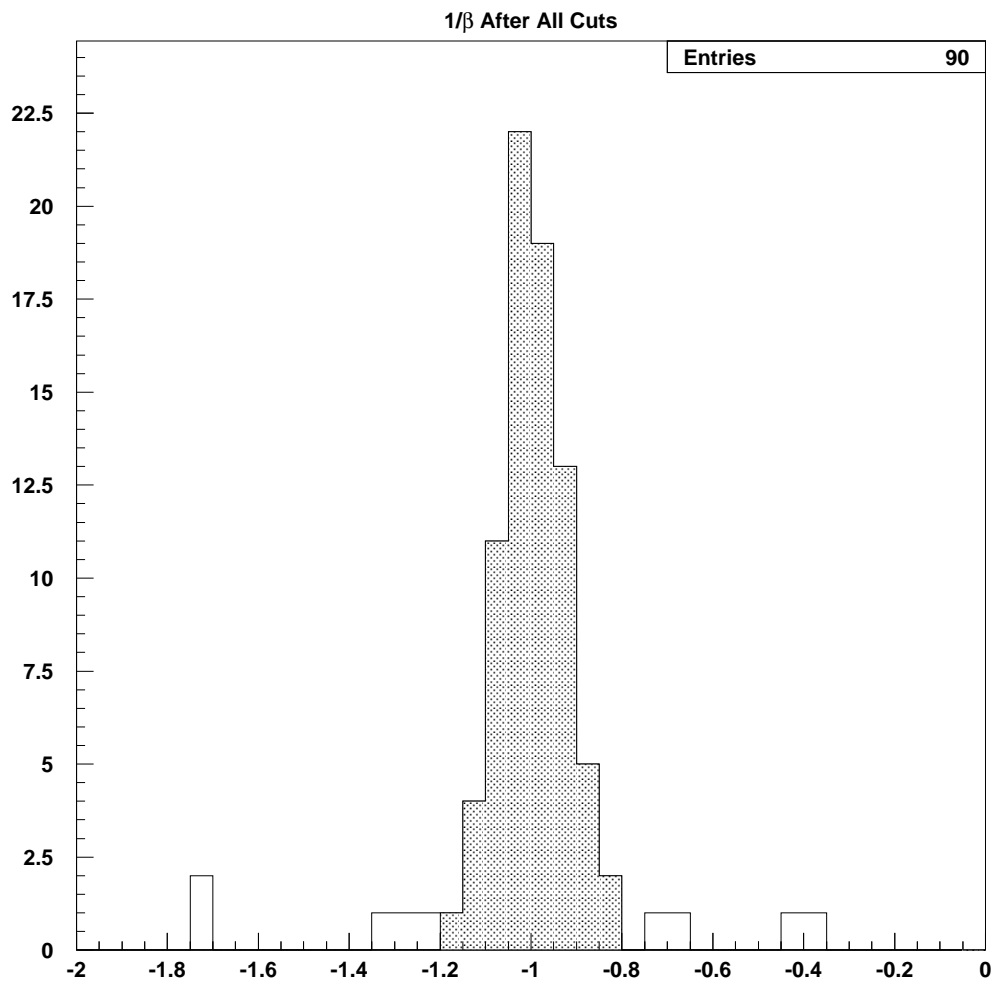


Figure 5.16: The final  $1/\beta$  distribution. The signal region, containing 77 events, is shaded.

### 5.4.2 The Monte Carlo Prediction

Following the same analysis path as real data, the simulated data for 113 years of nominal detector operation yielded 5460 events passing all cuts including all optional cuts (neglecting the effect of neutrino oscillations).

For each real data run, we could define the livetime for that run as the time from the first event recorded in the run until the last event. Summing this time over

all the runs in the dataset yields 2,346,699 minutes (4.5 yr). However, not all of these minutes are equivalent. During some of them MACRO was not in its nominal configuration. For example, sometimes one or more entire supermodules were turned off. In the earliest runs in the dataset, the attico streamer tubes were not all installed and working. Other times, even if all the supermodules were in acquisition, some small parts of the detector were dead or not fully efficient. Often one scintillator tank would be turned off due to hardware problems, sometimes for weeks or months at a time. At times the streamer tube gas mixture was not well-controlled, and the strip efficiency declined precipitously. For all of these reasons, it is necessary for the Monte Carlo calculation of the expectation to have a way of accounting for the effects of MACRO not being always in a full, nominally-functioning configuration.

To incorporate the effects of the known dead channels and inefficiencies into the Monte Carlo calculation, the database of channel dead periods and channel efficiencies (see Section 3.3) is used. The entire dataset of simulated events is passed through 262 different simulations, one for each week analyzed. For each Monte Carlo event to be analyzed, a clock time is chosen randomly, between the time the first event of the week occurred and the time of the last event of the week. If the time chosen is not during a run in the dataset (that is, it is between runs), the time is rejected and another chosen. Any channels that were dead at the chosen time are eliminated from the event record before analysis proceeds, and any channels that were not dead at that minute are probabilistically eliminated from the event record according to their efficiencies stored in the database. Next, a decision is made probabilistically to eliminate all channels in a microvax according to the measured average computer deadtime stored in the database for that microvax for that week. The algorithm assumes maximum correlation between the microvax dead periods; that is, if the event involves channels from two microvaxes and one microvax is chosen to be dead, the other microvax will also be chosen to be dead as often as possible, consistent with the difference of deadtimes between the two microvaxes. Finally, any channel that would have been eliminated from the real data at that time by a microcut (see Section 3.2) is eliminated from the simulated data as well. After this process, the

event is analyzed based on the channels that have not been eliminated. The resulting event may or may not pass all cuts.

For each Monte Carlo event, if it passes all cuts in the simulation for a given week, it is recorded to have a weight for that week equal to the number of minutes of actual data-taking that week, divided by the number of simulated minutes in the Monte Carlo generation. If it does not pass the simulation, its weight for the week is zero. Summing the weight for the event over all 262 weeks gives its total weight. If the detector had been nominal at all times, the same events would pass each week and the summed weight for all events would be equal to the ratio between the total real livetime and the length of time in the simulated generation. The Monte Carlo prediction for the number of events in the bins of any histogram would be the number of Monte Carlo events in the bin, multiplied by the ratio of the real livetime to the simulated generation time. The effect of the recorded non-ideal performance of the real detector is indicated by the difference between the actual summed weight for each Monte Carlo event and the ideal summed weight. The Monte Carlo prediction for the bins of any histogram is the sum of the weights of all simulated events in that bin. Figure 5.17 shows, for example, the  $1/\beta$  distribution for the real and ideal detectors. The simulated effect of the non-ideal performance is a reduction of 15.0% in the predicted event rate in the signal region  $-1.2 < 1/\beta < -0.8$ .

For the non-ideal detector, Table 5.2 shows several properties of the simulated events passing all cuts, both assuming no oscillations and assuming oscillations at a test point of  $\sin^2 2\theta = 1$ ,  $\Delta m^2 = 3.2 \times 10^{-2} \text{ eV}^2$ . The question of what this analysis has to say about oscillation parameters will be taken up in Chapter 6.

### 5.4.3 Comparison of the Measurement and the Prediction

Figure 5.18 shows a comparison of the measurement and the prediction, with and without oscillations, before applying any corrections or statistical and systematic errors. It is immediately evident that the data favor the hypothesis of oscillations. The significance of this assertion will be explored in the next chapter, Interpretation.

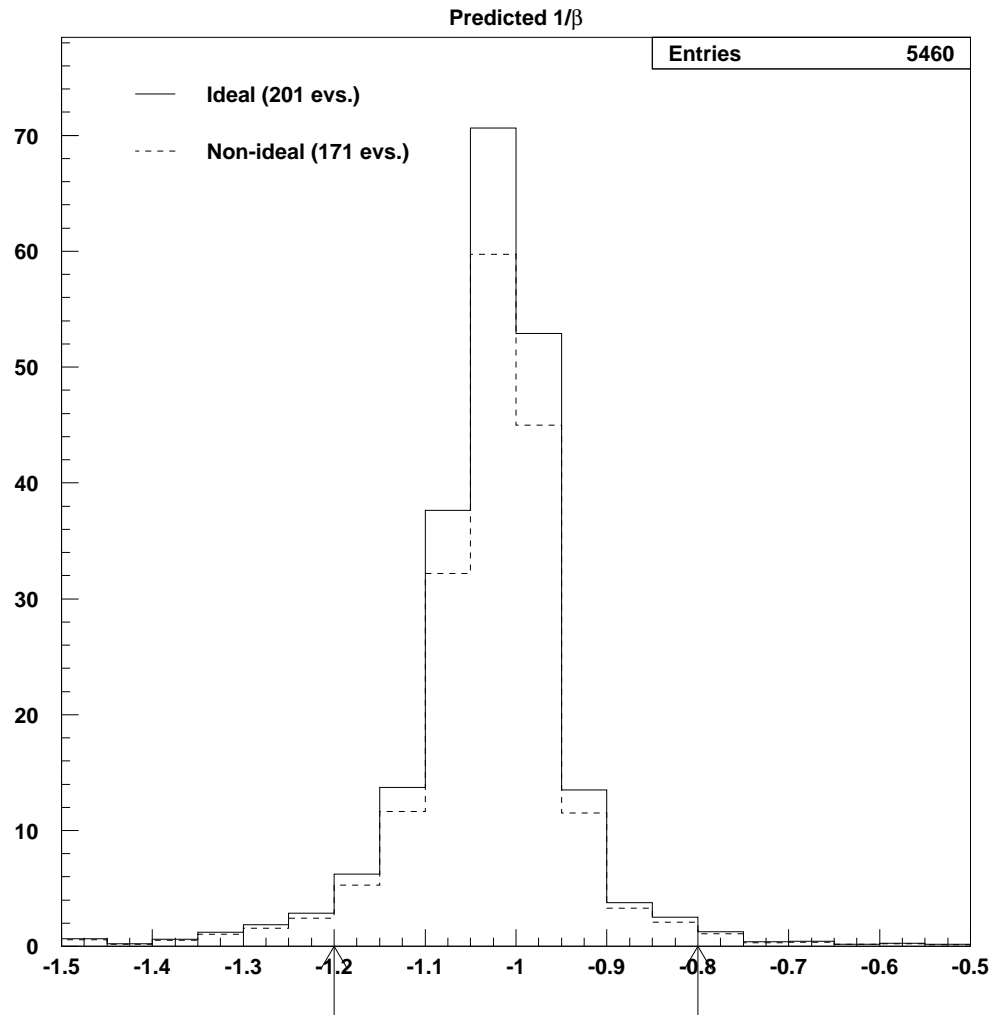


Figure 5.17: The predicted  $1/\beta$  distribution (neglecting oscillations) for the ideal detector (solid line) and for the non-ideal detector as simulated.

	No Oscillations	Oscillations
Total	170.8	96.3
$\nu_\mu$	108.2	57.6
$\bar{\nu}_\mu$	49.6	25.7
$\nu_e$	10.3	10.3
$\bar{\nu}_e$	2.7	2.7
$\nu_\mu + \bar{\nu}_\mu$ CC	154.9	80.4
$\nu_\mu + \bar{\nu}_\mu$ NC	2.9	2.9
$\nu_e + \bar{\nu}_e$ CC	11.9	11.9
$\nu_e + \bar{\nu}_e$ NC	1.1	1.1
p	67.8	37.8
n	102.9	58.5
Absorber	122.8	68.0
Iron	31.8	18.1
Scintillator	10.9	7.0

Table 5.2: Properties of simulated events passing the analysis. The first four rows show the particle interacting, the next four, the type of interaction, the next two, whether the interaction was with a proton or a neutron, and the last three, in what material in MACRO the interaction occurred. Several materials in MACRO are not listed.

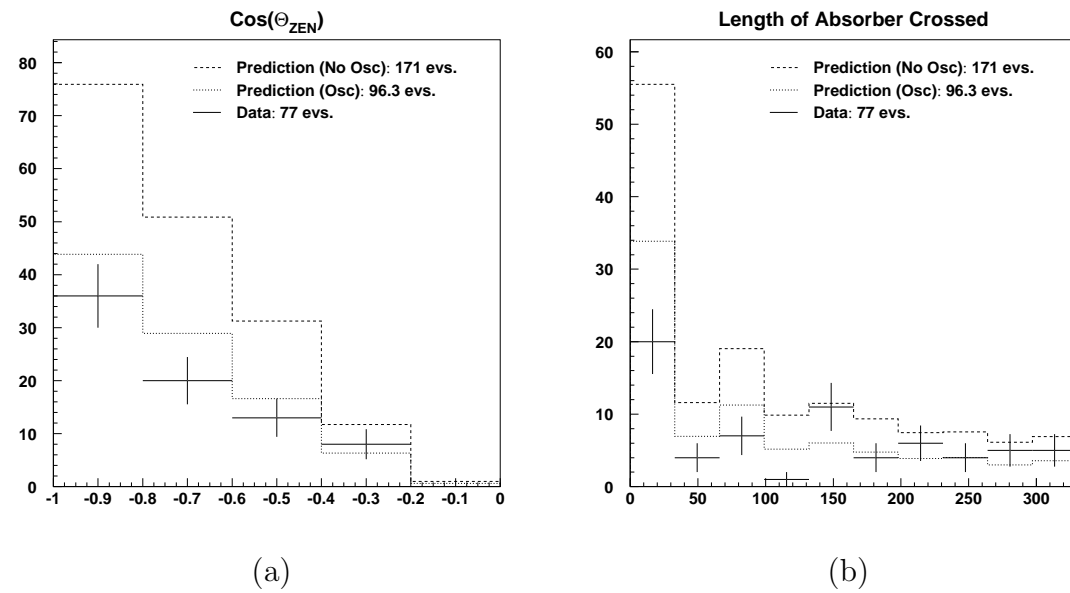


Figure 5.18: The selected real data events, plotted as a function of two variables, and compared to the Monte Carlo prediction, with and without oscillations. (a)  $\cos(\theta_{zen})$  with -1 representing vertical upwards and 0 horizontal. (b) Pathlength (in centimeters) in lower MACRO, which roughly sets a minimum on the penetrating power of the initial muon.

## Chapter 6 Interpretation

### 6.1 Corrections and Estimates of Uncertainty in the Measurement

#### 6.1.1 Externally-produced Neutrino-induced Muon Background

##### CORRECTION and UNCERTAINTY

If the containment cut is not perfect, upward throughgoing (neutrino-induced) muons produced outside the detector may appear to be semi-contained. A Monte Carlo dataset of 100,000 events, with an equivalent livetime of 143.5 yr, has been created using the upgoing muon generator described in Section 3.4.2. The generator is based on the flux of upgoing muons due to atmospheric neutrinos that would exist if there were no oscillations. After putting the data through the simulation of detector deadtime and inefficiency, the events passing the semi-contained analysis sum to a prediction of 1.77 events for the livetime of this analysis. Adjusting the flux for oscillations, the prediction is 0.97 events. (Here, and throughout the rest of this chapter, data assuming oscillations are computed at a test point of  $\nu_\mu$  disappearance oscillations with  $\sin^2 2\theta = 1$ ;  $\Delta m^2 = 3.2 \times 10^{-3} \text{ eV}^2$ .) This is to be subtracted from the measured events. The correction is 1-2% of the total number of events, a statistical error is applied for fluctuations in the background, and a systematic uncertainty of 1% of the total number of events is applied to account for any inaccuracy in this procedure.

#### 6.1.2 Mistimed Background

UNCERTAINTY only

Even in the Monte Carlo, not all neutrino-induced events are measured to have  $\beta = -1$  (see Figure 6.1a). In the  $|\beta| < 1$  region ( $|1/\beta| > 1$ ) there are events in which the muon (or perhaps some other charged particle from the interaction that creates a track and is chosen by the analysis to characterize the event) is actually moving at less than the speed of light, as well as events that are mistimed due to multiple particles hitting a single tank at different places. At  $|\beta| > 1$ , only the latter class exists. In the real data, 9 events exist in the regions  $-2 < 1/\beta < -1.2$  and  $-0.8 < 1/\beta < 0$  which is consistent with the Monte Carlo prediction of 7.9 events (see Figure 6.1b). Therefore, there is no empirical evidence for additional mistimed background in this analysis, in which all optional cuts are applied; therefore, no subtraction is made. If half the events in the sidebands are really due to mistimed background, a linear fit to them suggests about 1 event in the signal region, so an uncertainty of 1 event is assessed due to mistimed background. This uncertainty is asymmetrical; it can only cause the measurement to be higher than the true value.

### 6.1.3 Remaining $\beta = -1$ Background

UNCERTAINTY only

This analysis attempts to minimize the backgrounds induced by downgoing muons by implementing all of the optional cuts. Figure 5.15 in Chapter 5 showed that the less restrictive combinations of cuts appear to have more  $\beta = -1$  background than the all-optional-cuts combination used in this analysis; however, that does not rule out the possibility that background events remain in the all-optional-cuts combination. A hand scan of events revealed that the sample remaining after applying all optional cuts appeared considerably cleaner than the events allowed by the less restrictive combinations. Because there is no clear evidence of background, no subtraction is made. A systematic uncertainty of 3 events is assigned. This uncertainty is asymmetrical; it can only cause the measurement to be higher than the true value.

As a check, 100,000 simulated downgoing atmospheric muons were passed through the upgoing semi-contained analysis. All failed to pass the analysis, which is approx-

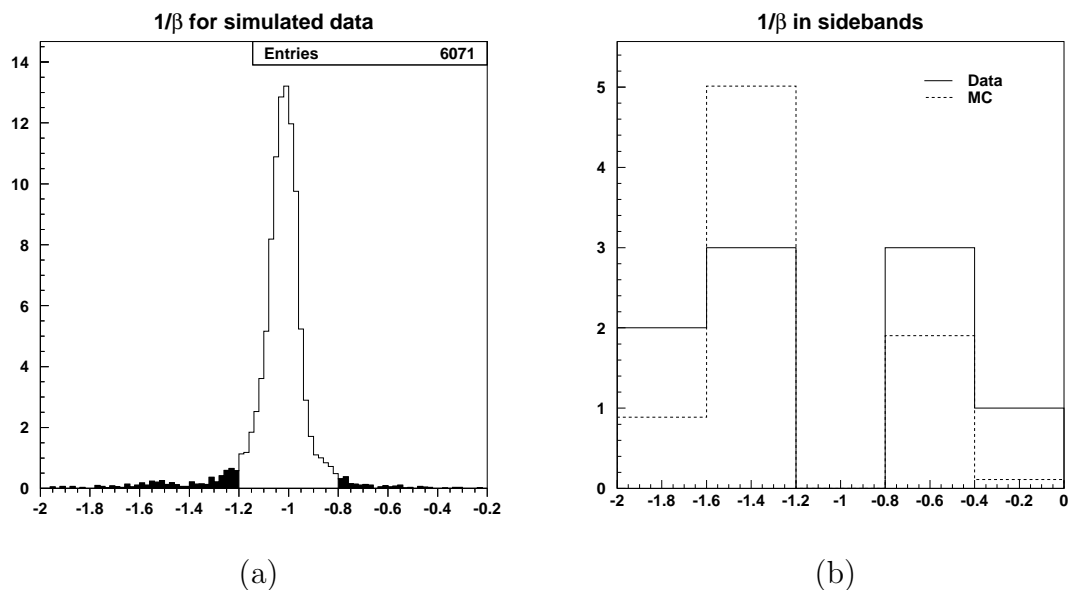


Figure 6.1: Even “signal” events from the simulation sometimes have measured  $\beta$  outside the signal region. (a) shows the  $1/\beta$  distribution from the simulation with fine binning. (b) compares the sidebands of the data (solid line) and the simulation (dashed line) at a coarser binning.

imately to say none generated an upgoing particle in the detector while escaping detection themselves. This represents a simulated livetime of under one week, however. No meaningful lower limit can be set on the background based on this simulation, but at least it gives no evidence of background.

### 6.1.4 The Nominal Detector Simulation

UNCERTAINTY only

An inaccurate detector simulation would change the prediction but would have no effect on what is measured. However, because discrepancies due to the simulation are an experimental rather than a theoretical issue, it has been the custom in MACRO to incorporate systematic uncertainty due to the simulation into the experimental error.

This analysis requires extreme reliance on the details of the Monte Carlo. The great majority of neutrino-induced particles in the detector range out without leaving

a trace or hit just a couple of streamer tubes. Out of over 150,000 generated neutrino interactions, fewer than a thousand create a track and hit two scintillators; the rest do not even pass the preliminary stages of this analysis. Thus, we are relying on the simulation's estimate of the occurrence of a relatively rare process. Furthermore, specifying the initial kinematics of an event is not enough to determine if the event will be detectable. To demonstrate this, 10,000 neutrino interactions were generated, determining the initial kinematics of particles emerging from the interaction. Then, each of the 10,000 interactions was tracked in GMACRO four times, the only difference being the random number seed to the Monte Carlo. Each run of GMACRO rolled the dice to determine how the particles interacted in the detector, computed the response of MACRO, and wrote a run file of 10,000 events to disk. Utilizing a preliminary version of this analysis, 741 of the 10,000 neutrino interactions produced an event detected by the analysis in at least one of the GMACRO runs, but only 249 of them were detected in all four runs of GMACRO. Each of the four runs produced  $483 \pm 14$  detectable events. This means that around half of all detectable events in the Monte Carlo had kinematics so susceptible to change that they would not be detectable if the Monte Carlo made different choices. (See Figure 6.2.)

It is difficult to estimate an uncertainty due to the simulation. GMACRO is very well-certified to perform well on the type of event MACRO sees most often – single relativistic muons (see the plots in Section 3.4.3). However, the events on which this analysis is based are sometimes much more complicated, involving multiple charged and uncharged particles. There is little empirical evidence that GMACRO produces an accurate response in these events. However, many of the elements comprising GMACRO – the materials, geometry and physics processes – are well-understood and certified in their own right. GMACRO's estimate of the timing and energy measurements when multiple particles hit a single tank is not known to be good; in fact, it is known that the GMACRO algorithm is an oversimplification of the true case. It is suspected that this is the chief source of discrepancy between the true and simulated response, particularly for high energy neutrino interactions with many secondary particles.

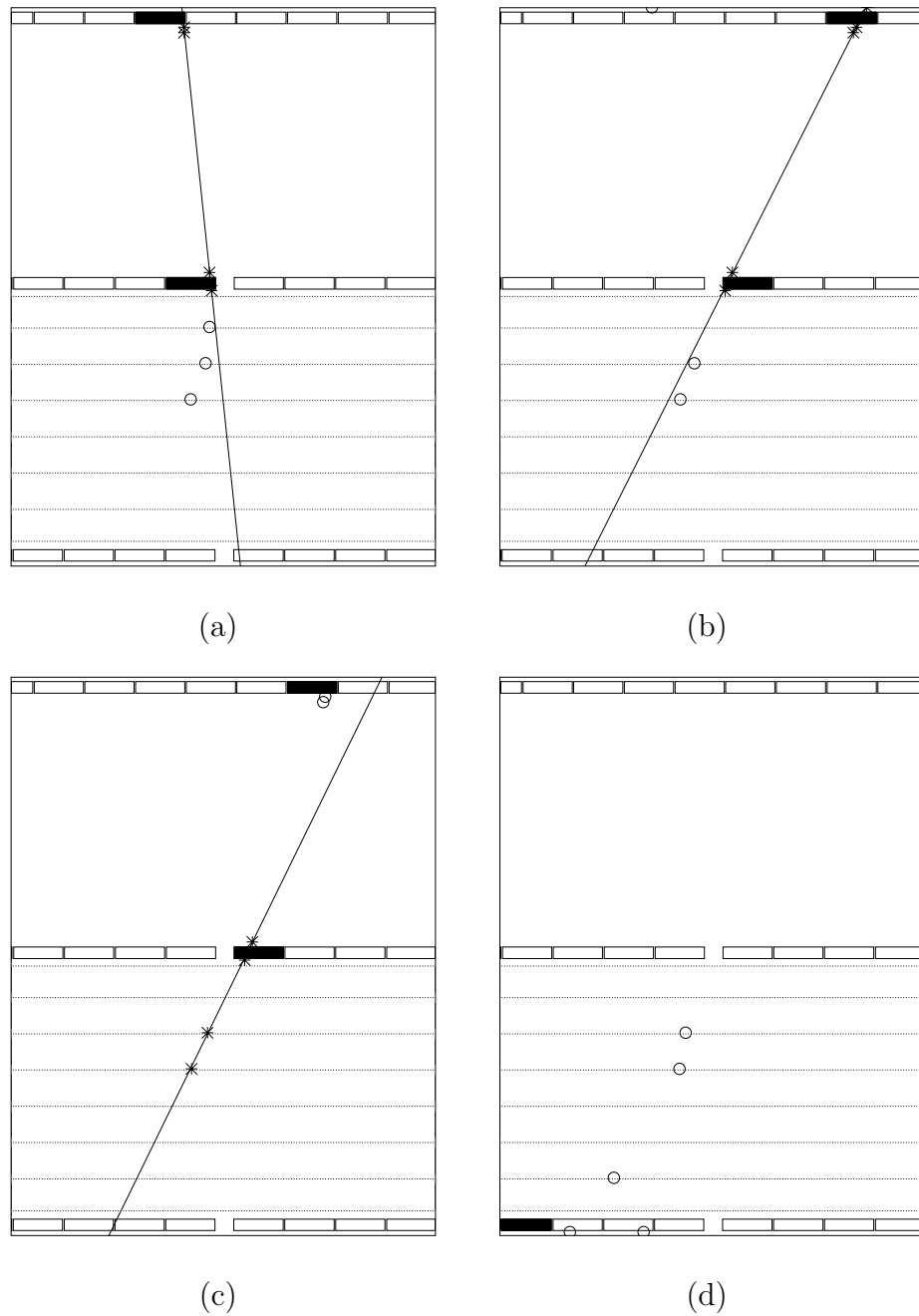


Figure 6.2: The same neutrino interaction, tracked four times by GMACRO. The initial particles are a 730 MeV  $\mu^+$  moving up and to the right, and a 390 MeV neutron moving down and to the left. Only event (b) passes the analysis and is detected. This is an extreme example of differences in tracking, not typical.

Evidence of inaccuracy in the simulation comes from an attempted analysis of a higher-energy subset of semi-contained neutrino interactions, which loosened the strict requirements on tracking from the analysis presented in this work, and attempted to remain efficient for multiple-particle events. The higher-energy analysis relied primarily on scintillator information and looked for events with a generally-upward flow of particle timing. The analysis had to be abandoned because of inconsistencies between the classes of events seen in the data and in the simulation. It should be noted, however, that the events in the higher-energy analysis were inherently more difficult to simulate and to reconstruct due to the presence of multiple particles, higher-energy particles, and more electrons and photons.

Several of the major parameters within GMACRO have been varied to get a sense of the variation. Raising the mass by 5% increases the prediction by 3.8%. Changing the hadronic interaction model to the version of FLUKA incorporated in Geant 3.21 decreases the prediction by 5.5%. Lowering the ERP trigger thresholds in the simulation by 2 MeV decreases the prediction by 1.4%. Raising all the Geant CUTS parameters from 0.5 MeV to 1 MeV (so that particles are tracked as they lose energy only until they reach 1 MeV) increases the prediction by 0.7%. Setting all streamer tube trigger thresholds to their default values, rather than the values determined by tuning, decreases the prediction by 4.0%. I believe these tests overstate the uncertainty due to the simulation, because there are good reasons to believe the parameters used in the prediction are more accurate than the alternate parameters tested here. All the variations mentioned in this paragraph add in quadrature to 7.9%. Since this is probably an overestimate, a systematic uncertainty of 6% is assigned to the simulation.

### **6.1.5 The Simulation of Non-ideal Detector Performance**

The accuracy of the simulation of dead periods and inefficiency was discussed at length in Section 3.4.4. A conservative uncertainty of 2% is assessed for inaccuracies in this simulation.

## 6.2 Estimates of Uncertainty in the Theoretical Prediction

The systematic uncertainty in comparing observation to expectation is dominated by theoretical uncertainty. At present, there is no unique and reliable estimate of the systematic uncertainty of the flux and cross section models. The MACRO collaboration has chosen conservatively to assign large uncertainties in the energy range relevant for this analysis.

### 6.2.1 Neutrino Flux

The calculations of neutrino flux are least accurate at low energies, especially at 1 GeV and below, where solar modulation and geomagnetic effects complicate the calculations, and the calculations cannot be checked against high-statistics measurements of muons at ground level. After conferring with the authors of the Bartol flux, MACRO has set a systematic uncertainty of 20% due to possible inaccuracies in the flux calculation at the energies relevant to this analysis.

### 6.2.2 Neutrino Cross Section

The experimental measurement of neutrino cross section for energies near and below 1 GeV is imprecise (recall Figure 4.5). Unless one has faith in a particular model, the uncertainty cannot be less than 10-20%. As described in Section 4.2, although the underlying weak interaction is well-understood at the partonic level, complications due to nuclear and QCD effects muddle the theoretical situation considerably. While the simulation used in this analysis is based on the Lipari cross section model (Section 4.2.1), another dataset has been generated using the NEUGEN model (Section 4.2.2); 3.6% fewer events are detected by this analysis from the NEUGEN dataset. MACRO has assigned a systematic uncertainty of 15% due to possible inaccuracies in the cross section model.

### 6.2.3 The Solar Cycle

As detailed in Section 5.2.3, the Monte Carlo dataset on which this analysis is based was generated using the flux at solar minimum for 77% of the simulated livetime and the flux at solar midcycle for the rest. It is not clear exactly what the authors of the flux meant by “solar maximum,” “solar minimum” and “solar midcycle,” nor how the amplitude of the solar modulation during the data-taking compared with earlier cycles on which the flux calculation was based. Therefore, a different proportion of solar minimum, midcycle and maximum events might have been a better model of the actual conditions during data-taking.

The simulation finds fewer detected events under the solar midcycle conditions than at solar minimum:  $8\% \pm 1.5\%$  fewer when oscillations are not simulated, and  $10\% \pm 2\%$  fewer with oscillations. If the proportion of simulated livetime generated with the solar midcycle flux were halved (to 12%) or increased by 50% (to 35%), the prediction would have varied by about 1%. Therefore, a systematic uncertainty of 1% is applied due to possible inaccuracies in the modeling of the solar cycle.

### 6.2.4 Summary

Table 6.1 summarizes the corrections and uncertainties, and computes the total experimental and theoretical systematic uncertainties by adding all terms in quadrature.

The final measurement is

$$M = 76 \pm 11.5\%_{stat} \begin{matrix} +6.4\% \\ -7.6\%_{syst} \end{matrix}$$

The prediction without oscillations is

$$P_{no} = 171 \pm 25.1\%_{theor}$$

and with oscillations at the test point  $\sin^2 2\theta = 1, \Delta m^2 = 3.2 \times 10^{-3} \text{ eV}^2$ , the prediction is

Source	Correction	Uncertainty
External Upgoing Muons	-1 event	$\pm 1\%$
Mistimed Background		-1 ev = -1.3%
$\beta = -1$ Background		-3 ev = -3.9%
Nominal Detector Simulation		$\pm 6\%$
Simulation of Non-ideal Detector Performance		$\pm 2\%$
Total Experimental Systematic	-1 event	+6.4% -7.6%
Counting Statistics		$\pm 11.5\%$
Flux		$\pm 20\%$
Cross Section		$\pm 15\%$
Solar Cycle		$\pm 1\%$
Simulation Statistics		$\pm 1.3\%$
Total Theoretical Systematic		$\pm 25.1\%$

Table 6.1: Summary of corrections and uncertainties.

$$P_o = 96 \pm 25.1\%_{theor}$$

## 6.3 Oscillation Analysis

### 6.3.1 The Number of Events

Figure 6.3 shows the measurement and the two predictions with errors. The statistical and systematic uncertainties of the measurement have been added in quadrature, yielding  $^{+13.2\%}_{-13.8\%}$ .

For an ensemble of experiments in which the true value being measured  $T$  is distributed according to the probability density function (pdf)  $P_T(T)$ , and the measurement  $M$  is distributed about the true value with a pdf  $P_M(M|T)$ , the likelihood of a measurement  $M$  is

$$\mathcal{L} = \int dT P_T(T) P_M(M|T)$$

which in our case is

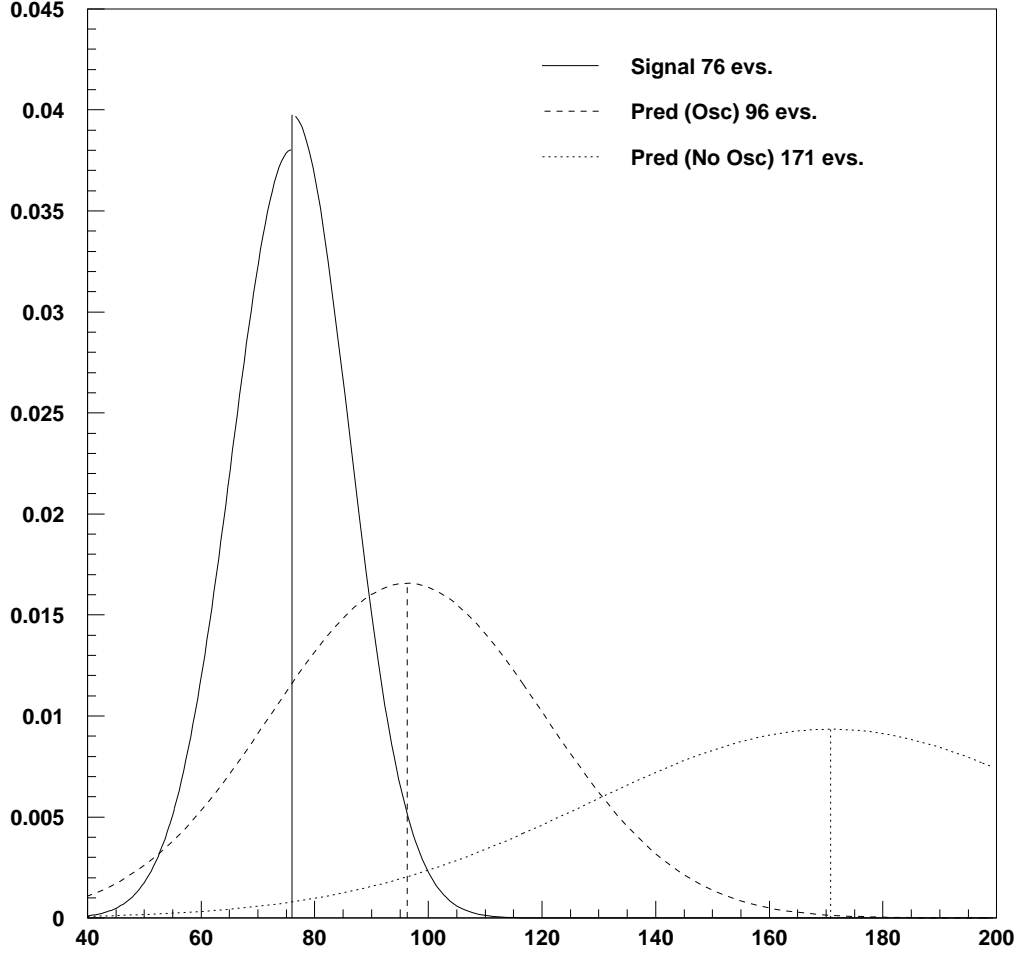


Figure 6.3: The measurement and two predictions, with errors shown. The area under each curve is unity.

$$\mathcal{L} = \int dS_t P_G(S_t; 1, \sigma_t) \int ds_m P_G^2(s_m; 1, \sigma_m^+, \sigma_m^-) P_P(N; S_t \times s_m \times N^0)$$

where  $S_t$  is a scaling variable representing the theoretical uncertainty,  $s_m$  is a scaling variable for the experimental uncertainty,  $P_G(x; \mu, \sigma)$  is the gaussian distribution,

$P_G^2(x; \mu, \sigma^+, \sigma^-)$  is the gaussian with different variances in the positive and negative directions (like the solid line in Figure 6.3 above),  $P_P(N; N_0)$  is the Poisson distribution,  $N$  is the measured number of events and  $N^0$  is the prediction.  $\sigma_t$  and  $\sigma_m$  are represented as percentages, i.e.,  $\sigma_t = 0.251$ ,  $\sigma_m^+ = .064$  and  $\sigma_m^- = .076$ .

Computing likelihood this way shows the likelihood of the real measurement is 9.2 times greater for the oscillations prediction than for the no-oscillations prediction. The two-sided probability that fluctuations would cause the measurement to be as far as it is or farther from the oscillations prediction (including all errors) is 47%; that is, almost half the time you did the experiment you would get a worse agreement. For the no-oscillations prediction, the probability is 3.3%. Thus, this aspect of the experiment excludes the no-oscillations theory at greater than 95% confidence level.

### 6.3.2 The Angular Distribution

The above oscillations analysis merely counts events and ignores much of what is known about them. Neutrino oscillations depend on two properties of the neutrino: its energy and the distance it travels from the point of neutrino production to the detector. The energy of the muon is correlated to the energy of the parent neutrino, but MACRO is not optimized to say anything about the muon energy. On the other hand, the direction the muon travels is correlated with the direction the neutrino was traveling, and the neutrino direction determines where on the surface of the earth it was created and thus how far it has traveled. Therefore, one may gain additional insight into oscillations by considering the angular distribution of the detected muons.

The muon does not perfectly follow the path of the neutrino, especially at the relatively low energies of neutrinos in this analysis. The neutrino flux is peaked at the horizontal, but the opening angle between the neutrino and muon directions (Figure 6.4a) flattens the flux out (Figure 6.4b). Nonetheless, a correlation remains between the measured muon direction and the length traveled by the muon (Figure 6.4c) such that, for certain oscillation parameters, more events disappear from vertical directions than from horizontal (Figure 6.4d).

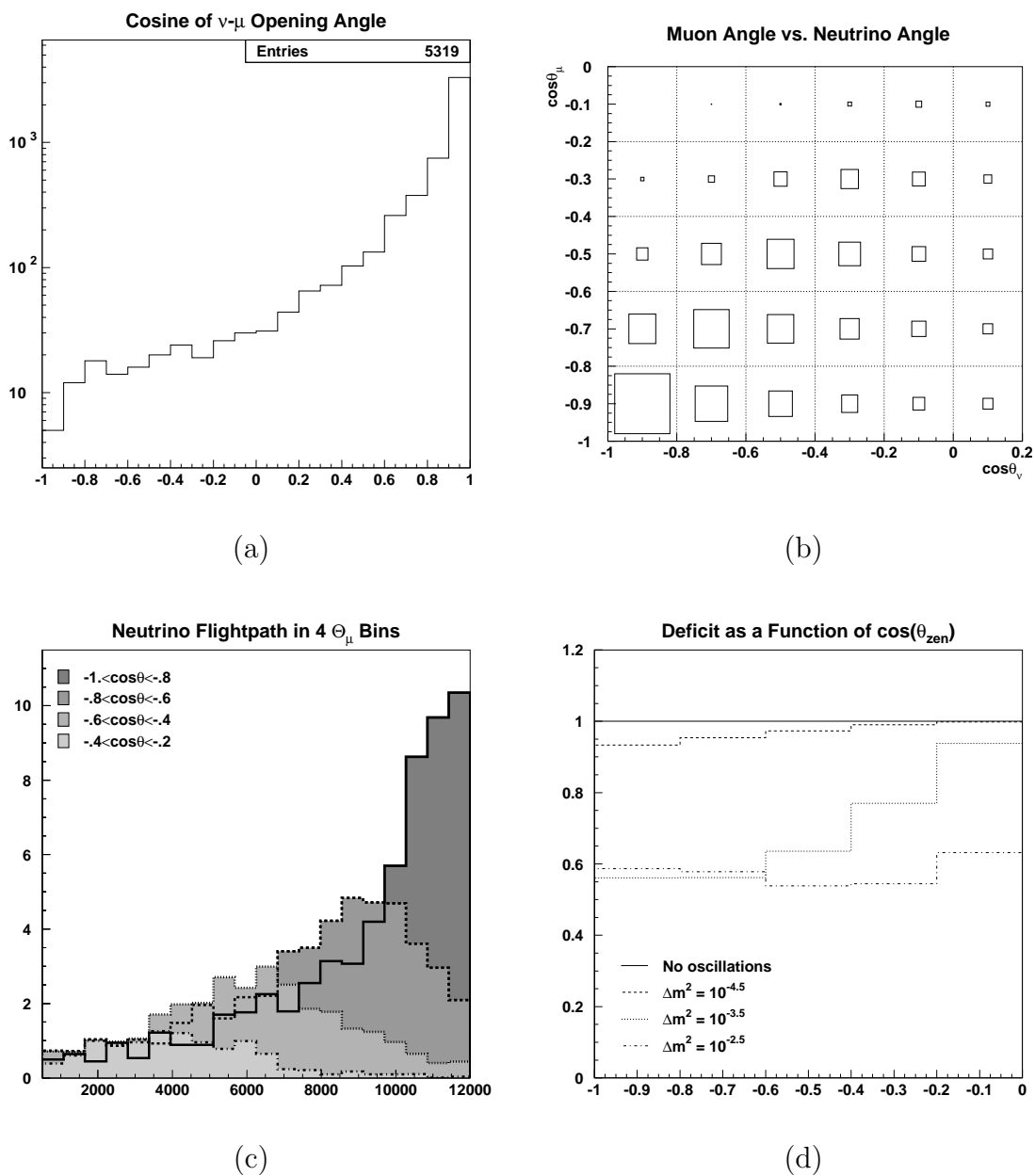


Figure 6.4: Zenith angle effects.

Figure 6.5 shows the measurement and two predictions for the angular distribution of observed muons, with errors.

We may again compute the likelihood of the measurement assuming an ensemble of experiments in which the true value is distributed about the prediction according to the stated errors; however, we must take care to apply certain errors in common



$$\mathcal{L} = \int dS_G P_G(S_G; 1, \sigma_t^G) \int ds_G P_G(s_G; 1, \sigma_m^G) \times \prod_i^{Nbin} \int dS_i P_G(S_i; 1, \sigma_t^b) \int ds_i P_G(s_i; 1, \sigma_m^b) P_P(N_i; S_G s_G S_i s_i N_i^0)$$

where the theoretical uncertainty has been split into  $\sigma_t^G$ , a global part that is in common across all bins, and  $\sigma_t^b$  which is an independent variation in each bin; similarly for the experimental uncertainty  $\sigma_m^G$  and  $\sigma_m^b$ . I take the uncertainties to be the same in all five bins. The portions of the uncertainties assigned to the global uncertainty are shown in Table 6.2.

Source	Total Uncertainty	Global Uncertainty
External Upgoing Muons	$\pm 1\%$	$\pm 1\%$
Mistimed Background	$-1.3\%$	$-1.3\%$
$\beta = -1$ Background	$-3.9\%$	$-3.9\%$
Nominal Detector Simulation	$\pm 6\%$	$\pm 4\%$
Non-ideal Detector Performance	$\pm 2\%$	$\pm 2\%$
Total Experimental		$\pm 5.5\%$
Flux	$\pm 20\%$	$\pm 14\%$
Cross Section	$\pm 15\%$	$\pm 15\%$
Solar Cycle	$\pm 1\%$	$\pm 1\%$
Simulation Statistics	$\pm 1.3\%$	$\pm 1.3\%$
Total Theoretical		$\pm 20.6\%$

Table 6.2: Summary of corrections and uncertainties.

From this point, we are dropping the distinction between positive and negative experimental uncertainty. The theoretical and experimental bin-by-bin errors are chosen to make the variance of the total number of events the same as in the unbinned analysis.

Following this procedure, we again find the data is more likely under the oscillations hypothesis than under the no-oscillations hypothesis, this time by a factor of 20. If an ensemble of experiments were performed as in the previous section, for the oscillations hypothesis a result with lower likelihood than that of our real data would be obtained 89% of the time; for the no-oscillations hypothesis, the number is 68%.

The latter result may seem in contradiction to the very low probability found in the previous section for measuring the total number of events we measured if the no-oscillations hypothesis is true. However, this shows the importance of taking the angular information into account. There are many ways to fill the bins of the angle histogram to add up to 76 events; and most of them are exceptionally unlikely. However, the way the bins are filled in our real measurement is compatible with a suppression of the rate uniform across all bins, which is somewhat accommodated by the theoretical and experimental uncertainty. If, to rank the unlikeliness of a given measurement, instead of using the raw likelihood we use the unified approach of Feldman and Cousins [103], the real measurement is heavily penalized when considering the no-oscillations hypothesis because there is another hypothesis that the data fits much better. With this ranking, the probabilities of a measurement as unlikely as our real measurement is 64% for the oscillations hypothesis and 1.5% for no-oscillations.

How can the no-oscillations hypothesis be excluded at greater than 95% confidence level by the Feldman-Cousins prescription, when the raw likelihood of the real measured data for that hypothesis shows a probability of greater than 50%? When using the raw likelihood, which is the traditional method of evaluating a null hypothesis, the decision whether to exclude is independent of any other hypotheses that may be considered as alternatives. On the other hand, Feldman-Cousins is based on the relative probabilities of different hypotheses. If the no-oscillations hypothesis were true, there would be many results (counts in the bins of the histogram that are fluctuated from the true values) that were likely at the 68% level; however, the vast majority of these would not fit any other hypothesis much better than they fit the no-oscillations hypothesis. However, the real measured data fits alternative hypotheses more than 20 times better than it fits the no-oscillations hypothesis. That is why the Feldman-Cousins prescription rules out the no-oscillations hypothesis.

Figure 6.6 shows, for a grid of oscillation hypotheses, the confidence level at which they are ruled out by this measurement, using the Feldman-Cousins prescription. The best fit of the grid values considered is at maximal mixing and  $\Delta m^2 = 3.2 \times 10^{-2} \text{ eV}^2$ . Small values of  $\Delta m^2$  or of  $\sin^2 2\theta$  are excluded because they correspond to too small a

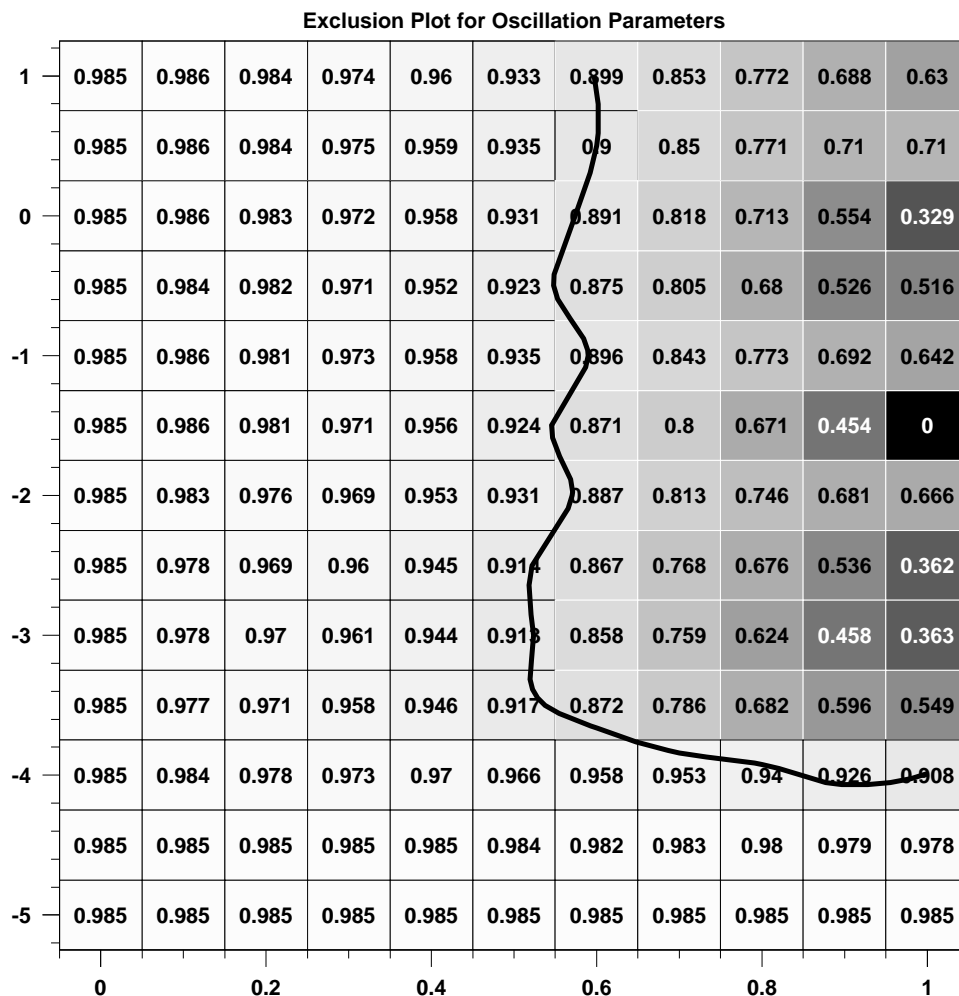


Figure 6.6: Considering the angular distribution of this measurement of semi-contained upgoing muons, for a grid of oscillation parameters, the confidence level at which those parameters are ruled out. The vertical axis is  $\log_{10} \Delta m^2$  while the horizontal axis is  $\sin^2 2\theta$ . An approximate 90% confidence level contour is shown. Parameters below or left of the contour are ruled out.

magnitude of  $\nu_\mu$  disappearance. Arbitrarily large values of  $\Delta m^2$  are allowed because for hypotheses above a certain point, all upgoing muons are fully oscillated and raising  $\Delta m^2$  does not change the predicted number.

## 6.4 This Analysis in the Context of Other MACRO Analyses

This analysis is generally incompatible with the no-oscillations hypothesis, and generally compatible with oscillations with maximal mixing and  $\Delta m^2 = 3.2 \times 10^{-3} \text{ eV}^2$ . This choice of parameters is not arbitrary; it is the value preferred by previously-published MACRO neutrino analyses [26, 52], and is generally the same as Super-Kamiokande's combined result [25]. It is striking that a single hypothesis is compatible with all MACRO analyses, which are based on different events and different analysis procedures, and span two orders of magnitude in energy distribution. The energy distribution is important because at the preferred oscillation parameters, neutrinos below a few GeV have reached their maximum deficit due to oscillations within a few tens of kilometers. Thus, in this analysis, at the preferred parameters we expect all neutrinos coming from below to be fully oscillated. However, at 100 GeV and above, only neutrinos from farthest away, from the most vertical downward direction, are fully oscillated. Thus, the angular signature of oscillations is different among the different analyses.

All oscillation analyses based on absolute measurements of atmospheric neutrino flux are hampered by the large theoretical uncertainties on the flux and on the cross section, a situation that is worst for lower-energy neutrinos (i.e., those considered in this analysis). The most precise measurements of oscillation effects have always been based on the comparison of two quantities (for example, muon neutrinos and electron neutrinos, or upward and downward neutrinos), in which much of the theoretical error cancels. It is difficult to draw conclusions comparing our measurements of lower-energy and of higher-energy neutrinos because the uncertainties on the flux and the cross section do not necessarily cancel when one is considering different energy regions.

However, a very fruitful combined analysis can be made with one MACRO analysis: the sample of both up- and down-going semi-contained neutrinos passing the Bottom face (topologies (e) and (f) in Figure 5.1 in the previous chapter). While

MACRO cannot distinguish the direction of the detected muon, it is known that the sample would contain nearly equal numbers of upward and downward particles in the absence of oscillations (recall from Section 4.1 that the flux is nearly up-down symmetric in the absence of oscillations), and an energy distribution almost identical to the present analysis (see Figure 5.2). However, for the preferred oscillation parameters, it is expected that most neutrinos from below (which have traveled hundreds or thousands of kilometers) would be fully oscillated so the flux would be reduced to about half of its nominal value, while neutrinos from above (which have traveled only tens of kilometers) would be hardly attenuated at all by oscillations. Thus, the measurement reported in this work (which I will refer to as Analysis *A*), consisting only of lower-energy neutrinos from below, would see about half the nominal flux, while the other analysis (Analysis *B*) would see about three quarters of the nominal flux (all of the downward neutrinos and half of the upward). Even if there were large errors in the absolute magnitude of the predicted interaction rate, the two results would differ from the oscillations prediction by the same fraction. Thus, a combined analysis accords us some immunity from the large theoretical uncertainties. This general picture is borne out in Analysis *A* (Figure 6.5 above), which sees 76 events with 96 predicted at the oscillations test point, and Analysis *B* (Figure 6.7), which sees 262 events with 288 predicted.

In the combined analysis, the various uncertainties are accounted for by a number of scale factors, as named in Table 6.3. The values used for the scale factors are derived in Table 6.4. Analysis *B* has been published elsewhere [52], although the measurement used here has been updated since the publication of [52]. Systematic uncertainties are taken from that publication, and subjective judgment is used to partition the errors among the various scale factors. Three of the scale factors ( $f_i$ ,  $s_i^a$  and  $s_i^b$ ) have nothing assigned to them, and they are discarded.

The no-oscillations hypothesis cannot find a decent likelihood for both the Analysis *A* bins and the Analysis *B* bins simultaneously by assuming a single error in the absolute normalization. The real measured data is 78 times more likely under the oscillations hypothesis than under the no-oscillations hypothesis. For an ensemble of

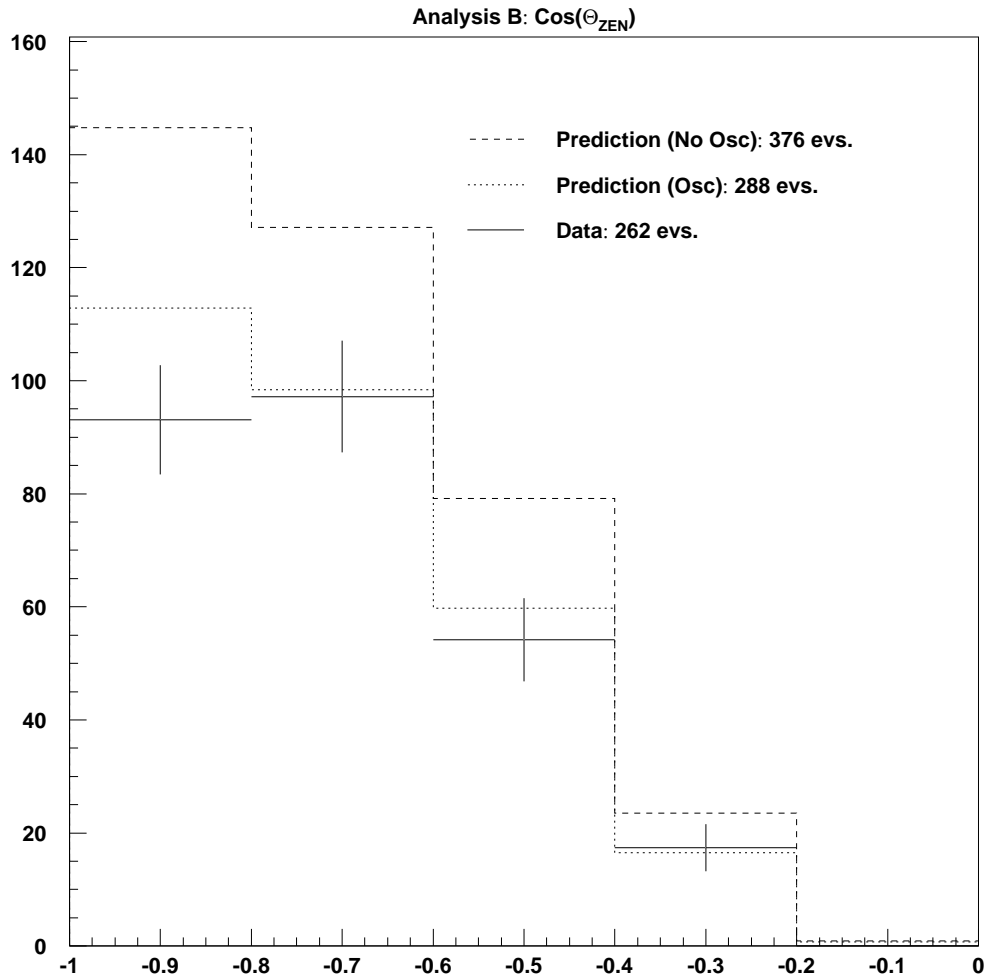


Figure 6.7: The angular distribution of events from Analysis *B* and two predictions, before the assignment of any errors (other than counting statistics).

experiments in which the true value being measured in each bin varies according to the errors tabulated in Table 6.4, the 10 bin values (five from each analysis) would be as unlikely as the 10 actual measured bin values 83% of the time under the oscillations hypothesis, and less than 0.1% under the no-oscillations hypothesis (using the Feldman-Cousins prescription).

Figure 6.8 shows the exclusion plot for the combined analysis. The allowed region

$S$	Theoretical error, common to both analyses and all angle bins
$F$	Experimental error, common to both analyses and all angle bins
$S^A$	Theoretical error, Analysis $A$ , common to all bins
$F^A$	Experimental error, Analysis $A$ , common to all bins
$S^B$	Theoretical error, Analysis $B$ , common to all bins
$F^B$	Experimental error, Analysis $B$ , common to all bins
$s_i$	Theoretical error, common to both analyses, for angle bin $i$
$f_i$	Experimental error, common to both analyses, for angle bin $i$ . NOT USED.
$s_i^a$	Theoretical error, Analysis $A$ , angle bin $i$ . NOT USED.
$f_i^a$	Experimental error, Analysis $A$ , angle bin $i$ .
$s_i^b$	Theoretical error, Analysis $B$ , angle bin $i$ . NOT USED.
$f_i^b$	Experimental error, Analysis $B$ , angle bin $i$ .

Table 6.3: Scale factors in the combined analysis to account for systematic uncertainties.

EXPERIMENTAL	Tot A	Tot B	$F$	$F^A$	$F^B$	$f_i^a$	$f_i^b$
$\mu$ -induced BG	-4%	4%		-4%	4%		
External $\mu$ BG	1%	0		1%			
Mistimed BG	-1%	0		-1%			
Nominal Detector MC	6%	6%	4.5%	3.8%	3.8%	2.2%	2.2%
Detector Problems	2%	3%		2%	3%		
Total			4.5%	5.2%	6.3%	2.2%	2.2%
THEORETICAL	Tot A	Tot B	$S$	$S^A$	$S^B$	$s_i$	
Flux	20%	20%	18.3%			14%	
Cross Section	15%	15%	14%	5.5%			
Solar Cycle	1%	1%		1%	1%		
MC Stats	1.3%	2.2%		1.3%	2.2%		
Total			23.2%	5.7%	2.4%	14%	

Table 6.4: Scale factors in the combined analysis to account for systematic uncertainties.

has been greatly reduced compared to that from Analysis  $A$  alone (or from Analysis  $B$  alone). In particular, the Analysis  $A$  data, considered alone, are compatible with arbitrarily large values of  $\Delta m^2$ . That is because the upgoing neutrinos in all of the bins with significant statistics are “fully-oscillated” for any value of  $\Delta m^2$  above  $10^{-3}$  eV<sup>2</sup> or so, and increasing  $\Delta m^2$  would not change the prediction for Analysis  $A$  at all. However, as  $\Delta m^2$  increases above  $3.2 \times 10^{-1}$  eV<sup>2</sup>, more and more of the

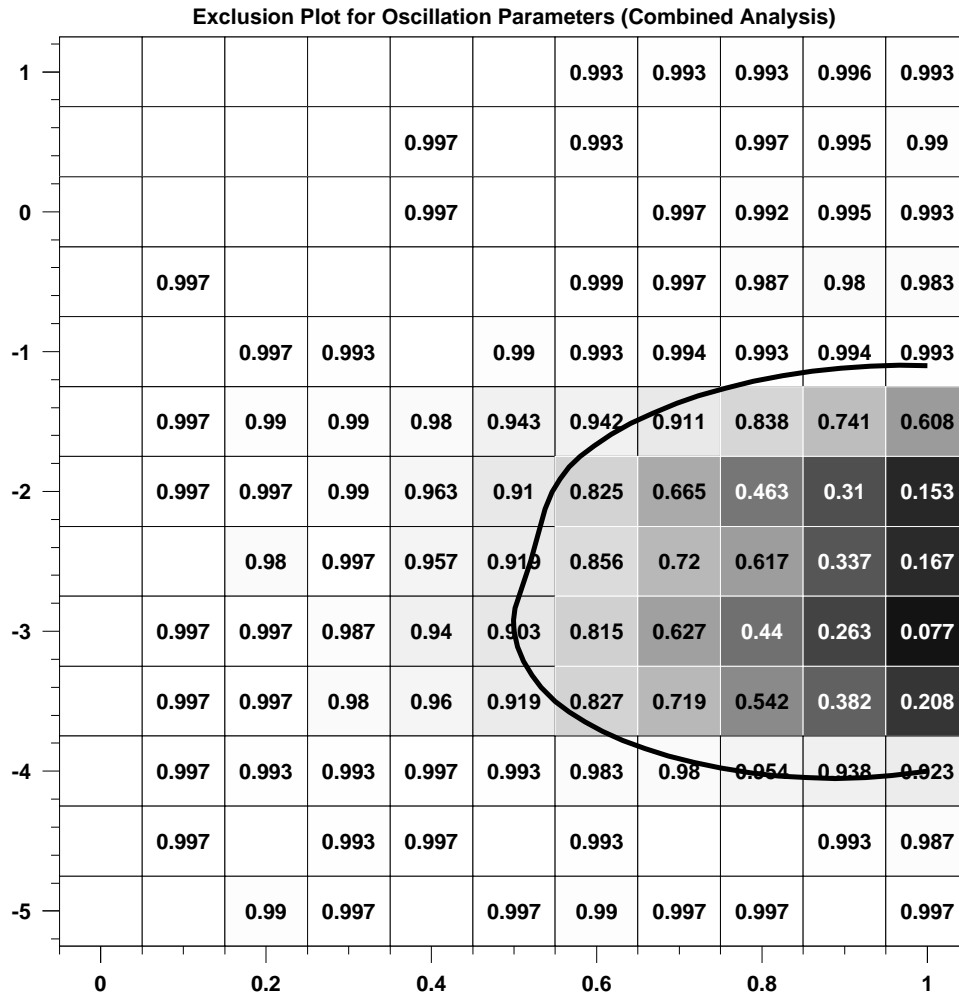


Figure 6.8: The exclusion plot, analogous to Figure 6.6, for the combined analysis. Blank squares were below the detection limit of the software ( $C.L. > 0.997$ ). The small region within the contour is allowed, and the large region outside is excluded at 90% confidence level.

downgoing neutrinos in Analysis  $B$  begin to disappear. Although Analysis  $B$  alone could accommodate the reduction by an error in the overall normalization, considering both analyses together shows that upgoing neutrinos are disappearing and downgoing are not. That restricts  $\Delta m^2$  to a relatively small region.

## Chapter 7 Conclusion

This thesis reports a study of atmospheric neutrinos interacting in the MACRO detector. A Monte Carlo calculation, based on the Bartol flux calculation and the Lipari cross section model, predicts on the order of 100 events could be observed in the live-time of this analysis (4.5 years). An analysis has been developed, taking extra care to eliminate backgrounds due to the copious downgoing atmospheric muons. 77 events are found, a result generally consistent with neutrino oscillations with the parameters suggested by higher-energy MACRO analyses as well as other experiments, and inconsistent with no oscillations. However, due mostly to large theoretical uncertainties, the allowed parameter space from this analysis alone is not very precise. Combining this analysis with another MACRO analysis, of neutrino interactions with similar energy but different topology, causes a partial cancellation of much of the uncertainty and allows a more precise determination of oscillation parameters.

## Bibliography

- [1] W. Pauli, "Letter to the Physical Society of Tubingen," reproduced in *Physics Today* **31**(9):23, 1978.
- [2] E. Fermi, "An Attempt of a Theory of Beta Radiation. 1.," *Z. Phys.* **88**:161, 1934. In German.
- [3] F. Reines and C. Cowan, "Detection of the Free Neutrino," *Phys. Rev.* **92**:830, 1953.
- [4] T. Lee and C. Yang, "Question of Parity Conservation in Weak Interactions," *Phys. Rev.* **104**:254, 1956.
- [5] G. Danby *et al.*, "Observation of High-Energy Neutrino Reactions and the Existence of Two Kinds of Neutrinos," *Phys. Rev. Lett.* **9**:36, 1962.
- [6] F. Hasert *et al.*, "Observation of Neutrino-like Interactions without Muon or Electron in the Gargamelle Neutrino Experiment," *Phys. Lett.* **B46**:138, 1973.
- [7] A. Benvenuti *et al.*, "Observation of Muonless Neutrino Induced Inelastic Interactions," *Phys. Rev. Lett.* **32**:800, 1974.
- [8] B. Barish *et al.*, "Neutral Currents in High-Energy Neutrino Collisions: An Experimental Search," *Phys. Rev. Lett.* **34**:538, 1975.
- [9] B. Barish *et al.*, "Exploratory Study of High Energy Neutrino Interactions," *Phys. Rev. Lett.* **31**:565, 1973.
- [10] B. Aubert *et al.*, "Scaling-Variable Distributions in High-Energy Inelastic Neutrino Interactions," *Phys. Rev. Lett.* **33**:984, 1974.
- [11] R. Davis, Jr., D. S. Harmer, and K. C. Hoffman, "Search for Neutrinos from the Sun," *Phys. Rev. Lett.* **20**:1205, 1968.

- [12] for **Mont Blanc Neutrino Observatory** Collaboration, C. Castagnoli (IAU Circular 4323), 1987.
- [13] **Kamiokande** Collaboration, K. Hirata *et al.*, “Observation of a Neutrino Burst from the Supernova SN1987A,” *Phys. Rev. Lett.* **58**:1490, 1987.
- [14] **IMB** Collaboration, R. Bionta *et al.*, “Observation of a Neutrino Burst in Coincidence with Supernova 1987A in the Large Magellanic Cloud,” *Phys. Rev. Lett.* **58**:1494, 1987.
- [15] S. Weinberg, *Proceedings of the XXVI International Conference on High Energy Physics 1992*. A.I.P., New York, 1993. p. 346.
- [16] **Particle Data Group**, D. Groom, *et al.*, “Review of Particle Properties,” *Eur. Phys. Jour.* **C15**:1, 2000.
- [17] F. Boehm and P. Vogel, *Physics of Massive Neutrinos*. Cambridge University Press, Cambridge, 1992. p. 217.
- [18] B. Kayser, “On the Quantum Mechanics of Neutrino Oscillation,” *Phys. Rev.* **D24**:110, 1981.
- [19] L. Wolfenstein, “Neutrino Oscillations in Matter,” *Phys. Rev.* **D17**:2369, 1978.
- [20] **K2K** Collaboration, S. H. Ahn *et al.*, “Detection of Accelerator Produced Neutrinos at a Distance of 250-km,” *Phys. Lett.* **B511**:178, 2001, hep-ex/0103001.
- [21] **LSND** Collaboration, E. D. Church, “Evidence for Neutrino Oscillations at LSND,” *Nucl. Phys.* **A663**:799, 2000.
- [22] B. Armbruster *et al.*, “Search for  $\bar{\nu}_\mu \rightarrow \bar{\nu}_e$  Oscillations with KARMEN2,” *Nucl. Phys.* **A663**:803, 2000.
- [23] **SNO** Collaboration, Q. R. Ahmad *et al.*, “Measurement of the Charged Current Interactions Produced by B-8 Solar Neutrinos at the Sudbury Neutrino Observatory,” *Phys. Rev. Lett.* **87**:071301, 2001, nucl-ex/0106015.

- [24] **Super-Kamiokande** Collaboration, Y. Fukuda *et al.*, “Evidence for Oscillation of Atmospheric Neutrinos,” *Phys. Rev. Lett.* **81**:1562, 1998, hep-ex/9807003.
- [25] **Super-Kamiokande** Collaboration, T. Kajita, “Study of Neutrino Oscillations with the Atmospheric Neutrino Data from Superkamiokande,” *Nucl. Phys. Proc. Suppl.* **100**:107, 2001.
- [26] **MACRO** Collaboration, M. Ambrosio *et al.*, “Measurement of the Atmospheric Neutrino-Induced Upgoing Muon Flux using MACRO,” *Phys. Lett.* **B434**:451, 1998.
- [27] **Soudan-2** Collaboration, W. A. Mann, “New Results on Atmospheric Neutrinos from Soudan 2,” *Nucl. Phys. Proc. Suppl.* **91**:134, 2000, hep-ex/0007031.
- [28] **MACRO** Collaboration, S. Ahlen *et al.*, “Search for Slowly Moving Monopoles with the MACRO Detector,” *Phys. Rev. Lett.* **72**:608, 1994.
- [29] **MACRO** Collaboration, M. Ambrosio *et al.*, “Performance of the MACRO Streamer Tube System in the Search for Magnetic Monopoles,” *Astropart. Phys.* **4**:33, 1995.
- [30] **MACRO** Collaboration, M. Ambrosio *et al.*, “Magnetic Monopole Search with the MACRO Detector at Gran Sasso,” *Phys. Lett.* **B406**:249, 1997.
- [31] **MACRO** Collaboration, S. Ahlen *et al.*, “Search for Nuclearites Using the MACRO Detector,” *Phys. Rev. Lett.* **69**:1860, 1992.
- [32] **MACRO** Collaboration, M. Ambrosio *et al.*, “Nuclearite Search with the MACRO Detector at Gran Sasso,” *Eur. Phys. J.* **C13**:453, 2000.
- [33] **MACRO** Collaboration, S. Ahlen *et al.*, “Study of Penetrating Cosmic Ray Muons and Search for Large Scale Anisotropy at the Gran Sasso Laboratory,” *Phys. Lett.* **B249**:149, 1990.

- [34] **MACRO** Collaboration, M. Aglietta *et al.*, “Study of the Ultrahigh Energy Primary Cosmic Ray Composition with the MACRO Experiment,” *Phys. Rev.* **D46**:895, 1992.
- [35] **MACRO** Collaboration, S. Ahlen *et al.*, “Measurement of the Decoherence Function with the MACRO Detector at Gran Sasso,” *Phys. Rev.* **D46**:4836, 1992.
- [36] **MACRO** Collaboration, S. Ahlen *et al.*, “Arrival Time Distributions of Very High Energy Cosmic Ray Muons in MACRO,” *Nucl. Phys.* **B370**:432, 1992.
- [37] **MACRO** Collaboration, M. Ambrosio *et al.*, “Vertical Muon Intensity Measured with MACRO at the Gran Sasso Laboratory,” *Phys. Rev.* **D52**:3793, 1995.
- [38] **MACRO** Collaboration, M. Ambrosio *et al.*, “High Energy Cosmic Ray Physics with the MACRO Detector at Gran Sasso: Part I. Analysis Methods and Experimental Results,” *Phys. Rev.* **D56**:1407, 1997.
- [39] **MACRO** Collaboration, M. Ambrosio *et al.*, “High Energy Cosmic Ray Physics with the MACRO Detector at Gran Sasso: Part II. Primary Spectra and Composition,” *Phys. Rev.* **D56**:1418, 1997.
- [40] **MACRO** Collaboration, M. Ambrosio *et al.*, “Seasonal Variations in the Underground Muon Intensity as Seen by MACRO,” *Astropart. Phys.* **7**:109, 1997.
- [41] **MACRO** Collaboration, M. Ambrosio *et al.*, “Measurement of the Energy Spectrum of Underground Muons at Gran Sasso with a Transition Radiation Detector,” *Astropart. Phys.* **10**:11, 1999.
- [42] **MACRO** Collaboration, M. Ambrosio *et al.*, “High Statistics Measurement of the Underground Muon Pair Separation at Gran Sasso,” *Phys. Rev.* **D60**:032001, 1999.

- [43] **MACRO and EASTOP** Collaboration, M. Aglietta *et al.*, “Study of the Primary Cosmic Ray Composition around the Knee of the Energy Spectrum,” *Phys. Lett.* **B337**:376, 1994.
- [44] **MACRO and EASTOP** Collaboration, R. Bellotti, *et al.*, M. Aglietta, *et al.*, “Simultaneous Observation of Extensive Air Showers and Deep-Underground Muons at the Gran Sasso Laboratory,” *Phys. Rev.* **D42**:1396, 1994.
- [45] **GRACE and MACRO** Collaboration, M. Ambrosio *et al.*, “Coincident Observation of Air Cerenkov Light by a Surface Array and Muon Bundles by a Deep Underground Detector,” *Phys. Rev.* **D50**:3046, 1994.
- [46] **MACRO** Collaboration, S. Ahlen *et al.*, “Muon Astronomy with the MACRO Detector,” *Astrophys. J.* **412**:301, 1993.
- [47] **MACRO** Collaboration, S. Ahlen *et al.*, “Search for Neutrino Bursts from Collapsing Stars with the MACRO Detector,” *Astropart. Phys.* **1**:11, 1992.
- [48] **MACRO** Collaboration, M. Ambrosio *et al.*, “Real Time Supernova Neutrino Burst Detection with MACRO,” *Astropart. Phys.* **8**:123, 1998.
- [49] **MACRO** Collaboration, M. Ambrosio *et al.*, “Search for Lightly Ionizing Particles with the MACRO Detector,” *Phys. Rev.* **D62**:052003, 2000.
- [50] **MACRO** Collaboration, M. Ambrosio *et al.*, “Atmospheric Neutrino Flux Measurements Using Upgoing Muons,” *Phys. Lett.* **B357**:481, 1995.
- [51] **MACRO** Collaboration, M. Ambrosio *et al.*, “Limits on Dark Matter WIMPs Using Upward-Going Muons in the MACRO Detector,” *Phys. Rev.* **D60**:082002, 1999.
- [52] **MACRO** Collaboration, M. Ambrosio *et al.*, “Low Energy Atmospheric Neutrinos in MACRO,” *Phys. Lett.* **B478**:5, 2000.

- [53] **MACRO** Collaboration, M. Ambrosio *et al.*, “Neutrino Astronomy with the MACRO Detector,” *Astrophys. J.* **546**:1038, 2001.
- [54] **MACRO** Collaboration, M. Ambrosio *et al.*, “Matter Effects in Upward-going Muons and Sterile Neutrino Oscillations,” *Phys. Lett.* **B517**:59, 2001.
- [55] **MACRO** Collaboration, S. Ahlen *et al.*, “First Supermodule of the MACRO Detector at Gran Sasso,” *Nucl. Instr. and Meth.* **324**:337, 1993.
- [56] **MACRO** Collaboration, M. Ambrosio *et al.*, “The MACRO Detector at Gran Sasso,” Submitted to *Nucl. Instr. and Meth.*
- [57] F. James, *MINUIT: Function Minimization and Error Analysis Reference Manual (Version 94.1), Program Library D506*. CERN, Geneva, 1998.
- [58] CERN Application Software Group, *Geant: Detector Description and Simulation Tool; CERN Program Library Long Writeup W5013*. CERN, Geneva, 1994.
- [59] T. K. Gaisser, *Cosmic Rays and Particle Physics*. Cambridge University Press, Cambridge, 1990.
- [60] H. Bilokon, S. Bussino, C. Chiera, E. Lamanna, and L. Miller, “Muon Survival Probabilities in Gran Sasso Rock,” Tech. Rep. LNGS-94/92, Laboratori Nazionali del Gran Sasso, 1994.
- [61] M. Gluck, E. Reya, and A. Vogt, “Dynamical Parton Distributions of the Proton and Small X Physics,” *Z. Phys.* **C67**:433, 1995.
- [62] W. Lohmann, R. Kopp, and R. Voss, “Energy Loss of Muons in the Energy Range 1-GeV to 10000-GeV,” Tech. Rep. CERN-85-03, CERN, 1985.
- [63] H. Fesefeldt, “The Simulation of Hadronic Showers: Physics and Applications,” Tech. Rep. PITHA-85-02, CERN-DD-EE-81-1, CERN-DD-EE-80-2, CERN, 1985.

- [64] J. O. Johnson and T. A. Gabriel, “Development and Evaluation of a Monte Carlo Code System for Analysis of Ionization Chamber Responses,” Tech. Rep. ORNL/TM-10196, Oak Ridge National Laboratory, 1987.
- [65] C. Archer *et al.*, “Detection of Muons Produced by Cosmic Ray Neutrinos Deep Underground,” *Phys. Lett.* **18**:196, 1965.
- [66] F. Reines *et al.*, “Evidence for High-Energy Cosmic Ray Neutrino Interactions,” *Phys. Rev. Lett.* **15**:429, 1965.
- [67] B. Rossi and K. Greisen, “Cosmic-Ray Theory,” *Rev. Mod. Phys.* **13**:240, 1941.
- [68] T. K. Gaisser, “Semi-Analytic Approximations for Production of Atmospheric Muons and Neutrinos,” 2001, [astro-ph/0104327](#).
- [69] M. Honda, T. Kajita, K. Kasahara, and S. Midorikawa, “Calculation of the Flux of Atmospheric Neutrinos,” *Phys. Rev.* **D52**:4985, 1995.
- [70] V. Agrawal, T. Gaisser, P. Lipari, and T. Stanev, “Atmospheric Neutrino Flux Above 1 GeV,” *Phys. Rev.* **D53**:1314, 1996.
- [71] T. Gaisser and T. Stanev, “An Improved Calculation of the Atmospheric Neutrino Flux in the GeV Range,” *Proceedings of the 24th International Cosmic Ray Conference, 1995, Roma* **1**:694, 1995.
- [72] G. Battistoni *et al.*, “A Three-Dimensional Calculation of the Atmospheric Neutrino Fluxes,” *Astropart. Phys.* **12**:315, 2000.
- [73] W. R. Webber, R. L. Golden, and S. A. Stephens, “Cosmic Ray Proton and Helium Spectra from 5-200 GV Measured with a Magnetic Spectrometer,” *Proceedings of the 20th International Cosmic Ray Conference, 1987, Moscow* **1**:325, 1987.
- [74] E. Seo *et al.*, “Measurement of Cosmic-Ray Proton and Helium Spectra During the 1987 Solar Minimum,” *Astrophys. J.* **378**:763, 1991.

- [75] W. Menn *et al.*, “Measurement of the Absolute Proton and Helium Flux at the Top of the Atmosphere Using IMAX,” *Proceedings of the 25th International Cosmic Ray Conference, 1997, Durban* **3**:369, 1997.
- [76] R. Bellotti *et al.*, “Balloon Measurements of Cosmic Ray Muon Spectra in the Atmosphere Along With Those of Primary Protons and Helium Nuclei over Midlatitude,” *Phys. Rev.* **D60**:052002, 1999.
- [77] **Wizard-Caprice** Collaboration, G. Barbiellini *et al.*, “A Measurement of the Proton Spectrum at 1-AU Near Solar Minimum with the CAPRICE Experiment,” *25th International Cosmic Ray Conference (ICRC 97), Durban 1997*.
- [78] M. Boezio *et al.*, “The Cosmic Ray Proton and Helium Spectra Between 0.4-GeV and 200-GeV,” *Astrophys. J.* **518**:457, 1999.
- [79] P. Lipari, “The Primary Protons and the Atmospheric Neutrino Fluxes,” 1999, [hep-ph/9905506](https://arxiv.org/abs/hep-ph/9905506).
- [80] B. Nilsson-Almqvist and E. Stenlund, “Interactions Between Hadrons and Nuclei: The Lund Monte Carlo, FRITIOF Version 1.6,” *Comput. Phys. Commun.* **43**:387, 1987.
- [81] E. Stenlund and I. Otterlund, “Do Pseudo-Rapidity Distributions from Proton-Nucleus Interactions Scale?” Tech. Rep. EP/82-42, CERN, 1982.
- [82] C. Störmer, “On the Trajectories of Electric Particles in the Field of a Magnetic Dipole with Applications to the Theory of Cosmic Radiation,” *Astrophysics* **1**:237, 1930.
- [83] T. Johnson, “The Azimuthal Asymmetry of the Cosmic Radiation,” *Phys. Rev.* **43**:834, 1933.
- [84] L. Alvarez and A. H. Compton, “A Positively Charged Component of Cosmic Rays,” *Phys. Rev.* **43**:835, 1933.

- [85] T. Futagami *et al.*, “Observation of the East-West Anisotropy of the Atmospheric Neutrino Flux,” *Phys. Rev. Lett.* **82**:5194, 1999.
- [86] The International Geomagnetic Reference Field is available with regular updates at  
<http://nssdc.gsfc.nasa.gov/space/model/magnetos/igrf.html>.
- [87] P. Lipari, “The East-West Effect for Atmospheric Neutrinos,” *Astropart. Phys.* **14**:171, 2000.
- [88] P. Lipari, “The Geometry of Atmospheric Neutrino Production,” *Astropart. Phys.* **14**:153, 2000.
- [89] C. H. Llewellyn Smith, “Neutrino Reactions at Accelerator Energies,” *Phys. Rept.* **3**:261, 1972.
- [90] G. L. Fogli and G. Nardulli, “A New Approach to the Charged Current Induced Weak One Pion Production,” *Nucl. Phys.* **B160**:116, 1979.
- [91] D. Rein and L. M. Sehgal, “Neutrino Excitation of Baryon Resonances and Single Pion Production,” *Ann. Phys.* **133**:79, 1981.
- [92] R. P. Feynman, M. Kislinger, and F. Ravndal, “Current Matrix Elements from a Relativistic Quark Model,” *Phys. Rev.* **D3**:2706, 1971.
- [93] P. Lipari, M. Lusignoli, and F. Sartogo, “The Neutrino Cross-Section and Upward Going Muons,” *Phys. Rev. Lett.* **74**:4384, 1995, [hep-ph/9411341](#).
- [94] H. Plochow-Besch, *PDFLIB: Proton, Pion and Photon Parton Density Functions, Parton Density Functions of the Nucleus and  $\alpha_S$  Calculations: User’s Manual - Version 8.04, Program Library W5051*. CERN, Geneva, 2000.
- [95] M. Gluck, E. Reya, and A. Vogt, “Dynamical Parton Distributions Revisited,” *Eur. Phys. J.* **C5**:461, 1998, [hep-ph/9806404](#).

- [96] T. Sjöstrand, “Pythia 5.7 and Jetset 7.4: Physics and Manual,” *Computer Physics Commun.* **82**:74, 1994, [hep-ph/9508391](#).
- [97] G. D. Barr, *The Separation of Signals and Background in a Nucleon Decay Experiment*. PhD thesis, Oxford University, 1987. Also Tech. Rep. RAL-T-052.
- [98] H. Gallagher, *Neutrino Oscillation Searches with the Soudan 2 Detector*. PhD thesis, University of Minnesota, 1996. Also Tech. Rep. UMI-96-26361.
- [99] Z. Koba, H. B. Nielsen, and P. Olesen, “Scaling of Multiplicity Distributions in High-Energy Hadron Collisions,” *Nucl. Phys.* **B40**:317, 1972.
- [100] C. Walter and R. Nolty, “The FARFALLA Programming Reference Guide,” *MACRO Memo 1002/94* 1994. Also available at [http://www.hep.caltech.edu/macro/farfalla/farfalla\\_ref/](http://www.hep.caltech.edu/macro/farfalla/farfalla_ref/).
- [101] E. Kearns, “DASH: A Data Analysis Shell Manual for MACRO Users,” *MACRO Memo 1021/93* 1993.
- [102] Inter-Sol Group, [www.inter-sol.org](http://www.inter-sol.org).
- [103] G. J. Feldman and R. D. Cousins, “A Unified Approach to the Classical Statistical Analysis of Small Signals,” *Phys. Rev.* **D57**:3873, 1998, [physics/9711021](#).